

WEIRD: Wide-orbit Exoplanet search with InfraRed Direct imaging

FRÉDÉRIQUE BARON,¹ ÉTIENNE ARTIGAU,¹ JULIEN RAMEAU,¹ DAVID LAFRENIÈRE,¹ JONATHAN GAGNÉ,^{2,3} LISON MALO,¹ LOÏC ALBERT,¹ MARIE-EVE NAUD,¹ RENÉ DOYON,¹ MARKUS JANSON,⁴ PHILIPPE DELORME,⁵ AND CHARLES BEICHMAN⁶

¹*Institut de Recherche sur les Exoplanètes, Département de Physique, Université de Montréal, Montréal, QC H3C 3J7, Canada*

²*Carnegie Institution of Washington DTM, 5241 Broad Branch Road NW, Washington, DC 20015, USA*

³*NASA Sagan Fellow*

⁴*Department of Astronomy, Stockholm University, SE-106 91 Stockholm, Sweden*

⁵*Université de Grenoble Alpes, CNRS, IPAG, F-38000 Grenoble, France*

⁶*NASA Exoplanet Science Institute, California Institute of Technology, Jet Propulsion Laboratory, Pasadena, CA 91125, USA*

ABSTRACT

We report results from the Wide-orbit Exoplanet search with InfraRed Direct imaging (WEIRD), a survey designed to search for Jupiter-like companions on very wide orbits (1000 to 5000 AU) around young stars (<120 Myr) that are known members of moving groups in the solar neighborhood (<70 pc). Sharing the same age, distance, and metallicity as their host while being on large enough orbits to be studied as "isolated" objects make such companions prime targets for spectroscopic observations and valuable benchmark objects for exoplanet atmosphere models. The search strategy is based on deep imaging in multiple bands across the near-infrared domain. For all 177 objects of our sample, z'_{ab} , J , [3.6] and [4.5] images were obtained with CFHT/MegaCam, GEMINI/GMOS, CFHT/WIRCcam, GEMINI/Flamingos-2, and *Spitzer*/IRAC. Using this set of 4 images per target, we searched for sources with red z'_{ab} and [3.6]–[4.5] colors, typically reaching good completeness down to 2 M_{Jup} companions, while going down to 1 M_{Jup} for some targets, at separations of 1000–5000 AU. The search yielded 4 candidate companions with the expected colors, but they were all rejected through follow-up proper motion observations. Our results constrain the occurrence of 1–13 M_{Jup} planetary-mass companions on orbits with a semi-major axis between 1000 and 5000 AU at less than 0.03, with a 95% confidence level.

Keywords: Exoplanets — Direct Imaging — Brown Dwarfs

1. INTRODUCTION

Since the first detection of an exoplanet around a main sequence star by Mayor & Queloz (1995), thousands of exoplanets have been discovered, revealing planetary system architectures vastly different from that of the Solar System. The most successful methods to detect exoplanets are the transit and radial velocity methods, which are more effective for planets close to their host star (up to 15 AU). The outer part of planetary systems can be probed by direct imaging. The first detection of a giant planet by direct imaging was made in 2004, with the discovery of a 4 M_{Jup} planet orbiting the brown dwarf 2MASSW J1207334-393254 (Chauvin et al. 2004), and the search for directly imaged planets has continued since then.

A good number of direct imaging surveys for planetary mass objects on wide orbits were carried out in the last decade. Some targeted only low mass stars, such as Bowler et al. (2015), Lannier et al. (2016), and Naud et al. (2017), while others surveyed higher mass stars (Vigan et al. 2012; Nielsen et al. 2013; Rameau et al. 2013) or all spectral types

(Lafrenière et al. 2007b; Heinze et al. 2010; Biller et al. 2013; Chauvin et al. 2015). Bowler (2016) did a meta-analysis using data from the most complete studies that surveyed all types of star (Lafrenière et al. 2007b; Janson et al. 2011; Vigan et al. 2012; Biller et al. 2013; Janson et al. 2013; Nielsen et al. 2013; Wahhaj et al. 2013; Brandt et al. 2014; Bowler et al. 2015) using 384 stars with spectral types B2 to M6. He obtained an overall planet occurrence rate for BA, FGK, and M stars of respectively 2.8^{3.7}_{-2.3} %, <4.1%, and <3.9% for 5-13 M_{Jup} planets at separations of 30 to 300 AU.

Direct imaging surveys have typically targeted young stars, which are prime targets since their planets are still contracting and are thus warmer and brighter than their older counterparts, for a given mass. The number of known young stars near the Sun has dramatically increased in the last few years, as a result of a growing interest for young stellar moving groups (e.g., Zuckerman & Song 2004; Torres et al. 2008). A moving group is composed of stars that were formed together less than a few hundreds of Myr ago, and therefore still share similar UVW galactic velocities, enabling their identifica-

tion. In the recent years, a significant effort has been made to identify a large number of low mass stars, brown dwarfs and isolated planetary-mass objects that are members of known young moving group (Lépine & Simon 2009; Shkolnik et al. 2009; Kiss et al. 2011; Schlieder et al. 2010; Rodriguez et al. 2011; Liu et al. 2013; Schlieder et al. 2012a,b; Shkolnik et al. 2012; Malo et al. 2013; Moór et al. 2013; Rodriguez et al. 2013; Kraus et al. 2014; Malo et al. 2014; Riedel et al. 2014; Gagné et al. 2014; Binks et al. 2015; Gagné et al. 2015b).

Planets found on wide orbits around young stars are very interesting because they can be characterized much better than their closer-in counterparts. First, a planet bound to a well-studied star shares some properties with it, like its age, distance from Earth, and metallicity. Furthermore, when a planet is on an large enough orbit, it can be studied as if it were an isolated object, that is without adaptive optics (Naud et al. 2014; Gauza et al. 2015), and a very high resolution spectrum can then be acquired, which is very hard to obtain for closer-in planets. Also, the large separation to the host enables direct studies that are very challenging with high-contrast imaging (e.g., accurate spectro-photometry, intermediate resolution spectroscopy, optical imaging, time-variability). Such planetary mass objects are also prime targets for *JWST* follow-up.

Widely separated systems are of further interest because they challenge formation processes. Theories predict that giant planets form either by core accretion or gravitational instability, or like brown dwarfs by cloud fragmentation. The former process describes a way of forming planets by first building a 5 to 20 M_{Earth} core of rocks and ices, in a protoplanetary disk (Alibert et al. 2009; Inaba et al. 2003; Pollack et al. 1996). The core then accretes gas very rapidly to form a giant planet. This method explains very well the formation of planets on close-in orbit (< 10 AU, Mordasini et al. 2012), but struggles to explain the formation of planets on wide orbits. The second process suggests that planets form from the fragmentation of a gravitationally unstable disk (Boss 2011), which forms clumps that then can accrete gas and dust to become planets (Stamatellos et al. 2007; Bate 2012). However, this mechanism also has difficulties forming planets on wide orbits, as shown for example by Nayakshin (2017) and Vigan et al. (2017). The last process predicts that planets on wide orbits form from the direct collapse of the molecular cloud (Padoan & Nordlund 2004). A fragment of a few Jupiter mass is formed which then accretes gas from the cloud to form a higher mass object. However, Bate et al. (2002) and Bate (2012) have shown that the accretion process can be stopped at a low mass if the companion is ejected away from the dense part of the envelope or if the envelope is depleted at the formation time. However this formation process tends to form preferentially equal mass binaries and does not seem to produce systems with the high mass ratios needed to match

the observed planetary systems at wide separations. Dynamical instabilities are a tantalizing alternative to explain the detected planets at large separations (Chatterjee et al. 2008; Veras et al. 2009; Baruteau & Masset 2013). Mutual gravitational perturbations and close encounters among the planets occur and pump the eccentricity and the semi-major axis of the less massive giant planets up to 100 - 100 000 AU (Veras et al. 2009), but close-in scatterers are yet to be discovered (Bryan et al. 2016).

We report here the results from the Wide-orbit Exoplanet search with InfraRed Direct imaging (WEIRD). The WEIRD survey started in 2014 with the aim to detect Jupiter-like companions on very wide orbits (at separations 1000–5000 AU) around all the known members of young moving groups within 70 pc. We gathered a large dataset to try to construct the SED of such objects through of deep [3.6] and [4.5] imaging from *Spitzer*/IRAC and deep seeing-limited J and z'_{ab} imaging from CFHT and Gemini-South of all 177 known (at the time) young (< 120 Myr) objects in a volume-limited sample of 70 pc of the Sun. Using these data, planetary companions can be revealed through their distinctively red $z'_{ab}-J$ and [3.6]–[4.5] colors. The range of separations studied here has been barely probed by previous direct imaging surveys as they were limited by the field of view of high contrast imagers, with the exception of Naud et al. (2017), which was much less sensitive than the present survey, and limited to low-mass stars. The selection of the sample of young stars and the observing strategy and data reduction are described in Section 2. Section 3 presents the results of our search, while Section 4 discusses the statistical analysis of the survey.

2. SAMPLE AND OBSERVATIONS

2.1. Sample

The best targets to find giant planets on very wide orbits are young stars in the solar neighborhood because giant planets are more luminous when they are younger and they become fainter with time. Therefore, observations of younger stars are sensitive to lower-mass planets. A sample was thus created by selecting all stars within 70 pc that are members of the following young moving groups or associations (see Table 1): TW Hydrae (de la Reza et al. 1989; Kastner et al. 1997), β Pictoris (Zuckerman et al. 2001a), AB Doradus (Zuckerman et al. 2004), Tucana Horologium (Torres et al. 2000; Zuckerman et al. 2001b), Carina (Torres et al. 2008), Columba (Torres et al. 2008) and Argus (Makarov & Urban 2000). The members of these groups have ages in the range 10–150 Myr. The age of the Argus moving group is not well constrained, likely because current membership lists suffer from significant contamination from unrelated field-aged stars (Bell et al. 2016). To be considered bona fide members of one group and included in our sample, the

Table 1. Young Moving Groups

Name	Distance (pc)	Age (Myr)	Number of members detected	Ref.
$N\beta$ -Pictoris	9-73	24 ± 3	51	Shkolnik et al. (2017)
AB-Doradus	37-77	149^{+51}_{-19}	58	Bell et al. (2016)
Argus	8-68	30-50	10	Torres et al. (2008)
Carina	46-88	45^{+11}_{-7}	6	Bell et al. (2016)
Columba	35-81	42^{+6}_{-4}	15	Bell et al. (2016)
Tucana-Horologium	36-71	45 ± 3	50	Bell et al. (2016)
TW Hydrae	28-92	10 ± 3	16	Bell et al. (2016)

stars must have a trigonometric parallax and a radial velocity measurement, $XYZUVW$ values consistent with the moving group membership, as well as independent signatures of youth, e.g. spectroscopic signs of low-gravity, strong X-ray or UV emission or lithium absorption (see Soderblom 2010). The sample was constructed from Gagné et al. (2014); Kiss et al. (2011); Lépine & Simon (2009); Malo et al. (2013); Schlieder et al. (2010); Shkolnik et al. (2009); Shkolnik et al. (2011); Shkolnik et al. (2012); Song et al. (2003); Torres et al. (2000); Torres et al. (2008); Zuckerman & Webb (2000); Zuckerman et al. (2004); Zuckerman et al. (2001a); Zuckerman (2001); Zuckerman et al. (2011). We note that these publications also proposed a larger sample of strong candidates but they lacked one or more measurements to be confirmed members; these objects were not included in our sample. Our complete sample includes 177 objects.

Multiple systems were not excluded from the sample as the presence of a lower or equal mass object does not exclude the possibility of having a planetary mass object on a wide orbit. For example, Ross 458 (AB)c is a triple system comprising a tight M0.5+M7 binary orbited by an 11 M_{Jup} object (Goldman et al. 2010) and 2MASS J01033563-5515561(AB)b, a 12–14 M_{Jup} object, orbits a pair of young late-M stars at 84 AU (Delorme et al. 2013). Also, Wang et al. (2015) have shown that stellar multiplicity does not influence the presence of planets on wide (100 to 2000 AU) orbits in the system. In our sample of targets, 68 are multiple systems, 2 host brown dwarf companions (Schneider et al. 2004; Chauvin et al. 2005) and 4 host known planets (Chauvin et al. 2004; Marois et al. 2008; Lagrange et al. 2009; Macintosh et al. 2015).

The properties of the 177 objects in our sample is presented in Table 2. They have spectral classes in the range A–M, with a majority of M dwarfs, are located at distances of 7 to 70 pc, are located all over the sky, and have relatively high proper motions (see Figure 1). The median star has a proper motion of 100 mas/yr, a distance of 42 pc and an age of 45 Myr. Table 3 lists all the systems in our sample along with their radial velocities, distances and the association they are a member of.

2.2. Observing strategy

Figure 2 presents the typical $z'_{ab} - J$ and [3.6]–[4.5] colors as a function of spectral type for objects ranging from spectral types L to T, a range relevant for the companions sought here. It shows that both L and T dwarfs have very red $z'_{ab} - J$ colors, with the color of an L dwarf being between 2.5 and 3 mag, and the color of a T dwarf between 3 and 4.5 mag. Beyond those types, as shown by Lodieu et al. (2013), the $z'_{ab} - J$ colors of Y dwarfs remain red but vary much more, ranging from 2.5 to 5 mag. In the mid-infrared, starting at around T0, the [3.6]–[4.5] color becomes increasingly red with spectral type, reaching values larger than 1.5 mag for late-T's. Young objects, with larger radii and correspondingly lower surface gravities, would have slightly redder colors compared to the colors of field dwarfs shown in the figure. The strategy used in the current survey builds on these markedly red colors of very late-type dwarfs across these four spectral bands, which enables distinguishing them easily from earlier-type objects and most other astrophysical sources. In addition, as shown in Figure 3, these bands are also optimal to maximize the flux of the objects sought over the temperature range of interest.

The ground-based component of our survey is optimized to find companions up to spectral type $\sim T9$, while the Spitzer component is optimized for later types. At a distance of 42 pc (the median distance of our sample), the expected J magnitude of a T9 dwarf is about 21 mag. We thus designed our observations in J -band to reach 21 mag. As T dwarfs later than T0 are expected to have $z'_{ab} - J > 3$ mag, we designed our observations to reach $z'_{ab} = 24$ mag as they can be identified either through detection in both bands or as z'_{ab} dropouts. For the this part of the survey, we used the same detection criteria as for the CFBDSIR survey (Delorme et al. 2008, 2010; Albert et al. 2011). That survey was a wide-field search for T dwarfs and early-type Y dwarfs, and the candidates were identified through their very-red $z'_{ab} - J > 3$ mag colors if they were detected in both bands, or through z'_{ab} dropouts. The CFBDSIR survey returned only 64 candidates over the 280 square degrees observed, of which 17 were actual field T dwarfs. The strategy of searching for very low-

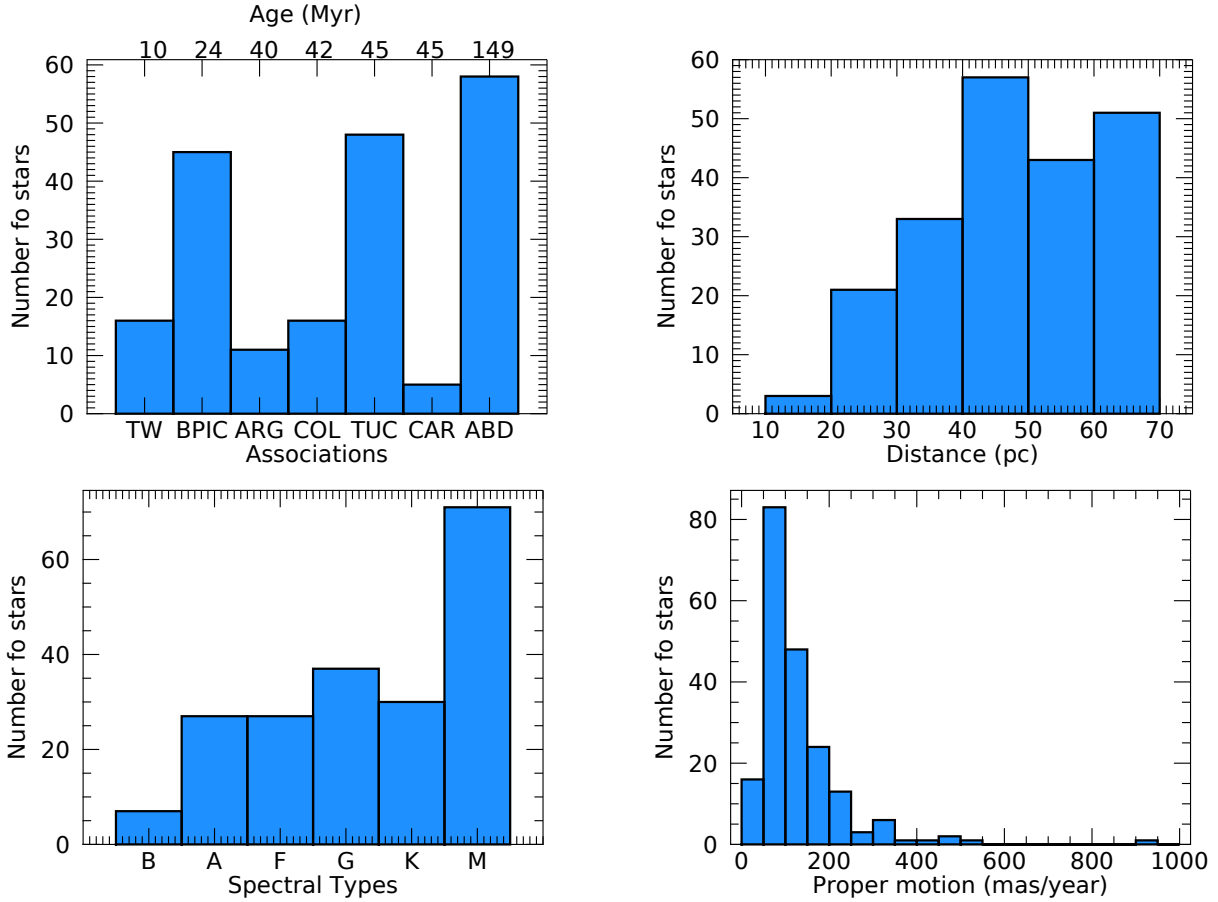


Figure 1. Distributions of associations, distances (pc), spectral types and proper motions (mas/yr) for all the stars in the sample.

mass objects using NIR colors has also been employed by the PSYM-wide survey (Naud et al. 2017) to probe nearby young M dwarfs for planetary mass companions. The survey discovered a new planetary mass object ($9\text{--}13 M_{\text{Jup}}$) orbiting at 2000 AU around the M3V star Gu Psc, a highly probable member of the AB Doradus moving group (Naud et al. 2014)¹.

The *Spitzer*/IRAC observations were designed so that they reach a sufficient depth to identify point-sources in the field down to ~ 0.5 mag of the confusion limit and have their color measured with accuracy to identify them at $> 5\sigma$ level compared to the bulk of background objects. We perform the point-source detection in [3.6], which provides deeper images for flat-spectrum sources, and use the [4.5] photometry to constrain colors. Our observations are designed to reach depths of 21.2 mag (5σ) and 20.7 mag (3σ) in [3.6] and [4.5], respectively. Planetary-mass objects close

to the detection limit, with masses below $3\text{--}5 M_{\text{Jup}}$ will have $[3.6] - [4.5] > 2$ mag (see right-hand side Figure 2) and will therefore be detected at a higher signal-to-noise ratio in [4.5]. Because they would have $M_J > 18$ mag (or $J > 21$ mag for a typical target) or a spectral type $\gtrsim T8.5$, such objects would be z'_{ab} - and J -band dropouts ($z'_{ab} - [4.5] > 6$ mag and $J - [4.5] > 3.5$ mag). Given that background objects typically have $[3.6] - [4.5] \sim 0.0 \pm 0.4$ mag, such planetary-mass objects will differ from the bulk of background objects at the $> 5\sigma$ -level. However, by itself this part of the dataset is insensitive to more massive ($> 3\text{--}5 M_{\text{Jup}}$) companions as their colors don't differ enough from those of background objects.

2.3. Observations and Data Reduction

All targets in our sample were observed with deep seeing-limited J and z'_{ab} imaging at either the Canada-France-Hawaii Telescope (CFHT) with WIRCam (Puget et al. 2004) and Megacam (Boulade et al. 1998), or at Gemini-South with GMOS-S (Hook et al. 2004; Gimeno et al. 2016) and Flamingos-2 (Eikenberry et al. 2012), as well as with *Spitzer*/IRAC (Fazio et al. 2004) in the [3.6] and [4.5] bands. Stars with a declination $< -35^\circ$ were observed from the ground at the Gemini-South Observatory while the others

¹ Using the parallax of 21.0019 ± 0.0721 mas (Lindegren et al. 2018; Gaia Collaboration et al. 2018) for GU Psc from the *Gaia* DR2 release, and the web tool BANYAN Σ from Gagné et al. (2018b), we infer that the probability of Gu Psc to be a member of the AB Doradus moving group is 99.1 %, which confirms the membership of the star.

were observed at the CFHT. Throughout this work, all the J -band magnitudes are in the Vega system while all the z'_{ab} magnitudes are in the AB system. For a median star in our sample with a distance of about 42 pc and an age of 45 Myr, the limiting magnitude in both bands corresponds to $M_J = 17.9$ mag and $M_z = 20.9$ mag, or to an effective temperature of about 385 K according to models from Baraffe et al. (2003).

2.3.1. Gemini Observations

The observations were made from 2014 to 2017 at Gemini-South (GS-2014B-Q-2, GS-2015A-Q-71, GS-2015B-Q-57, GS-2016A-Q-69, GS-2016B-Q-33, GS-2017A-Q-58, PI Frederique Baron). We obtained deep imaging of our southern sub-sample with Flamingos-2 with the J filter (J_G0802, $1.255 \mu\text{m}$) and the Gemini Multi-Object Spectrograph (GMOS) in the z'_{ab} filter (z_G0328, $>848 \mu\text{m}$). Objects beyond 30 pc, the vast majority of our targets, are sufficiently far for the entire projected 5000 AU sphere around them to fit within the GMOS/F2 FOV.

Flamingos-2 is a near-infrared wide-field imager and multi-object spectrometer with a 6.19 arcmin^2 circular field of view and a $0.18''$ pixel scale. We obtained at least 600s of integration time on each target, divided into a different number of expositions (at least 9) depending on the magnitude of the star and the observing conditions. A small random dither pattern was used to mitigate detector defects. The exposition time was selected to reach a limiting magnitude of $J = 21$ mag at a 7σ level. Each observation was about 20 minutes long, including all overheads.

GMOS has three 2048×4608 CCDs which, when combined, have a field of view of $5.5 \times 5.5 \text{ arcmin}^2$ and a pixel scale of $0.073''$. We obtained 8 expositions of 65 s for each target of the sample. A dither pattern of $17''$ was used for all observations. The exposure time was chosen to reach a limiting magnitude of $z = 24$ mag at 3σ . The observations were each about 20 minutes long, including all overheads.

The J -band images from F2 were reduced using a custom IDL pipeline. The individual images were reduced by subtracting dark images, dividing by flat field images, and correcting the residual gradient from the vignetting of the Peripheral Wavefront Sensor (PWFS). This step was done by first normalizing the image to its median value, then masking regions with values significantly over the median to get rid of the stars. This image was in turn used to create a gradient image where each pixel is the median of a 128×128 pixel box of the masked image. A polynomial fit of degree 3 was then applied to the gradient image. This was divided from the F2 image to correct for the vignetting by the PWFS. The astrometric correction was then computed by anchoring the star positions on the *Gaia* DR1 catalog (Gaia Collaboration et al. 2016). A radial profile about the bright target star was then

subtracted to help search for sources at smaller separations. Lastly, a low-pass filter was created by median binning the image by 4×4 pixels, applying a 15×15 -pixel median filter, and then resampling at the original image size. This low-pass filter was subtracted from the image to facilitate the detection of point sources. The individual images for a given target were then combined by taking their median, after astrometric registration, to produce the final J -band image.

For GMOS, the images were also reduced using a custom IDL reduction pipeline. Each CCD was first processed separately. First, a sky correction was applied by subtracting the median of all images taken on a given night. When needed, any detector region affected by the on-instrument wave front sensor was masked. Most of the time the wave front sensor was off the detector, but sometimes it was not possible to find a guide star outside of the FOV. The astrometric solution was found for each CCD by anchoring the field to the F2 reduced image of the same target. A high-pass filter was then applied by subtracting a median-filtered image with a width of 15 pixels. A one-dimensional median-filter with a width of 61 pixels was also subtracted from each line of the image to correct for the saturation banding. The 3 CCDs were then combined to form a complete image, to which the astrometric solution was applied again. All the images for a given target were then aligned and stacked by taking their median to get the resulting reduced image.

2.3.2. CFHT Observations

Deep imaging of our northern sub-sample was obtained at the CFHT from 2014 to 2017 using WIRCam with the J filter and MegaCam with the z'_{ab} filter (14BC016, 15AC032, 15BC012, 16AC021, 16BC018, 17AC23; PI Frédérique Baron).

WIRCam (Puget et al. 2004) is a near infrared wide-field imager with a field-of-view of 20 arcmin^2 and a pixel scale of $0.3''$. It uses a mosaic of 4 detectors with a small gap between each. We used the J -band ($1.253 \mu\text{m}$) filter and a homemade dither pattern of 16 60-s expositions, arranged so that the target does a small dither of $28''$ around a pixel situated $64''$ from the corner of one detector near the center of the field, for a total of 1120 s of on-target integration time. A different dither pattern was used to mitigate the saturation effects of stars brighter than $J = 7$. In those cases, the bright target was put in a gap between quadrants at each position of the dither pattern. With a seeing between $1''$ and $1.2''$, the exposure time is sufficient to reach a $\text{SNR}=7$ at a limiting magnitude of $J \approx 21$.

MegaCam (Boulade et al. 1998) is a wide-field optical imager with a 1 square degree field-of-view and a pixel scale of $0.187''$. We used the z'_{ab} filter (z_G0328, $>848 \mu\text{m}$) and a dither pattern with 4 positions offset by $15''$, which is twice the size of the standard dither pattern. The total integration

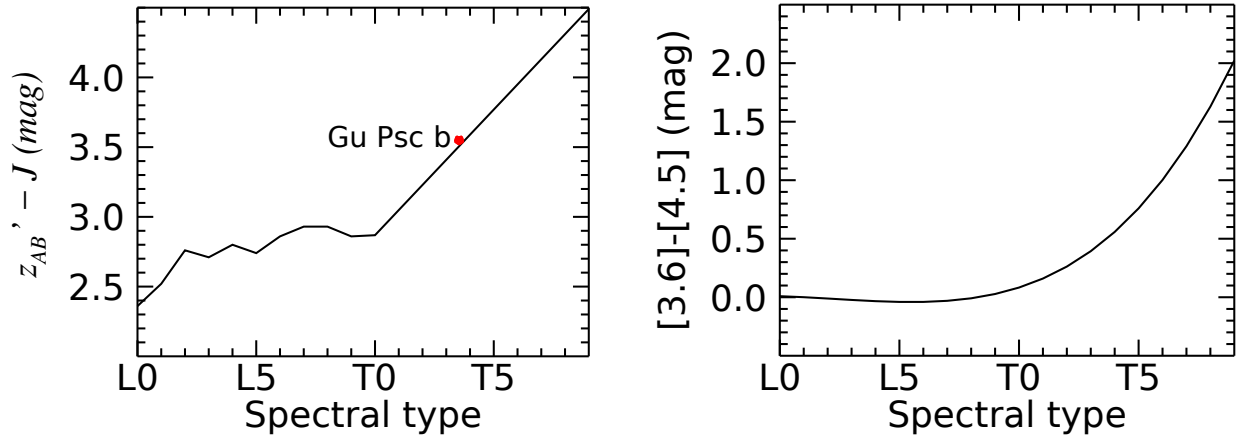


Figure 2. On the left, $z'_{ab} - J$ vs spectral type for L to T dwarfs from Hawley et al. (2002) for the L dwarfs and Albert et al. (2011) for the T dwarfs. The L to T dwarfs are characterized by red $z'_{ab} - J$ colors. The red dot represents Gu Psc b, the planetary mass object discovered by Naud et al. (2014), representative of the kind of objects we are seeking in this work. On the right, $[3.6]-[4.5]$ for L to T dwarf from Dupuy & Liu (2012). We see that late T dwarfs can be identified both by their red $[3.6]-[4.5] > 1.5$ and $z'_{ab} - J > 4$ colors.

time per target varies between 311 s and 476 s. The higher integration time is for targets with a declination in the range -35 to -30 , to accommodate the higher airmass and maintain a good SNR. With a seeing between $0.55''$ and $0.65''$, this ensures a SNR of 3 for all our z'_{ab} -band observations with a limiting magnitude of $z'_{ab}=24$.

The WIRCam images were reduced using the method described in Albert et al. (2011). First, they were preprocessed by CFHT using their ‘iwi pipeline version 2.0. Next, a low-pass filter was created by median binning the image by 4×4 pixels, applying a 5×5 -pixel median filter, and then re-sampling at the original image size. This low-pass filter was subtracted from the image to preserve only high spatial frequencies. After this, the different images were stacked using the Bertin software suite. First, SExtractor (Bertin & Arnouts 1996) builds a catalog of objects in each image. This catalog is in turn read by Scamp (Bertin 2010a), which also computes the astrometric and photometric solutions by anchoring on the J -band data of the 2MASS catalog. Swarp (Bertin 2010b) then stacks the images together.

Data from MegaCam were first processed by CFHT’s Elixir pipeline. Then, the astrometric solution from each of the 40 CCDs was found by anchoring the field on the positions from the USNO-B1 catalog. A high-pass filter was applied, as before, by subtracting an image created by median binning the image by 4×4 pixels, applying a 7×7 -pixel median filter, and then re-sampling at the original image size. Then the images from the different CCDs were combined to form an image of size matching that of the WIRCam images, as the field of view of MegaCam is much wider than WIRCam’s. The different images of a given target obtained on a given night were then median-combined to obtain the final reduced z'_{ab} image.

2.3.3. *Spitzer*/IRAC observations

Our complete sample was observed with *Spitzer*/IRAC. Nine of our targets had previously been observed with IRAC with an exposition time that meets our requirements. The others targets were observed between 2015 and 2016 (*Spitzer* proposal 11092) in both IRAC $[3.6]$ and $[4.5]$, with a total integration time of 2160 s in each band (per-visit total of 5221 s with overheads). More precisely, we used 30 s individual exposure time, two exposures per dither position per band, and a 36-exposure reuleaux dither pattern.

The *Spitzer*/IRAC pipeline reduced images were further processed with custom IDL routines. First, the different images of a given target were oversampled on a $0.5''$ pixel grid and median-combined using the pipeline-provided astrometry and polynomial distortion. Then, to preserve the PSF morphology orientation in the image, in view of the PSF subtraction routines to be applied, we registered all images to a common PSF rotation angle.

Further data reduction involved the subtraction of the stellar point spread function (PSF) to reveal embedded and close-in sources. Since the *Spitzer* observations were uniform, we used the Reference Differential Imaging technique to subtract the PSF from a reference library. The strategy is similar to the re-analysis of *Hubble* imaging data through the ALICE project (Soummer et al. 2016; Choquet et al. 2015), and to previous analysis of archival *Spitzer* data (Janson et al. 2015; Durkan et al. 2016).

The library of reference PSF was created out of the newly obtained data, using the PSF of the observed stars. Saturated stars, very crowded fields, and low-contrast (< 1) visual binaries were removed from the library, resulting in a total of 111 PSFs out of the 168 targets observed. Each image was registered on a common center based on the fit of a two-dimensional Moffat function. It was then normalized in brightness from the flux measured in an aperture of a radius of seven pixels centered on the PSF core. Point sources were

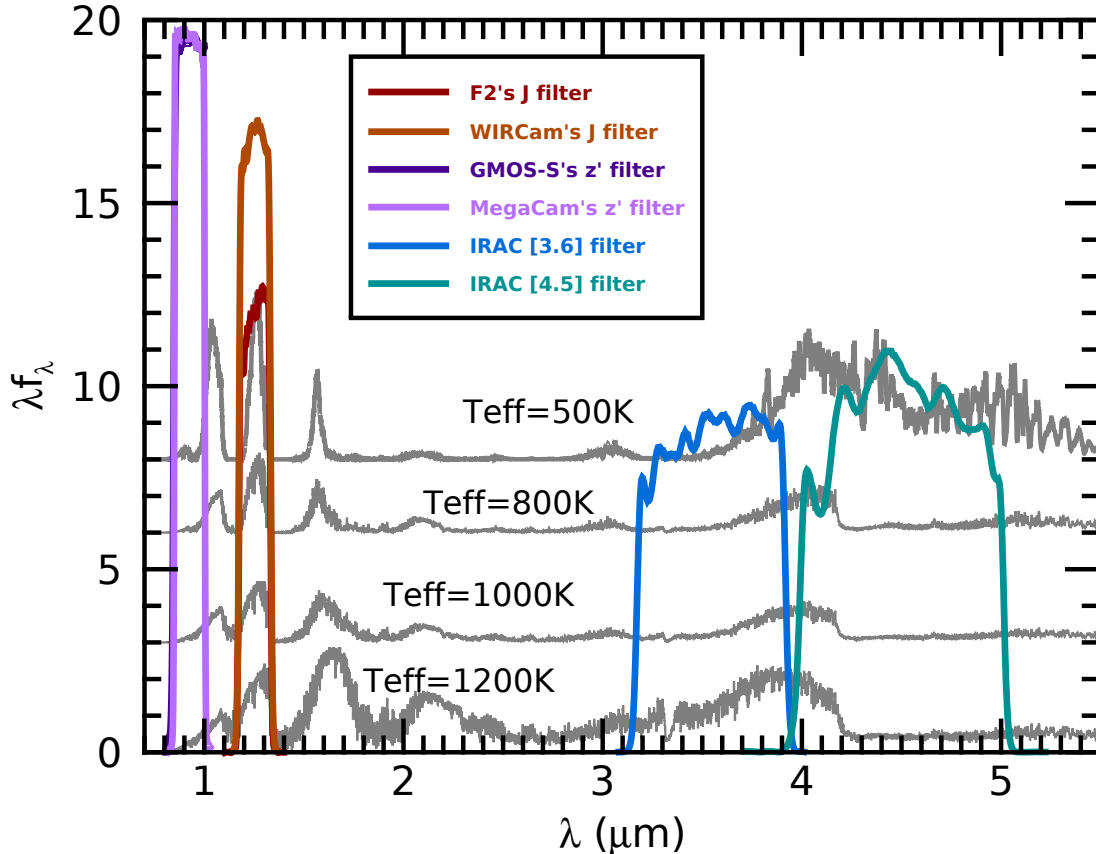


Figure 3. BT-Settl spectral energy distribution of young objects ($\log g = 4$ and solar metallicity) with effective temperatures of 500 K, 800 K, 1000 K, and 1200 K. The transmission functions of the four bandpasses used for our observations (z'_{ab} , J, [3.6], and [4.5]) are overlaid. These bandpasses provide distinctive red colors while maintaining a high flux level across the temperature range.

identified as 3σ outliers from the noise (calculated with a robust sigma estimator) after an initial PSF subtraction from the median of the reference library, excluding the given image. They were subsequently masked out in the original image.

We used classical RDI to subtract stellar PSFs in each *Spitzer* image for both filters. Because of the very large number of point sources in our deep data, advanced techniques such as LOCI or PCA (Lafrenière et al. 2007a; Soummer et al. 2012) suffered from too many pixels that were masked out, reducing the effective number of reference images. They tended to oversubtract the target PSF and other point sources in the field. We therefore opted for a classical median subtraction, a trade-off between the quality of the PSF subtraction and source preservation. Following this strategy, the processed image under consideration was excluded from the library of references, the median of which was then taken as the reference PSF for subtraction of this image. The position of the star was estimated by fitting a Moffat function and the reference PSF was shifted to this position. The reference PSF was normalized to the target brightness within the same aperture and subtracted from the image. This three-step process was repeated for any low-contrast (< 1) visual companion of our target present in the field. For tight binaries or triple

systems, the subtraction of all PSFs was done at once by iterating over the position and flux of each component in order to minimize the residuals in a box of width of 30 pixels. Saturated stars were processed like binaries to optimize the star registration and flux normalization. They still suffered from poorly subtracted wings and bright vertical stripes escaping from the core. Therefore, a new library was built from residual images of similarly saturated stars, following the same cleaning processes as for the original library. The median of this new library was used to subtract these residuals.

The images were finally high-pass filtered by subtracting a median filter of width 15 pixels.

2.3.4. Archival *Spitzer*/MIPS 24 μm data

A search through the *Spitzer* archive revealed that 141 of our 177 targets were observed with MIPS at 24 μm as part of surveys to find infrared excess indicative of debris disk. A flux measurement (or upper limit) at such a longer wavelength can be useful to better constrain the SED of our candidate objects identified. Thus for those 141 targets we retrieved the MIPS data and built our own combined image using the Enhanced BCD images (EBCD), as they have a superior flat fielding than the BCD image. A high-pass fil-

ter was then applied by subtracting a double-pass median-filtered version of the image, respectively of widths 32 and 12. We obtained the limiting flux in Jy/sr by doing aperture photometry at several random positions over the whole image and then evaluating the robust standard deviation of the resulting flux distribution. We converted this limiting flux in Jy/sr to magnitude and, over all images, obtained a median limiting magnitude of 12.5 mag.

2.4. Photometric calibration

Our GEMINI observations were all acquired with a specification for observing conditions of up to 70% cloud cover, or patchy clouds. Under those conditions, a variation of up to 0.3 mag can be expected. We assessed if significant variations were present or not from the data themselves. For a sequence of observations of a given field, we calculated the standard deviation of the flux variations of the 20 brightest stars, as compared to a reference image from the sequence. If this variation was higher than 3%, then we considered that the images of that target were not taken in photometric conditions ('patchy clouds' in table 4 and table 5); otherwise we considered that the images were taken under photometric conditions ('phot' in table 4 and table 5).

All of our CFHT images were taken in good conditions, with seeing around 0.6 for MegaCam and 1.1 for WIRCam, but we still checked the flux variations between images for a given target on a given night to make sure that the observations were acquired in photometric conditions.

Our final, stacked images in z'_{ab} and J were calibrated in flux by comparison with the Sloan Digital Sky Survey catalog (SDSS DR9; Ahn et al. 2012) or the 2MASS All-Sky Catalog of Point Sources (Cutri et al. 2003), respectively. If SDSS data were not available for a given field, we used either PanSTARRS (Chambers & Team 2018) z_{p1} data (available for 55 of our targets with dec > -30) or SkyMapper (Wolf et al. 2018) z' data (available for 79 of our targets). The PanSTARRS filters (g_{p1} , r_{p1} , i_{p1} , z_{p1} , y_{p1} , w_{p1}) are not the same as the SDSS filters, so we used the Tonry et al. (2012) color corrections to convert the Pan-STARSS magnitudes to SDSS magnitudes. For the J band, if too few stars in our images were in the 2MASS PSC, we used deeper data from the VISTA Hemisphere Survey (VHS; McMahon et al. 2013) or archival observations from the Observatoire du Mont Mégalantic obtained using the Spectrographe infrarouge de Montréal (SIMON) (Albert 2006).

For a given image, the magnitude that produces one count per second on the detector, or the zero point, was calculated for each individual point source in common between our image and the catalog, based on the difference between the magnitude extracted from our image and the magnitude taken from the catalog. Then, the zero point of the image was taken to be the median of the individual zero points, and

the error was computed by taking the standard deviation of those individual zero points divided by the square root of the number of sources.

When no catalog data were available for a given image, or when less than 5 objects with a magnitude measurement were available in the field of view, we used as a zero point the median zero point for the given observing condition ('phot' or 'patchy clouds'), instrument and filter of the image. This occurred for 16 of our J -band images and 48 of our z'_{ab} -band images. In the J band, we obtained a zero point of 22.4 ± 0.7 and 22.1 ± 0.9 with Gemini/F2, and 22.5 ± 0.8 and 22.7 ± 0.6 with CFHT/WIRCam, for photometric and non-photometric conditions respectively. In the z -band, we calculated a median zero point of 24.5 ± 0.3 and 24.6 ± 0.5 with CFHT/MegaCam and 29.7 ± 2 and 28.9 ± 2.3 with Gemini/GMOSS, for photometric and non-photometric conditions respectively.

2.5. Follow-up observations

Our search for planetary mass object revealed a number of candidates (see Section 3.2.3) that motivated us to obtain follow-up observations.

An astrometric follow-up was carried out between 2016 and 2017 in the J -band, with either CFHT/WIRCam or Gemini-South/Flamingos2. Only J -band images were obtained as it is in this band that the SNR of the candidate is highest. We used the same observation parameters as for the first epoch observations. We obtained proper motions follow-up in the J band for 4 candidate companions.

3. RESULTS

The ground-based observations described earlier were designed to reach a limiting magnitude of $z = 24$ mag at 3σ and $J = 21$ mag at 7σ . In practice, we achieved a median [AB] limiting magnitude in the z -band of 23.4 ± 1.2 mag with CFHT/MegaCam and 23.7 ± 1.2 mag with Gemini/GMOS-S, at 3σ . In the J -band, we achieved a 7σ median Vega limiting magnitude of 21.2 ± 0.5 mag with CFHT/WIRCam and 21.0 ± 0.8 mag with Gemini/F2. For the *Spitzer*/IRAC observations, we reached a median magnitude limit of 18.5 ± 0.9 mag at [3.6] at 5σ and 18.5 ± 0.8 mag at [4.5] at 3σ .

3.1. Detection Limits

The sensitivities to companions, in terms of limiting magnitudes, were evaluated for each J -band stacked image and [4.5] image as a function of the radial distance from the target star. For each radius from the central star, aperture photometry was performed by obtaining the flux inside 100 apertures of radius of 1 FWHM and a sky annulus between 4 to 6 FWHM. The limiting flux at each radius is the standard deviation of these 100 fluxes and it was then converted into magnitudes to get these 7σ limiting magnitudes. These results

are presented in Figure 4 for the J -band images and in Figure 5 for the [4.5] images. They show that the limiting magnitudes initially grow with increasing distance from the central star, and then reach a plateau. The black region of the plots contain 50% of the detection limit curves while 80% of the curves fall inside the grey region. For the J -band images, the plateau is reached at $\sim 30''$ at a magnitude of $J \sim 21.5$ mag for 50% of our target stars (the black region). The curves are truncated at about $180''$, which corresponds to the limit of the field of view of the *Flamingos-2* images. The plateau is reached at a projected physical separation of 1000 AU for an average star of our sample. For our [4.5] images, the plateau at magnitude ~ 18.5 is reached at a radius of $\sim 50''$ for 50% of the stars of the sample (the black region). We used the same cut-off as the J -band images. Tables 6 and 7 present, respectively for the J -band and [4.5] images, the 7σ detection limits for each target over the plateau along with the minimum and maximum separations (in arcsec and AU) where these limits are valid (defined as the range for which the detection limit is at most 1 magnitude brighter than the plateau value given, to accommodate for small fluctuations with separations).

The limiting magnitudes can be converted to limiting masses using evolutionary models at the ages of our targets (which range between 10 and 150 Myr). We used the COND models from Baraffe et al. (2003) to infer the masses. These models assume a hot start, which as described by Bowler (2016), corresponds to idealized initial conditions and an arbitrarily large initial radius. This model is thus optimistic as it represents more luminous planets than cold start models. The mass limit reached over the sensitivity plateau for each target is indicated in Table 6 and 7.

3.2. Candidate Search

We searched for and identified candidates in our imaging based on their $z'_{ab} - J$ and [3.6]–[4.5] colors. We started by identifying all point sources in the J -band images using the IDL `find` procedure (from *Astrolib*) and then fitted a 2D Gaussian function to each of them to get a more precise position. At this step, sources with an elongated PSF were rejected, as a first attempt to exclude extra galactic contaminants. We also rejected sources too close to the edge of the field (for F2 or GMOS-S) and sources that were saturated in either band. We used coordinates measured in our J -band images to identify sources in the z'_{ab} -band images. In both bands, we used aperture photometry with a radius of 1 FWHM and a sky sampling annulus extending between 2 and 3 FWHM to retrieve the instrumental flux of each source. We kept only point sources detected at 7σ in J , 5σ in [4.5] and 3σ in [3.6]. At a distance of > 20 pc, which is the case for 90% of the stars in our sample, a radius of 5000 AU fits in the field of view of the *Spitzer*/IRAC images. For that reason,

we searched for candidates only inside a projected separation of 5000 AU from the target stars.

We found the center of the target star by fitting a 2D Gaussian to the PSF, for stars that were not saturated. However, most of our targets were saturated in our J -band images. Thus, we used the *Gaia* DR1 DR1 catalog (Gaia Collaboration et al. 2016) to find an approximated position of the star. We then used the known proper motion of the star to compute the position at the time the image was obtained. If *Gaia* data were not available, we fitted a 2D Gaussian to the PSF, where all of the saturated pixels were given the maximum value possible for a pixel. For the IRAC images, the center of the stars was obtained during the PSF removal process.

3.2.1. Colors

For the ages of our target stars, 10–150 Myr, the transition between brown dwarfs and planets happens between L1/L2 and L5/L6 based on AMES.Cond models (Baraffe et al. 2003). As mentioned above (and see Figure 2), early-type L dwarfs have a $z'_{ab} - J$ color $\gtrsim 2.5$ mag. Considering our errors on magnitudes and zero points, we selected only sources with $z'_{ab} - J > 2.2$. Per the above discussion, this same color cut is also sensitive to T and Y dwarfs, which can be identified either through detection in both bands or as z'_{ab} dropouts (in the cases without detection in z'_{ab} , we get only a lower limit on the $z'_{ab} - J$ color). Thus at this stage, we kept all sources with $z'_{ab} - J > 2.2$ mag, including all the z'_{ab} dropouts.

As a second step, we removed any source that has a counterpart in the *Gaia* DR1 DR1 catalog (Gaia Collaboration et al. 2016). *Gaia* can detect objects with magnitude as low as $G=20$. Based on the relationship between $G - J$ and the spectral type of L dwarfs from Smart et al. (2017), using the expected J magnitude of L dwarfs from Faherty et al. (2016), and assuming a distance of 42 pc (the median distance of our sample), the cut in *Gaia* magnitudes rejects objects earlier than $\sim L2$.

Then, we compared the $z'_{ab} - J$ colors and [3.6]–[4.5] colors of our candidates to typical colors of ultracool field dwarfs (Dupuy & Liu 2012), see Figure 7. This figure shows all point sources in a radius of 5000 AU in the J -band image for an average target of the sample for which there was no candidate detected. The solid black line represents the expected colors for L to T dwarfs according to Dupuy & Liu (2012). We kept as candidates only the detections with [3.6]–[4.5] ~ 0.1 to 2 mag, as this is the expected interval for T dwarf's colors. We also kept as candidate source with $M_J < 16$ mag and [3.6]–[4.5] < 1 mag or $M_J > 16$ mag and [3.6]–[4.5] > 1 mag. Figure 6, right, presents the flowchart of the candidate selection for the candidates detected in the J band.

In some cases, a source was detected at 5σ in our IRAC data but we found no counterpart in our J or z'_{ab} imaging,

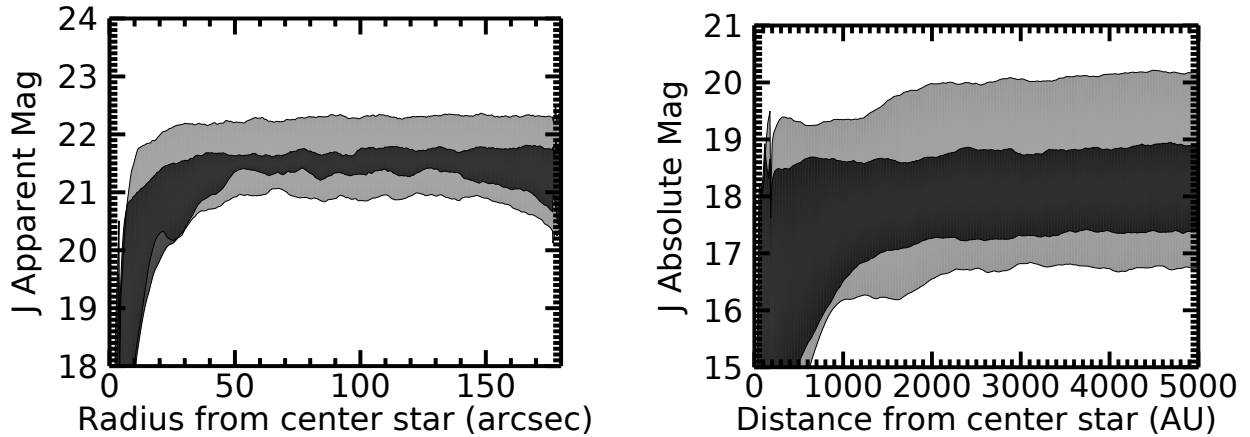


Figure 4. Detection limits for all of our stacked J -band images observed with Flamingos-2 at Gemini-South or WIRCcam at CFHT. The left panel shows limiting apparent magnitudes as a function of the projected separation from the target star in arcseconds. The right panel shows the corresponding absolute magnitudes at the distance of the star as a function of projected separation from the star in AU (with a cutoff at 5000 AU). 50% of the detection limit curves fall inside the black region while the grey region contains 80% of the curves.

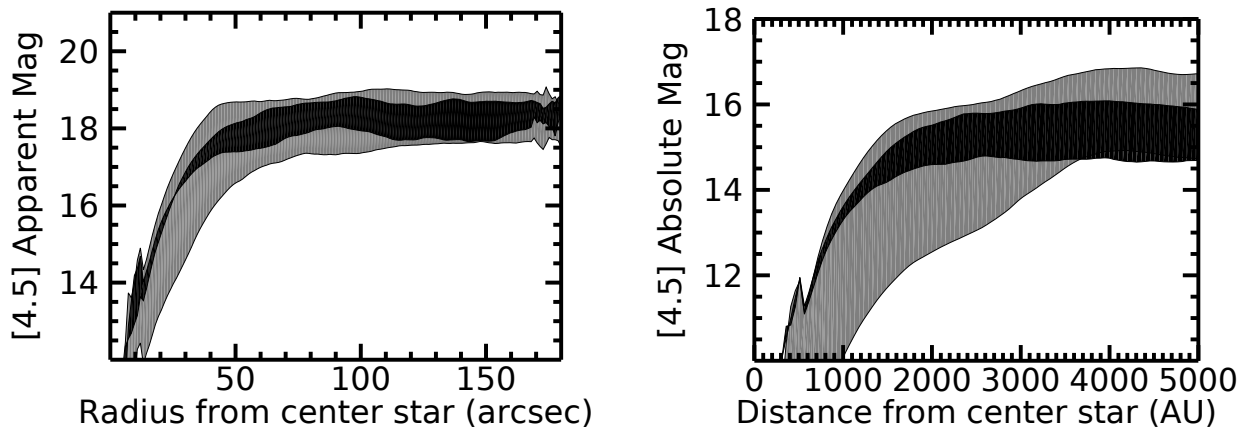


Figure 5. Same as 4 for the *Spitzer*/IRAC observations.

respectively at 7 and 3σ . Unambiguous IRAC-only detection of planets is possible only if $[3.6] - [4.5] > 2$, which corresponds to our detection limits of ~ 21 in the J band, or $M_J \sim 18$ (T8.5) at 50 pc according to AMES.Cond models. However, most of our IRAC-only detection had $0.5 < [3.6] - [4.5] < 2$. As the color in those bands for young 2 Mjup objects is rather uncertain, we decided to follow-up these sources anyway. Thus from the IRAC-only detection, we selected only sources with $[3.6] - [4.5] > 0.5$ and no *Gaia* detection. In addition, as the absolute magnitudes of young planetary mass objects analog to T dwarfs are not well known, we kept only sources with a [4.5] absolute magnitude within 0.75 mag from the typical values of field T dwarfs, see Figure 8. This method has uncovered 79 candidates with the expected colors of T dwarfs. Figure 6, on the right, presents the flowchart of the candidate selection for the candidates not detected in the J band.

The color criteria above yielded typically a few candidates per field. However, most were easily discarded by either

looking at the stacked images or the individual frames: some had an elongated PSF that escaped our automatic cut, some fell out of the detector in one or more frames of the dither pattern biasing their photometry, some were due to a persistence signal from a bright star that was on the same part of the detector in a previous frame (for the WIRCcam images), and some fell over the spider diffraction spikes of the host star. After these initial verifications, our search yielded 4 candidates with J -band detection and 48 candidates with IRAC-only detections.

3.2.2. Cross-match with the 2MASS catalog

The detection method described earlier is not sensitive to companions with spectral type earlier than early L dwarf. Instead, the latest M to early L-type dwarf companions can be identified through a search for common proper motion based on a comparison of our J -band images with 2MASS images, given the ~ 15 years baseline between them. We performed such a proper motion comparison for all sources with $J < 16.5$ mag.

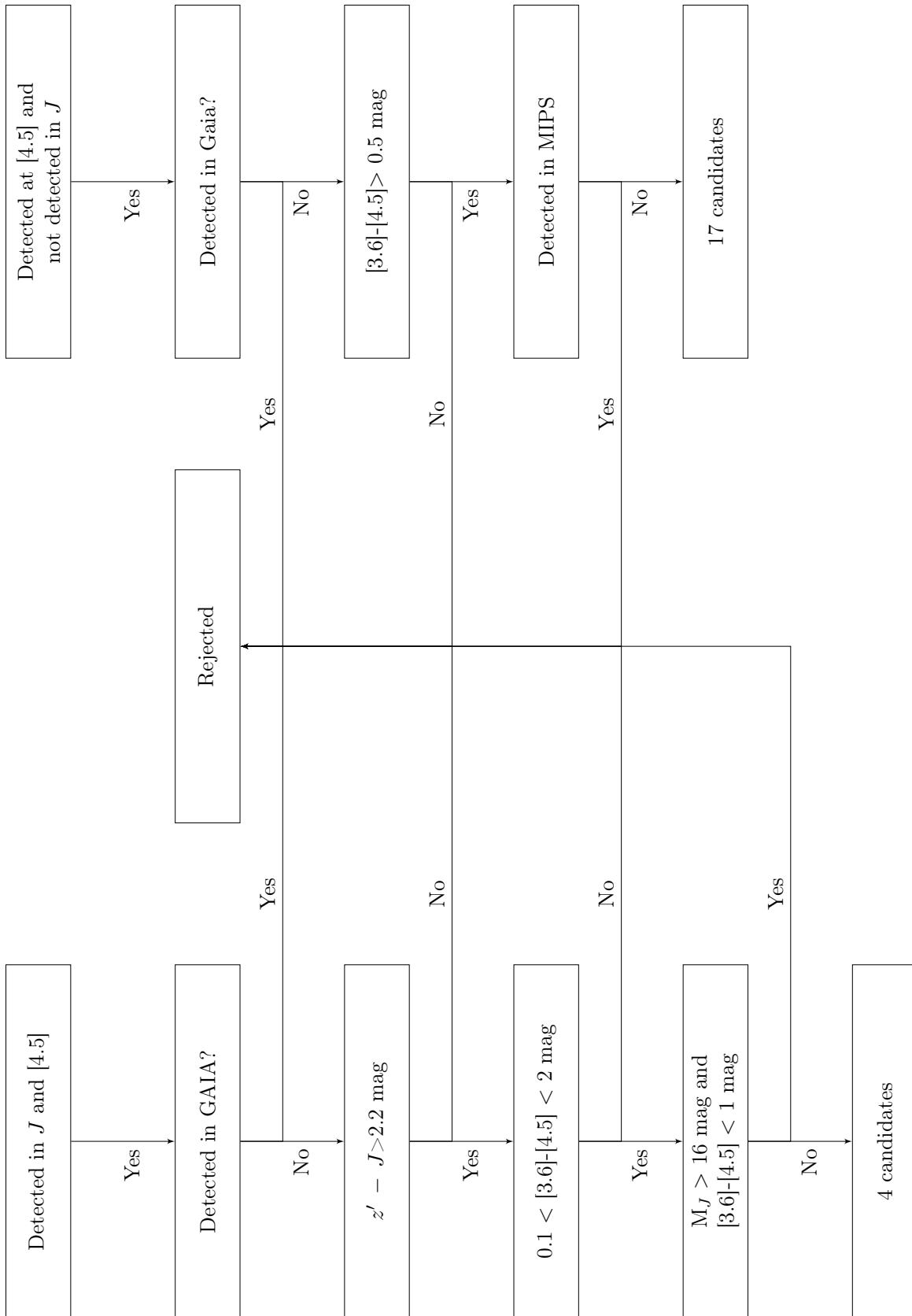


Figure 6. Flowchart of the candidate selection for candidates detected in the J -band on the left and the IRAC-only candidates on the right.

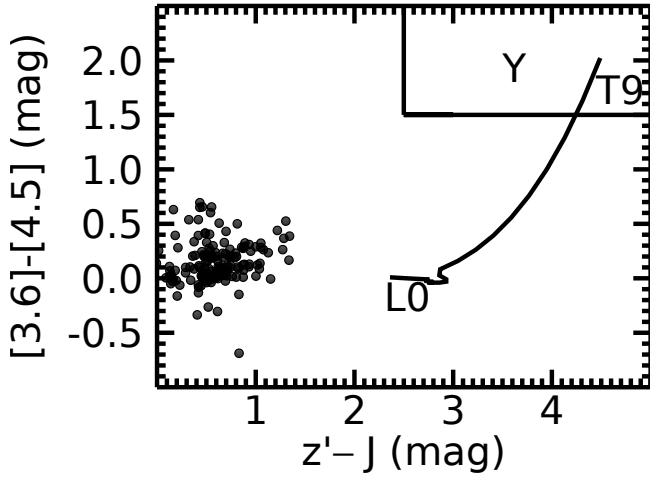


Figure 7. Color-color diagram for HIP 26453, a known member of Columba. The dots represent all sources detected in our J -band imaging, and without detection in *Gaia*, within a radius of 5000 AU from the target star. The solid line shows the expected color sequence for spectral types L to T from Dupuy & Liu (2012). The box represents the expected colors for early Y dwarfs. No candidates were detected in this field.

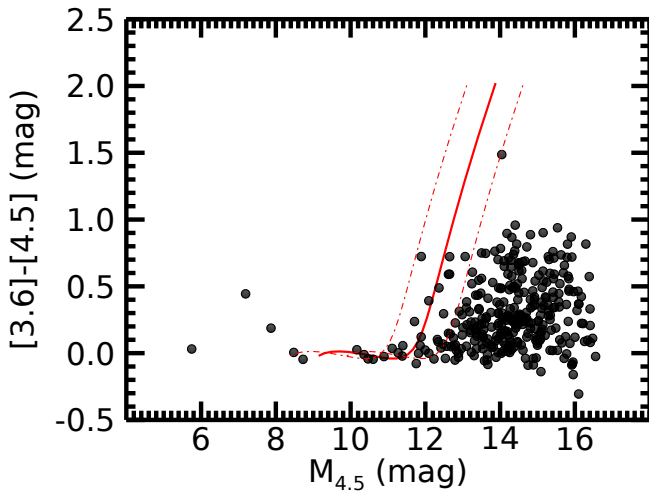


Figure 8. $[3.6]-[4.5]$ color of sources detected in our *Spitzer*/IRAC imaging of HIP 11152 versus their $[4.5]$ absolute magnitude at the distance of the target star. The solid red line corresponds to the colors of M6 to T9 dwarf from Dupuy & Liu (2012). The dotted lines on either sides represented a spread of 0.75 magnitude. The dots are all the point sources presents in a sphere of 5000 AU around the central star for which there is no detection in the optical. One point source has colors consistent with a late T dwarf at the right absolute magnitude. This point source is not detected in the z'_{ab} nor J images. While it is expected for a planetary mass companion to be undetected in z'_{ab} , it should have been detected in J images, given our detection limits. It is thus likely that the candidate is in fact an extragalactic contaminant.

This search identified one candidate with a proper motion consistent with a target star. It is TWA30B, an M4V dwarf

companion of TWA30 – an M5 dwarf member of the TW Hydrae association – at a separation of 3400 AU and which was discovered previously by Loper et al. (2010).

3.2.3. Follow-up of candidates

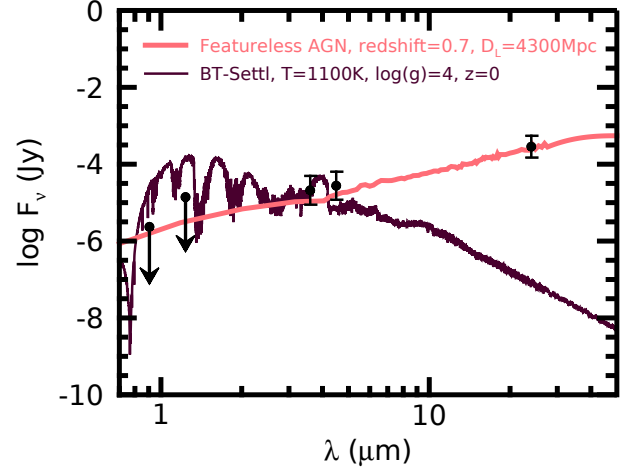


Figure 9. Photometric data for one candidate that has a large $[3.6]-[4.5]$ color but no detection in z'_{ab} and J . The data are compared to the model spectrum of an object with a $T_{\text{eff}} = 1100$ K, $\log g = 4$ and $z = 0$ from BT-Settl (purple) and to the spectrum of a featureless AGN with a redshift of 0.7 and a $D_L = 4300$ Mpc (magenta, from Kirkpatrick et al. 2012a). We see that the detection at $24 \mu\text{m}$ makes it very easy to untangle between a mid-T dwarf and a AGN.

The follow-up of our candidate companions includes 3 different types of observations. First of all, IRAC-only detections were studied in greater details by using MIPS data. A photometric follow-up was obtained to try to identify puzzling objects with very red $[3.6]-[4.5]$ colors and no detection in the z'_{ab} and J bands. Lastly, a proper motion follow-up was obtained for all candidates detected in J that survived the color cuts and verifications.

Our search for candidates in the *Spitzer*/IRAC images yielded 48 candidates with $[3.6]-[4.5] > 0.5$ and no detection in z' or J . Figure 8 shows all the point sources detected in $[3.6]$ and $[4.5]$ in a given field and for which no visible counterpart was found (from the *Gaia* DR1 catalog). Faint, red objects like this certainly constitute interesting planetary mass candidates, as indeed it is expected for such objects to be z' dropouts. Yet given our limits it is unexpected for them to be unseen in J . Other astrophysical sources that may have similar photometric properties include galaxies and active galactic nuclei (AGNs).

Figure 9 shows the expected SED of a low-mass object with an effective temperature of 1100 K compared to the SED of a featureless AGN. As the Figure illustrates, it is difficult to untangle AGNs from planetary candidates using $[3.6]$ and $[4.5]$ photometry alone, but photometry at $24 \mu\text{m}$ is a very

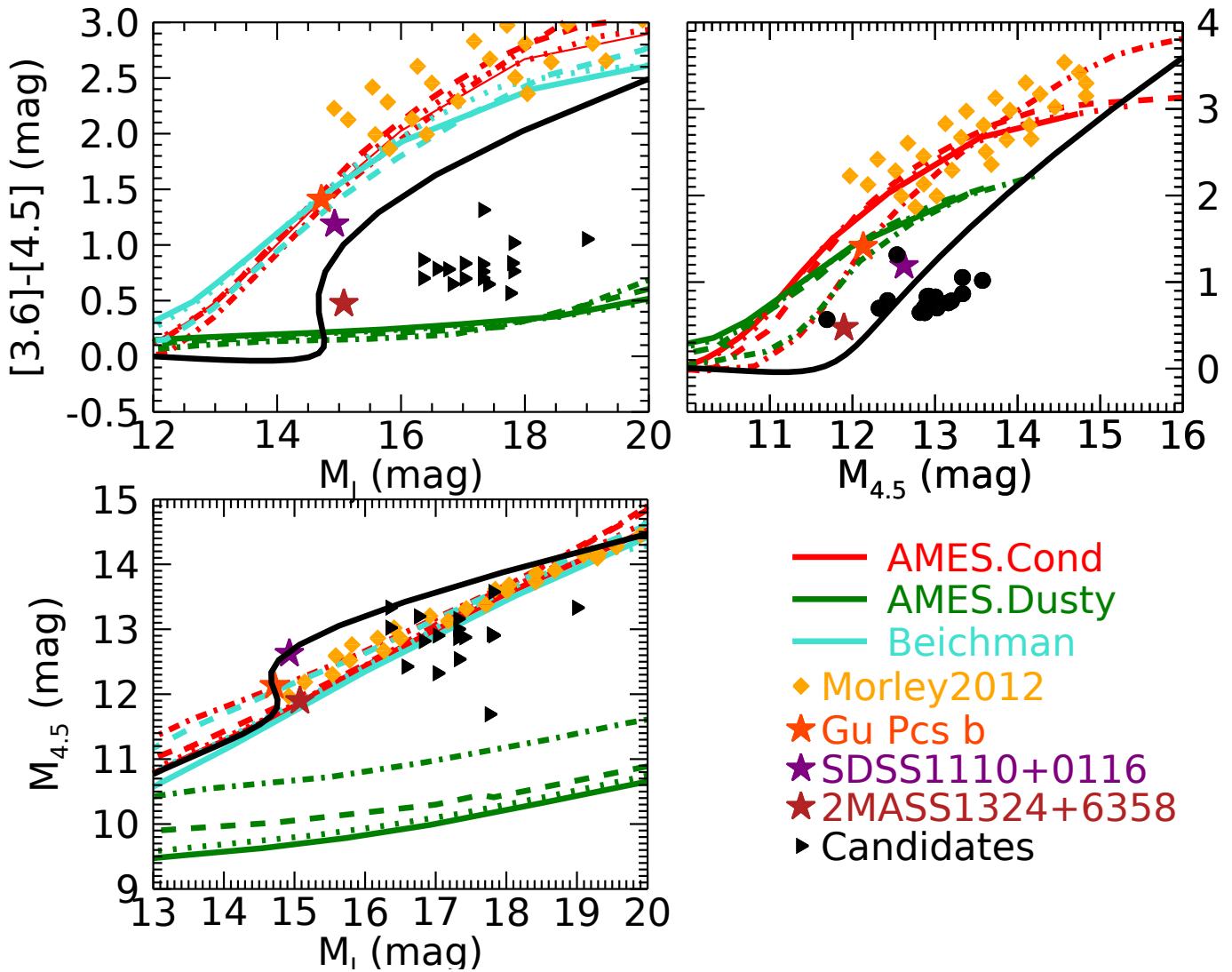


Figure 10. Colors of our 17 *Spitzer*/IRAC-only candidates remaining after the MIPS detection cut (triangles, upper limits in J -band). $[3.6]-[4.5]$ colors versus absolute J magnitude are shown on the upper left while $[3.6]-[4.5]$ colors versus absolute $[4.5]$ magnitudes are displayed on the upper right. The lower left shows absolute $[4.5]$ magnitudes vs absolute J magnitudes. Colors for M6 to T9 dwarfs from Dupuy & Liu (2012) are shown with a black line. The red curves represent the Ames.Cond (Baraffe et al. 2003) at 10, 20, 120 and 5000 Myr, using respectively the solid, dotted, dashed and dash-dotted line. Also shown are models from Beichman et al. (2014) in cyan, Mordasini et al. (2012) in yellow and Ames.Dusty in green. Photometric data for 3 young T dwarfs are also shown by an orange star for Gu Psc b (Naud et al. 2014), a purple star for SDSS1110+0116 (Gagné et al. 2015a) and a red orange star for 2MASS1324+6358 (Gagné et al. 2018a). While the candidate companions have similar $[3.6]-[4.5]$ colors versus $[4.5]$ as the young T dwarfs, they are too faint in the J -band to be considered planetary objects.

good discriminator. We used the MIPS $24 \mu\text{m}$ images mentioned above, reaching a limiting magnitude of 12.5 at 1σ in that band for most targets, to see if our candidates were detected at that wavelength, which would be incompatible with a planetary mass object. This enabled us to reject 31 of our remaining IRAC-only candidates and to identify them as extra-galactic contaminants. We checked archives to see if those MIPS detection are associated with X-ray or radio emission, but none of them are already known as AGN.

After this cut, 17 IRAC-only candidates remain. Figure 10 shows the colors and magnitudes of the candidates

compared to different models as well as to photometric data from known young T dwarfs. Of those 17 candidates, 4 were observed by MIPS but not detected. These candidates have $[3.6]-[4.5] = 0.7$ to 0.9 mag and $[4.5]$ magnitudes between 15.8 mag and 17.5 mag. Using only their IRAC color and assuming that they are T dwarfs and that the BT-Settl/Ames.Cond model are valid, one would expect them to have $M_J \sim 15$ mag, which would have been detected by our survey. As these candidates show no detection in our J -band imaging, we rejected those 4 candidates. The last 13 candidates were not observed by MIPS. Those candidates have

[3.6]–[4.5] colors between 0.6 mag and 1.3 mag and [4.5] magnitudes between 15.2 and 16.9 mag. Using the same thought process as for the candidates not seen in MIPS, we see that those candidates also should have been seen in the J band, but they were not detected. We thus reject the last 13 candidates such that no IRAC-only candidate remain. However, we decided to list those 17 rejected candidates in the interest of completeness, as we cannot identify the nature of the candidates at this stage, and because models might not reproduce accurately the colors of young late T to early Y dwarfs. Table 8 lists them all, with their RA, DEC, associated host star, limiting magnitude in z' and J , apparent magnitude in [3.6] and [4.5], separation in AU from the host star, and distance of the host star in pc. These unknown objects are possibly Ultra Luminous Galaxies (ULIRGS). ULIRGS are identified by their red [3.6]–[4.5] > 0.5 colors meaning that they share colors with T dwarfs. Daddi et al. (2007) have shown that ULIRGS from the GOODS sample, with $0.7 < z < 1.3$ have a space density of $2 \times 10^{-5} \text{ Mpc}^{-3}$. At a luminosity distance corresponding to a redshift of $z=1$, about 3 ULIRGS should have been found per *Spitzer*/IRAC field. As ULIRGS have $F_\nu \sim 10 \mu\text{Jy}$ for $z \sim 1$ to 2 (Kirkpatrick et al. 2012b), they are expected to be detected in our images.

A proper motion follow-up was obtained for all 4 candidates identified through their $z' - J$ and [3.6]–[4.5] colors. It was carried out between 2016 and 2017 both at CFHT and at Gemini-South. Table 9 lists the candidates with their RA, DEC, host stars, $M_{z'}$, M_J , $M_{3.6}$, $M_{4.5}$, separation in AU, pmra, pmdec and the number of sigma at which the proper motion of the candidate differ from the host star’s proper motion. The candidates are rejected at 3σ or higher.

4. ANALYSIS AND DISCUSSION

4.1. Sensitivity and completeness

For each image of our survey, the sensitivity to planets of a given semi-major axis and mass can be determined using the limiting magnitude reached as a function of the projected separations from the star and the corresponding fraction of pixels where a companion could have been detected. In computing these detection completeness maps for all stars in our sample, we adopted an approach similar to that of Nielsen et al. (2008) and Naud et al. (2017), relying on a Monte Carlo simulation.

First, for a given image and a given separation from the star, the fraction of clean pixels, i.e., pixels where a companion could have been detected if indeed it was present, was simply determined by counting pixels at that separation that were not flagged as bad, not saturated, and not affected by the presence of a star. Figures 11 and 12 show this fraction as a function of separation from the star for the J -band images and the [4.5]-band images, respectively. In most cases, at $10''$ the fraction reaches 0.9 for the J -band images and 0.98 for the

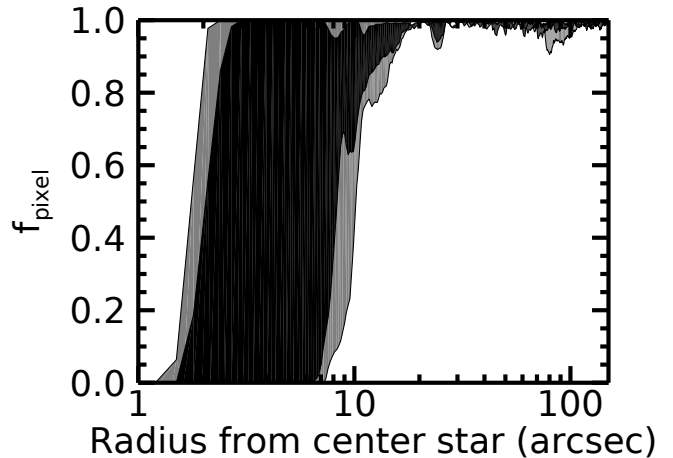


Figure 11. Fraction of clean pixels where a companion could be detected as a function of the separation from the target star in the J -band images. 50% of the stars have a fraction of pixel that is included in the black area while the grey area represents 80% of the stars. For most stars, the fraction of clean pixels reaches 90% at $10''$.

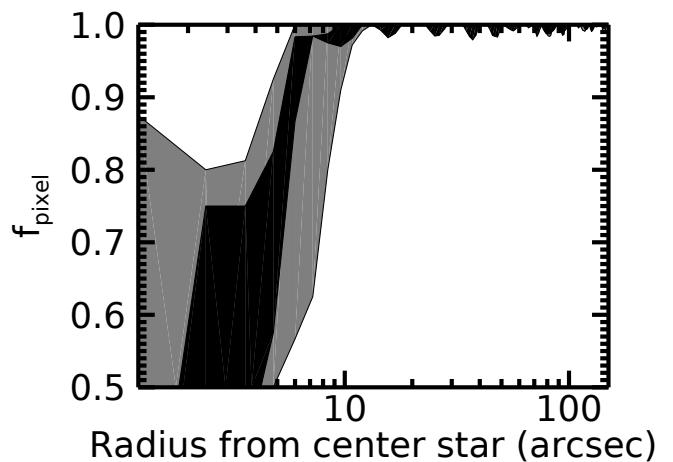


Figure 12. Same as 11 for *Spitzer*/IRAC observations at [4.5]. For most stars, the fraction of clean pixels reaches 98% at $10''$.

[4.5]-band images. In a few cases, the target star is in the galactic plane, making the detection of a companion harder and the fraction lower. Huge variations in f_{pixel} at smaller separations come from the different magnitude of the central stars, and the associated different areas affected by saturation. Some stars of the sample are very saturated and thus f_{pixel} is very low at small separation while the M dwarfs of our sample are not saturated and thus a higher f_{pixel} is reached at smaller separations. In general, the fraction of pixel for an individual target can be fitted by a logistic function with the shape of $1/(e^{-a_0(x-a_1)} + e^{a_2})$, where a_0 is the steepness of the curve, a_1 is the x -values of the mid point and a_2 is typically close to 0. Table 9 and Table 10 show the values of the 3 parameters for each target of the sample for the J -band and

[4.5] images respectively (a_0 varies from -10 to 40, a_1 goes from 0 to 14, and a_2 is close to 0).

Next, we defined a grid of masses and semi-major axes, with the masses equally spaced in logarithmic scale between 0.5 and 15 M_{Jup} and the semi-major axes equally spaced in logarithmic scale between 100 and 5000 AU. For each point of the grid, we simulated 10^4 planets. Each planet has an eccentricity taken randomly from the eccentricity distribution reported in Kipping (2013), which is taken from the eccentricity from RV planets. Then we used the method of Branderker et al. (2006) and Brandt et al. (2014) to find the instantaneous projected separation of each planet, given their eccentricity, semi-major axis, and some random inclination and time of observation. The projected separation in AU was finally converted to a projected angular separation in arcsec by dividing by the star distance, which is sampled uniformly within its interval of uncertainty.

For each grid point, we converted the mass into a J -band absolute magnitude using the AMES.Cond evolution models (Baraffe et al. 2003) and the ages of the targets from Table 1 and Table 3. We randomly sampled the age of each generated planet uniformly between the uncertainties given for the appropriate moving group (see Table 1). We then used the known distance of the star to convert the planets' absolute magnitudes to apparent magnitudes, and compared these to the detection limits found earlier to assess the detectability of each planet. If a planet was brighter than the detection limit, we used the fraction of clean pixels found earlier at that separation as the detection probability; otherwise the planet was assigned a detection probability of zero. This was repeated for each simulated planet, and the results were averaged to find the probability of detection at each point of the grid.

This procedure was repeated for all targets of the sample. The sensitivity of the whole survey was calculated by taking the median of all the detection probability maps. Two completeness maps were made this way, one for the J -band images (Figure 13, left) and one for the [4.5]-band images (Figure 13, right). The ground-based survey is mostly sensitive to objects with masses higher than 2 M_{Jup} with a semi-major axis of more than 1000 AU while the *Spitzer* survey is sensitive to planets slightly less massive (down to 1 M_{Jup}) at larger separations.

The completeness maps for each star of the sample and for both J and [4.5] bands were combined to build the overall completeness map of the survey. For each star at each point of the grid, the highest probability was taken between the completeness map of the J -band images and the [4.5] images. The two-band combined completeness maps were then averaged over all stars to obtain the overall survey completeness maps, see Figure 14. Figure 15 shows the mean detection probability as a function of semi-major axis for planetary objects with masses of 1 M_{Jup} , 2 M_{Jup} , 3 M_{Jup} and 13 M_{Jup} , taken

from the overall completeness map of the survey. The maximal probabilities of detection are respectively 64%, 95%, 98%, and 99%. Our survey is mostly sensitive to planets with masses of 2 M_{Jup} and above, as the detection probability falls very rapidly between 2 and 1 M_{Jup} .

Our results probe an area of the semi-major axis–mass diagram that has not been studied before. Figure 14 shows our completeness map compared to the regions probed by the following other studies: the PSYM-WIDE survey (Naud et al. 2017), aiming at discovering planetary mass objects on wide orbits around K5-L5 dwarfs, the PALMS survey (Bowler 2016), a deep coronagraphic study of 78 single young nearby (<40 pc) M dwarfs, the GPDS survey (Lafrenière et al. 2007b), a survey of young stars searching for giant planets on large orbits, the NaCo Survey of Young Nearby Dusty Stars (Rameau et al. 2013), which targeted 59 young nearby AFGK stars, the NaCo-LP survey (Chauvin et al. 2015), which focused on 86 young, bright, and primarily FGK stars, the IDPS-AF survey (Vigan et al. 2012), which observed 42 AF stars, the MMT L' and M-band Survey of 54 nearby FGK stars (Heinze et al. 2010), the Gemini NICI Planet-finding Campaign (Biller et al. 2013), which targeted 230 young stars of all spectral types, MASSIVE (Lannier et al. 2016), which targeted 58 young and nearby M-type dwarfs, the IDPS survey Galicher et al. (2016), which combine results for 292 young nearby stars and Durkan et al. (2016) who studied 121 nearby stars observed with *SPITZER*/IRAC. On the whole, this survey is a good complement to AO imaging surveys, being mostly sensitive at separations of several hundreds of AU but insensitive at semi-major axes of less than ~ 150 AU, where AO imaging surveys are most sensitive.

4.2. Constraints on additional companions in systems with known directly imaged companions

At least one planetary mass or brown dwarf companion was previously found around 6 stars in our sample; most of these companions were found using high-contrast AO imaging. Our search, being sensitive to much wider separations and reaching lower masses, adds valuable constraints on the presence of additional companions in these systems. We provide in Figure 16 the individual completeness maps from our survey for these six systems.

The companion Pz Tel B, a $36 \pm 6 M_{\text{Jup}}$ brown dwarf orbiting at 16.4 ± 1 AU from a pre-main sequence G9 star member of the β -Pictoris association, was found by Biller et al. (2010) using VLT/NACO. We put constraints on the presence of companions at larger orbits (see Figure 16, top left). At a confidence level of more than 90%, we can reject a companion with masses as low as 1–2 M_{Jup} at 2000–5000 AU.

The companion 2M1207 b, a $4 \pm 1 M_{\text{Jup}}$ object (Chauvin et al. 2004) orbiting at 46^{+37}_{-15} AU (Blunt et al. 2017) around the young brown dwarf TWA27, member of the TW Hydrae

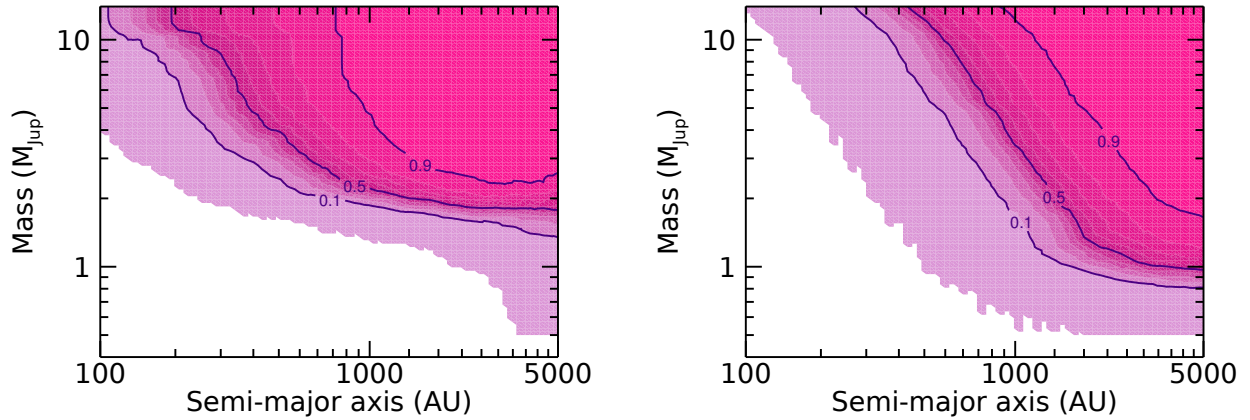


Figure 13. Completeness map for the J -band images on the left and for the $[4.5]$ images on the right. They show the probability of detecting a planet with a mass between 1 and $13 M_{\text{Jup}}$ as a function of the separation from the host star. Curves for 10%, 50% and 90% are shown.

association at 52 pc, was discovered using VTL/NACO. Our survey put strong constraints on the presence of $> 10 M_{\text{Jup}}$ objects in the system, as they should have been detected at separations from 100 to 5000 AU. Moreover, at a distance of 1000 AU, the detection probability of $1 M_{\text{Jup}}$ object is about 80%. Our survey covers quite well the regime of separations > 1000 AU and masses $> 1 M_{\text{Jup}}$ (see Figure 16, top right). No companion was detected by our survey.

Chauvin et al. (2005) found a $13.5 \pm 0.5 M_{\text{Jup}}$ object at 250 AU of AB Pic, a K2V star member of the Tucana-Horologium association, by using VLT/NACO. Figure 16, middle left, presents the completeness reached by our survey. We put strong constraints on the presence of companions of $2 M_{\text{Jup}}$ or more at separations higher than 1000 AU.

Marois et al. (2008, 2010) used AO observations with Keck/NIRC2 and Gemini/NIRI to find 4 planets of 7_{-2}^{+4} , 10_{-3}^{+3} , 10_{-3}^{+3} and $9_{-4}^{+4} M_{\text{Jup}}$ at respectively ~ 68 , 43, 27 and 17 AU from HR 8799 (Wertz et al. 2017), an A5V star member of the Columba association. We probed a region in mass that is equivalent to the planets already known, but at much larger semi-major axes. We put good constraints on the presence of companion with $\geq 4 M_{\text{Jup}}$ and semi-major axis greater than 1500 AU.

Lagrange et al. (2009) found a $12.7 \pm 0.3 M_{\text{Jup}}$ (Morzinski et al. 2015) planet at $9.2_{0.4}^{+1.5}$ AU (Millar-Blanchaer et al. 2015) orbiting β Pictoris, an A6V star member of the β Pictoris association, using high-contrast VLT/NACO observations. Our observations put strong constraints on the existence of objects of $1 M_{\text{Jup}}$ or more at semi-major axes of > 1000 AU.

A $1-2 M_{\text{Jup}}$ ² (Rajan et al. 2017) object orbiting 51 Eri at ~ 14 AU, an FOIV star, was found by Macintosh et al. (2015) using Gemini/GPI. 51 Eri is part of a triple system, bound

² This mass was inferred from hot start model from (Marley et al. 2007). It is also possible that the mass is anywhere between 2–12 M_{Jup} according to the cold start model from Fortney et al. (2008).

to and separated by ~ 2000 AU from GJ3305AB, an M+M binary of unresolved spectral type M0 (Montet et al. 2015). Our survey put strong constraints on the presence of companions of mass $> 1 M_{\text{Jup}}$ at semi-major axes between 100 and 5000 AU.

4.3. Planet frequency

Based on the null result of our survey, and our completeness limits calculated in section 4.2, we evaluated an upper limit to the frequency of occurrence of planets at large semi-major axis (1000–5000 AU), following the method developed by Lafrenière et al. (2007b).

If we have $N=177$ stars enumerated from $j=1$ to N , and we survey an interval of mass going from 1 to $13 M_{\text{Jup}}$ and an interval of semi-major axis of 1000 to 5000 AU, then we define f to be the fraction of stars with at least one companion in the intervals and p_j the probability of detecting such a companion. This probability is computed from the completeness map calculated previously by taking the mean of the probability at each point of the 100×100 grid. Since the grid is uniform in logarithmic space, this amounts to assuming that the semi-major axis and the mass are distributed uniformly in log. The detections in the survey are characterized by the set $\{d_j\}$, and in our case, since the survey gave a null result (all known companions around our targets were too close-in to be seen in our data), $d_j=0$ for all j . The probability of observing the set $\{d_j\}$ in our survey is given by the following binomial likelihood,

$$\mathcal{L}(\{d_j\}|f) = \prod_{j=0}^N (1 - f p_j)^{1-d_j} (f p_j)^{d_j}. \quad (1)$$

Then according to Bayes theorem, the posterior distribution for f , in light of our results, is given by,

$$p(f|\{d_j\}) = \frac{\mathcal{L}(\{d_j\}|f)p(f)}{\int_0^1 \mathcal{L}(\{d_j\}|f)p(f)df}, \quad (2)$$

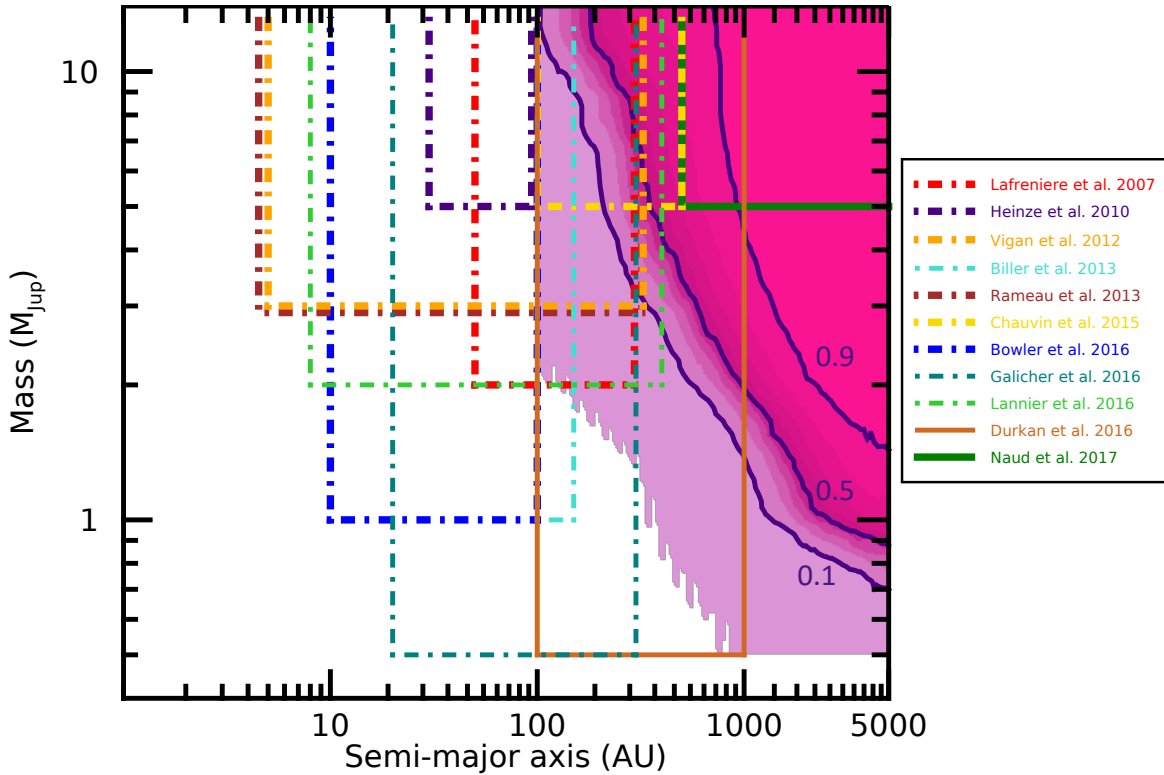


Figure 14. Overall completeness map for our survey. Our results are shown in shades of magenta and the contours correspond to the probability of detecting a planet of a giving mass and semi-major axis. The solid green box is the PSYM-WIDE survey (Naud et al. 2017), the solid brown box is the survey of Durkan et al. (2016), and the dashed-dotted boxes correspond to high contrast direct imaging surveys: PALMS in blue (Bowler 2016), GPDS in red (Lafrenière et al. 2007b), NaCo Survey of Young Nearby Dusty Stars (Rameau et al. 2013) in brown, NaCo-LP in yellow (Chauvin et al. 2015), IDPS-AF in orange (Vigan et al. 2012), MMT L' and M-band Survey of Nearby Sun-like Stars (Heinze et al. 2010) in purple, Gemini NICI Planet-finding Campaign (Biller et al. 2013) in turquoise, MASSIVE in lime green (Lannier et al. 2016) and IDPS in olive green (Galicher et al. 2016). Our observations probe larger semi-major axes than AO imaging surveys, but are insensitive to semi-major axes where AO observations are mostly sensitive.

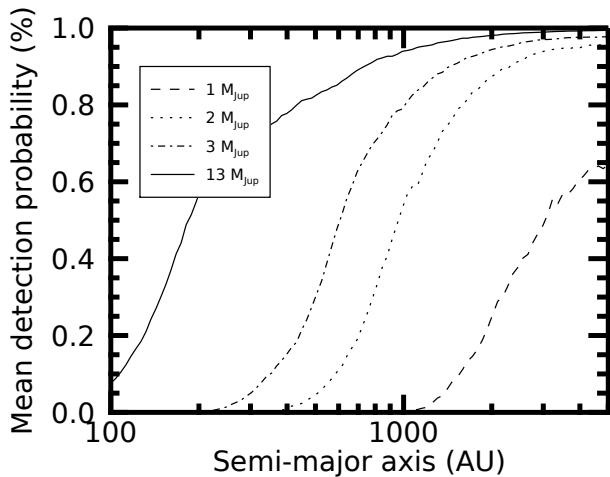


Figure 15. Mean detection probability for $1 M_{\text{Jup}}$ (dash), $2 M_{\text{Jup}}$ (dot), $3 M_{\text{Jup}}$ (dash-dot) and $13 M_{\text{Jup}}$ (solid) companions as a function of the semi-major axis in AU.

where $p(f)$ is the prior probability on f , reflecting our state of knowledge independently of our new data. One has to be

careful in the choice of the prior, and here we elected to use a non-informative Jeffrey's prior (see Berger et al. 2009), given by,

$$P(f) = \frac{1}{\pi} \frac{1}{\sqrt{f}} \frac{1}{\sqrt{1-f}}. \quad (3)$$

For our survey with no detection, the posterior distribution of f peaks at 0, and we can only set an upper limit on f (by integrating the posterior from 0 to the fraction f that give a probability matching the desired confidence level).

We obtained an upper limit for the fraction of stars with at least one planet of $f_{\text{max}} = 0.03$ at a 95% confidence level, for planets with masses between 1 and $13 M_{\text{Jup}}$ and semi-major axis between 1000 and 5000 AU distributed uniformly in log space.

5. CONCLUSIONS

A sample of 177 young stars, bona fide members of moving groups, were observed between 2014B and 2017B by CFHT's MegaCam in the z'_{ab} -band and WIRCcam in the J -band, or Gemini GMOS-S in the z'_{ab} -band and Flamingos-2 in the J -band, as well as with *Spitzer*/IRAC at [3.6] and [4.5]

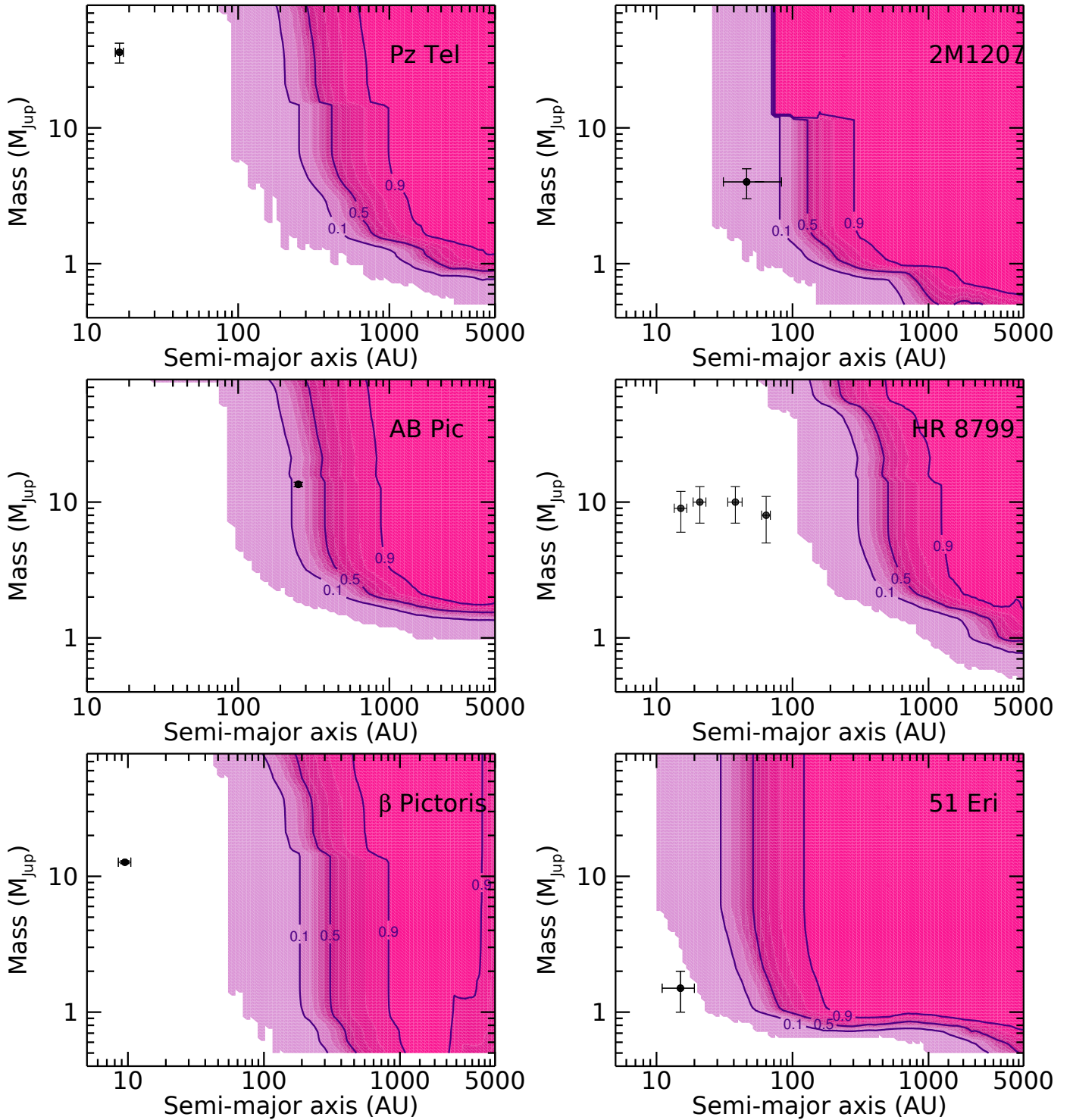


Figure 16. Contrast curves for Pz Tel, 2M1207, AB Pic, HR 8799, β Pictoris and 51 Eri. Known companions are shown as black points with error bars, using masses from hot start models. See text for references for the masses.

to search for planetary mass companions on very wide orbits (up to 5000 AU). The survey made use of the very red $z'-J$ and $[3.6]-[4.5]$ colors intrinsic to such objects and reached good sensitivities down to objects of $1 M_{\text{Jup}}$. Four candidates were identified through colors selection but proper mo-

tion follow-up obtained a year after the first epoch rejected the candidates. No planet was found. This null result allowed us to set an upper limit of 0.03 for the fraction of stars with at least one planet with mass between 1 and $13 M_{\text{Jup}}$ and semi-major axis between 1000 and 5000 AU, at a 95%

confidence level, assuming logarithmically uniform distributions in planet mass and semi-major axis. While it was not the main objective of the survey, our data also constrain the frequency of brown dwarfs to be less than 2.2% for objects with masses between 13 and $80 M_{\text{Jup}}$ and for semi-major axis between 1000 and 5000 AU.

As mentioned above, the formation process by which Jupiter-like objects on wide orbits form has been the subject of an ongoing debate. The very low occurrence rate for planets at 1000-5000 AU found by our survey indicates that neither core accretion nor disk instability is actually efficient at forming gas giants at these large separations. It is possible that the few known instances of planets at such large separations from their host star represent the low-mass tail end of distribution of brown dwarf companions that form like stars, rather than objects that form like planets. More quantitative implications of our results on the properties of the overall distribution of planets around stars, as well as on the formation mechanism of very distant companions will be explored in a forthcoming paper, where we will further incorporate the results of AO surveys.

Based on observations obtained at the Gemini Observatory through programs number GS-2014B-Q-2, GS-2015A-Q-71, GS-2015B-Q-57, GS-2016A-Q-69, GS-2016B-Q-33, GS-2017A-Q-58 and GS-2017B-Q-34. The Gemini Observatory is operated by the Association of Universities for Research in Astronomy, Inc., under a cooperative agreement with the National Science Foundation (NSF) on behalf of the Gemini partnership: the NSF (United States), the National Research Council (Canada), CONICYT (Chile), the Australian Research Council (Australia), Ministério da Ciência, Tecnologia e Inovação (Brazil), and Ministerio de Ciencia, Tecnología e Innovación Productiva (Argentina).

Based on observations obtained with MegaPrime/MegaCam, a joint project of CFHT and CEA/DAPNIA, at the Canada-France-Hawaii Telescope (CFHT) which is operated by the National Research Council (NRC) of Canada, the Institut National des Science de l'Univers of the Centre National de la Recherche Scientifique (CNRS) of France, and the University of Hawaii.

The Pan-STARRS1 Surveys (PS1) have been made possible through contributions of the Institute for Astronomy, the University of Hawaii, the Pan-STARRS Project Office, the Max-Planck Society and its participating institutes, the Max Planck Institute for Astronomy, Heidelberg and the Max Planck Institute for Extraterrestrial Physics, Garching, The Johns Hopkins University, Durham University, the University of Edinburgh, Queen's University Belfast, the Harvard-Smithsonian Center for Astrophysics, the Las Cumbres Observatory Global Telescope Network Incorporated, the National Central University of Taiwan, the Space Telescope Sci-

ence Institute, the National Aeronautics and Space Administration under Grant No. NNX08AR22G issued through the Planetary Science Division of the NASA Science Mission Directorate, the National Science Foundation under Grant No. AST-1238877, the University of Maryland, and Eotvos Lorand University (ELTE) and the Los Alamos National Laboratory.

This work has made use of data from the European Space Agency (ESA) mission *Gaia* (<https://www.cosmos.esa.int/gaia>), processed by the *Gaia* Data Processing and Analysis Consortium (DPAC, <https://www.cosmos.esa.int/web/gaia/dpac/consortium>). Funding for the DPAC has been provided by national institutions, in particular the institutions participating in the *Gaia* Multilateral Agreement.

Facility: Gemini-South (Flamingos-2, GMOS-S), CFHT (WIRCam, MegaCam), Spitzer (Irac)

Software: SExtractor (Bertin & Arnouts 1996), Scamp (Bertin 2010a), Swarp (Bertin 2010b), CFHT'S Elixir pipeline

Table 2. Properties of the sample of bona fide members

Name	RA	DEC	SpT	J	H	K	W1	W2
	(J2000.0)	(J2000.0)						
HIP 490	00 05 52.54	-41 45 11.0	G0V	6.464±0.011	6.189±0.017	6.117±0.013	6.043±0.053	6.053±0.023
HIP 560	00 06 50.08	-23 06 27.1	F3V	5.451±0.017	5.331±0.045	5.240±0.019	5.245±0.072	5.013±0.036
HIP 1113	00 13 53.01	-74 41 17.8	G8V	7.406±0.013	7.087±0.025	6.962±0.017	6.888±0.035	6.932±0.020
HIP 1134	00 14 10.25	-07 11 56.8	F5V	6.402±0.015	6.170±0.035	6.073±0.015	6.049±0.046	5.999±0.024
HIP 1481	00 18 26.12	-63 28 39.0	F8V	6.462±0.007	6.248±0.033	6.149±0.009	6.141±0.048	6.102±0.023
HIP 1910 AB	00 24 08.98	-62 11 04.3	MOV	8.385±0.019	7.708±0.031	7.494±0.015	7.354±0.026	7.306±0.019
HIP 1993	00 25 14.66	-61 30 48.3	MOV	8.615±0.021	7.943±0.037	7.749±0.021	7.606±0.025	7.594±0.020
GJ 2006A	00 27 50.23	-32 33 06.4	M3.5V	8.882±0.032	8.236±0.038	8.012±0.033	7.720±0.021	7.541±0.017
HIP 2484 B	00 31 32.67	-62 57 29.6	A2V	4.664±0.254	4.677±0.075	4.481±0.033	4.604±0.087	4.104±0.042
HIP 2578	00 32 43.91	-63 01 53.4	A0V	5.061±0.033	5.156±0.075	4.985±0.013	5.010±0.068	4.657±0.038
HIP 2729	00 34 51.20	-61 54 58.1	K5V	7.337±0.007	6.721±0.031	6.533±0.011	6.427±0.044	6.443±0.019
HIP 3556	00 45 28.15	-51 37 33.9	M3V	8.481±0.011	7.867±0.019	7.623±0.023	7.509±7.428	7.329±0.026
HD 4277 A	00 45 50.89	54 58 40.2	F8V	6.645±0.009	6.399±0.021	6.361±0.011	6.245±0.047	6.267±0.020
HIP 4448 A	00 56 55.46	-51 52 31.9	K3V	7.040±0.021	6.522±0.045	6.358±0.019	6.340±0.043	6.345±0.021
G 132-51 B	01 03 42.11	+40 51 15.8	M2.6V	9.372±0.036	8.839±0.046	8.513±0.029	8.092±0.022	7.937±0.019
HD 6569 AB	01 06 26.15	-14 17 47.1	K1V	7.909±0.017	7.427±0.031	7.340±0.017	7.258±0.027	7.332±0.020
2MASS J01112542+1526214	01 11 25.42	15 26 21.5	M5V	9.082±0.019	8.512±0.033	8.208±0.029	8.004±0.023	7.791±0.020
CD-12 243	01 20 32.27	-11 28 03.7	G0V	7.026±0.011	6.654±0.039	6.549±0.015	6.533±0.041	6.581±0.021
2MUCD 13056	01 23 11.26	-69 21 38.0	M7.5V	12.320±0.029	11.710±0.033	11.320±0.031	11.060±0.023	10.808±0.021
HIP 6485	01 23 21.25	-57 28 50.7	G6V	7.241±0.013	6.946±0.031	6.847±0.025	6.753±0.037	6.809±0.021
G 269-153 A	01 24 27.68	-33 55 08.6	M4.3V	9.203±0.034	8.659±0.045	8.240±0.030	7.895±0.022	7.720±0.020
HIP 6856	01 28 08.66	-52 38 19.1	K1V	7.405±0.009	6.944±0.021	6.834±0.017	6.765±0.036	6.813±0.020
2MASS J01351393-0712517	01 35 13.93	-07 12 51.8	M4.3V	8.964±0.017	8.387±0.023	8.078±0.029	7.975±0.024	7.795±0.020
G271-110	01 36 55.17	-06 47 37.9	M3.5V	9.707±0.022	9.137±0.026	8.862±0.021	8.684±0.022	8.522±0.020
HIP 9141 AB	01 57 48.98	-21 54 05.3	G3V	6.856±0.015	6.555±0.035	6.472±0.021	6.391±0.045	6.440±0.019
HIP 9685	02 04 35.12	-54 52 54.1	F2V	5.696±0.041	5.489±0.023	5.448±0.011	5.393±0.069	5.237±0.031
HIP 9892 AB	02 07 18.06	-53 11 56.5	G7V	7.347±0.017	6.986±0.039	6.894±0.017	6.865±0.034	6.908±0.019
HIP 9902	02 07 26.12	-59 40 45.9	F8V	6.534±0.011	6.304±0.029	6.204±0.013	6.208±0.046	6.147±0.022
HD 13482 A	02 12 15.41	23 57 29.5	K1V	6.203±0.009	5.827±0.007	5.727±0.007	5.610±0.063	5.582±0.028
HIP 10602 A	02 16 30.59	-51 30 43.8	B8IV	4.026±0.298	3.951±0.262	4.127±0.268	3.881±0.111	3.336±0.059
HIP 10679	02 17 24.74	28 44 30.4	G2V	6.570±0.013	6.355±0.021	6.262±0.009	6.221±0.039	6.251±0.021
HIP 11152	02 23 26.64	22 44 06.7	M3V	8.182±0.007	7.561±0.015	7.346±0.011	7.264±0.027	7.239±0.021
HIP 11360	02 26 16.24	06 17 33.2	F4IV	6.028±0.011	5.863±0.019	5.822±0.015	5.757±0.045	5.646±0.025
HIP 11437 A	02 27 29.25	30 58 24.6	K8V	7.870±0.029	7.235±0.011	7.080±0.021	6.991±0.032	7.039±0.020
1RXSJ022735.8+471021	02 27 37.26	47 10 04.5	M4.6V	10.306±0.021	9.733±0.018	9.461±0.017	9.288±0.023	9.113±0.019
HIP12394	02 39 35.36	-68 16 01.0	B9V	4.443±0.296	4.433±0.270	4.254±0.033	4.201±0.090	3.707±0.058
HIP12413	02 39 47.99	-42 53 30.03	A1V	4.678±0.266	4.620±0.075	4.460±0.019	4.425±0.091	4.066±0.051
HIP 12545 AB	02 41 25.89	05 59 18.4	K6V	7.904±0.021	7.234±0.027	7.069±0.027	6.946±0.034	6.943±0.020
AF Hor	02 41 47.31	-52 59 30.7	M2V	8.481±0.027	7.851±0.034	7.641±0.027	7.374±0.028	7.336±0.019
HIP 12635	02 42 20.95	38 37 21.5	K3.5V	8.377±0.015	7.904±0.051	7.762±0.019	7.735±0.024	7.763±0.021
HIP12925	02 46 14.61	+05 35 33.3	F8V	6.859±0.031	6.632±0.049	6.517±0.033	6.445±0.043	6.466±0.020
HD 17332 A	02 47 27.24	19 22 18.5	G0V	5.868±0.011	5.564±0.011	5.517±0.015	5.117±0.069	5.014±0.024
HIP 13209	02 49 59.03	27 15 37.8	B8V	3.657±0.294	3.803±0.238	3.864±0.033	3.842±0.094	3.296±0.063
HIP 14551	03 07 50.85	-27 49 52.1	A5V	5.891±0.011	5.851±0.051	5.772±0.011	5.722±0.055	5.620±0.028
IS Eri	03 09 42.29	-09 34 46.6	G0V	7.156±0.023	6.794±0.037	6.701±0.021	6.644±0.038	6.681±0.021
HIP 14807	03 11 12.33	22 25 22.7	K6V	8.358±0.017	7.789±0.027	7.652±0.021	7.585±0.025	7.594±0.018
HIP 14913 A	03 12 25.75	-44 25 10.8	A8V+F3V	5.118±0.025	4.931±0.021	4.827±0.013	4.773±0.096	4.403±0.063
HIP 15247	03 16 40.67	-03 31 48.9	F6V	6.457±0.013	6.209±0.021	6.099±0.015	6.031±0.050	5.972±0.025

Table 2 continued

Table 2 (continued)

Name	RA	DEC	SpT	J	H	K	W1	W2
	(J2000.0)	(J2000.0)						
HIP 15353	03 17 59.07	-66 55 36.7	A3V	5.782±0.015	5.752±0.029	5.691±0.021	5.643±0.059	5.540±0.024
CD-35 1167	03 19 08.66	-35 07 00.3	K7V	8.576±0.027	7.919±0.031	7.723±0.023	7.576±0.026	7.607±0.020
CD-44 1173	03 31 55.64	-43 59 13.5	K6V	8.300±0.018	7.679±0.015	7.470±0.021	7.434±0.026	7.426±0.020
V577 Per	03 33 13.49	46 15 26.5	G5V	6.836±0.013	6.457±0.003	6.368±0.017	5.785±0.047	6.102±0.019
2MASS J03350208+2342356	03 35 02.09	23 42 35.6	M8.5V	12.250±0.017	11.655±0.020	11.261±0.014	11.044±0.023	10.767±0.020
HIP 16853 AB	03 36 53.40	-49 57 28.9	G2V	6.492±0.021	6.264±0.035	6.137±0.013	6.020±0.054	6.022±0.022
HIP 17248	03 41 37.24	55 13 06.8	M0.5V	8.347±0.021	7.649±0.023	7.499±0.017	7.436±0.026	7.448±0.021
HIP 17695	03 47 23.43	-01 58 19.9	M2.5V	7.804±0.019	7.174±0.049	6.933±0.019	6.810±0.037	6.684±0.019
HIP 17764	03 48 11.47	-74 41 38.8	F3V	6.367±0.013	6.224±0.043	6.136±0.011	6.112±0.050	6.095±0.022
HIP 17782 AB	03 48 23.00	52 02 16.3	G8V	7.222±0.021	6.859±0.031	6.747±0.015	6.707±6.715	6.687±0.038
HIP 17797	03 48 35.88	-37 37 12.5	A1V	3.900±1.054	4.626±9.996	4.824±0.007	4.763±0.031	4.304±0.021
HIP 18714 AB	04 00 31.99	-41 44 54.4	G3V	7.203±0.009	6.939±0.009	6.875±0.023	6.802±0.042	6.827±0.020
HD 25457	04 02 36.75	-00 16 08.1	F5V	4.712±0.236	4.342±0.075	4.181±0.033	9.654±-9.000	6.076±0.114
HD 25953	04 06 41.53	01 41 02.1	F5V	6.892±0.019	6.695±0.041	6.582±0.017	6.503±0.040	6.563±0.021
IRXS J041417.0-090650	04 14 17.30	-09 06 54.4	M4.3V	9.630±0.024	9.056±0.024	8.755±0.023	8.586±8.432	8.319±0.023
HIP 21547	04 37 36.13	-02 28 24.8	F0V	4.744±0.033	4.770±0.075	4.537±0.019	4.486±0.081	4.085±0.049
HIP 21632	04 38 43.94	-27 02 01.8	G3V	7.273±0.015	6.970±0.029	6.866±0.005	6.861±0.035	6.899±0.022
HIP 21965	04 43 17.20	-23 37 42.0	F2V	6.288±0.011	6.068±0.031	6.023±0.017	5.931±0.058	5.934±0.023
HIP 22295	04 48 05.17	-80 46 45.3	F7V	7.170±0.013	6.991±0.021	6.868±0.025	6.788±0.038	6.821±0.019
BD+01 2447	04 52 24.41	-16 49 21.9	M3V	6.176±0.021	5.605±0.033	5.311±0.023	6.765±6.602	6.532±0.038
CD-56 1032 A	04 53 30.54	-55 51 31.7	M3V	7.197±0.027	6.623±0.055	6.338±0.021	5.837±5.289	5.200±0.042
HIP 23179	04 59 15.43	37 53 25.1	A1V	4.903±0.470	4.980±0.015	4.922±0.021	4.956±0.110	4.653±0.073
HIP 23362	04 59 15.43	37 53 25.1	A1V	4.903±0.470	4.980±0.015	4.922±0.021	4.956±0.110	4.653±0.073
HIP 23200	04 59 34.83	01 47 00.7	M0V	7.117±0.011	6.450±0.027	6.261±0.009	6.173±0.046	6.079±0.023
HIP 23309	05 00 47.12	-57 15 25.4	M0.5V	7.095±0.013	6.429±0.025	6.244±0.019	6.129±0.050	6.093±0.022
HIP 23418 ABCD	05 01 58.79	09 58 59.3	M3V	7.212±0.015	6.657±0.025	6.370±0.015	6.180±0.048	5.977±0.024
GJ 3331 A	05 06 49.91	-21 35 09.1	M1V	7.046±0.013	6.391±0.047	6.117±0.009	0.000±0.000	0.000±0.000
HIP 24947	05 20 38.05	-39 45 17.8	F6V	6.416±0.015	6.218±0.031	6.144±0.019	6.109±6.057	6.101±0.053
HD 35650 AB	05 24 30.17	-38 58 10.7	K6V	6.702±0.005	6.105±0.021	5.921±0.011	5.854±0.053	5.806±0.024
HIP 25486	05 27 04.76	-11 54 03.4	F7V	5.268±0.021	5.087±0.021	4.926±0.015	4.924±0.070	4.543±0.043
V* AB Dor B	05 28 44.47	-65 26 46.3	M3V	5.316±0.009	4.845±0.029	4.686±0.007	4.598±0.121	4.189±0.057
HIP 26309	05 36 10.29	-28 42 28.9	A2V	5.958±0.017	5.936±0.029	5.864±0.011	5.919±0.053	5.776±0.026
HIP 26369 A	05 36 55.10	-47 57 48.1	K6V	7.448±0.019	6.828±0.037	6.607±0.009	6.544±0.035	6.524±0.019
HIP 26453	05 37 39.62	-28 37 34.6	F3V	6.470±0.017	6.288±0.015	6.277±0.013	6.235±0.050	6.213±0.023
HIP 26990	05 43 35.80	-39 55 24.6	G0V	7.056±0.017	6.845±0.033	6.756±0.015	6.718±0.036	6.728±0.019
HIP 27321	05 47 17.09	-51 03 59.4	A5V	3.669±0.236	3.544±0.200	3.526±0.222	3.663±0.100	3.003±0.040
HIP 28036	05 55 43.16	-38 06 16.3	F7V	6.494±0.011	6.308±0.047	6.206±0.017	6.175±0.048	6.153±0.022
HIP28474	06 00 41.30	-44 53 50.0	G8V	7.730±0.011	7.433±0.021	7.321±0.045	7.257±0.030	7.290±0.019
AP Col	06 04 52.15	-34 33 36.0	M5V	7.742±0.021	7.183±0.011	6.866±0.015	6.642±0.039	6.404±0.021
2MASS J06085283-2753583	06 08 52.84	-27 53 58.4	M8.5V	13.595±0.026	12.897±0.024	12.371±0.024	11.976±0.024	11.623±0.021
CD-35 2722	06 09 19.21	-35 49 31.2	M1V	7.920±0.015	7.283±0.031	7.046±0.011	6.929±0.033	6.877±0.019
SCR 0613-2742AB	06 13 13.31	-27 42 05.5	M4V	8.002±0.034	7.432±0.071	7.145±0.024	7.042±0.035	6.851±0.020
HIP 29964	06 18 28.21	-72 02 41.4	K4V	7.530±0.009	6.984±0.031	6.814±0.025	6.679±0.040	6.692±0.020
HIP 30030	06 19 08.05	-03 26 20.3	G0V	6.848±0.013	6.591±0.013	6.552±0.013	6.408±0.041	6.485±0.021
HIP 30034 A	06 19 12.91	-58 03 15.6	K1V	7.576±0.017	7.088±0.015	6.981±0.019	6.888±0.035	6.906±0.020
HD 45270 AB	06 22 30.94	-60 13 07.1	G1V	5.433±0.031	5.156±0.029	5.045±0.011	5.088±0.073	4.748±0.038
AK Pic AB	06 38 00.37	-61 32 00.2	G1.5V	5.079±0.272	4.747±0.091	4.544±0.021	4.492±0.081	4.026±0.044
CD-61 1439 A	06 39 50.02	-61 28 41.5	K7V	7.301±0.011	6.643±0.019	6.500±0.013	6.424±0.045	6.488±0.021
HIP 32104	06 42 24.31	17 38 43.0	A2V	5.026±0.033	5.070±0.015	5.011±0.013	5.022±0.064	4.718±0.040
HIP 32235	06 43 46.25	-71 58 35.6	G6V	7.693±0.023	7.380±0.029	7.278±0.039	7.276±0.030	7.319±0.020
HIP 32435	06 46 13.54	-83 59 29.5	F5V	6.553±0.023	6.396±0.027	6.299±0.015	6.312±0.046	6.273±0.021

Table 2 continued

Table 2 (continued)

Name	RA	DEC	SpT	J	H	K	W1	W2
	(J2000.0)	(J2000.0)						
HIP 33737	07 00 30.46	-79 41 45.9	K2V	8.265±0.015	7.831±0.055	7.652±0.021	7.620±0.024	7.656±0.020
V* V429 Gem	07 23 43.59	+20 24 58.7	K5V	7.643±0.013	7.032±0.009	6.879±0.011	6.777±0.038	6.782±0.020
HIP 36349 C	07 25 51.18	-30 15 52.8	M5.0V	6.615±0.017	5.970±0.033	5.716±0.013	5.592±0.059	5.374±0.029
HIP 36948	07 35 47.47	-32 12 14.1	G8Vk	6.905±0.019	6.578±0.043	6.458±0.019	6.433±0.042	6.440±0.021
HIP 47135	09 36 17.83	-78 20 41.7	G1V	7.475±0.019	7.241±0.027	7.160±0.007	7.119±0.032	7.155±0.020
TWA21	10 13 14.78	-52 30 54.0	K3V	7.870±0.015	7.353±0.031	7.194±0.015	7.133±0.029	7.170±0.021
HIP 50191	10 14 44.16	-42 07 18.9	A2V	3.858±0.264	3.713±0.244	3.775±0.282	3.718±0.100	3.018±0.076
TWA 22 B	10 17 26.89	-53 54 26.5	M6V	8.554±0.013	8.085±0.043	7.689±0.015	7.495±0.023	7.272±0.020
TWA 1	11 01 51.91	-34 42 17.0	K6V	8.217±0.017	7.558±0.039	7.297±0.019	7.101±0.033	6.947±0.020
TWA 2 A	11 09 13.81	-30 01 39.8	M2V	7.629±0.025	6.927±0.037	6.710±0.021	6.637±0.038	6.537±0.021
TWA 12	11 21 05.50	-38 45 16.3	M1V	8.999±0.029	8.334±0.029	8.053±0.025	8.046±0.023	7.950±0.020
TWA 13 A	11 21 17.24	-34 46 45.5	M1V	8.431±0.039	7.727±0.065	7.491±0.035	7.635±0.052	7.545±0.030
TWA 4 AC	11 22 05.29	-24 46 39.8	K4V	6.397±0.011	5.759±0.023	5.587±0.015	5.487±0.062	5.325±0.032
TWA 5 A	11 31 55.26	-34 36 27.2	M2V	7.669±0.019	6.987±0.031	6.745±0.017	6.654±0.038	6.507±0.020
TWA30	11 32 18.31	-30 19 51.8	M5V	9.641±0.024	9.030±0.023	8.765±0.021	8.796±0.022	8.436±0.021
TWA 8 B	11 32 41.16	-26 52 09.0	M5.5V	9.837±0.021	9.276±0.020	9.012±0.023	8.862±0.061	8.608±0.053
TWA 26	11 39 51.14	-31 59 21.5	M9V	12.686±0.023	11.996±0.020	11.503±0.021	11.155±0.023	10.793±0.020
TWA 9 A	11 48 23.73	-37 28 48.5	M1V	9.981±0.025	9.381±0.021	9.151±0.022	9.008±8.879	8.810±0.050
HIP 57632	11 49 03.66	14 34 19.7	A3V	1.854±0.274	1.925±0.194	1.883±0.192	2.794±0.083	1.490±0.083
TWA 23	12 07 27.38	-32 47 00.3	M1V	8.618±0.023	8.025±0.041	7.751±0.027	7.642±0.026	7.506±0.022
TWA 27 AB	12 07 33.47	-39 32 54.0	M8V	12.995±0.023	12.388±0.026	11.945±0.024	11.556±0.023	11.009±0.020
TWA 25	12 15 30.72	-39 48 42.6	M0V	8.166±0.029	7.504±0.039	7.306±0.013	7.264±0.029	7.208±0.020
TWA 11 C	12 35 48.94	-39 50 24.6	M4V	9.790±0.023	9.223±0.020	8.943±0.023	8.796±0.022	8.593±0.020
GJ 490 A	12 57 40.30	35 13 30.6	M0.5V	7.401±0.019	6.734±0.017	6.552±0.016	6.371±6.391	6.301±0.042
PX Vir	13 03 49.65	-05 09 42.5	G5V	6.053±0.013	5.674±0.035	5.509±0.017	5.396±0.073	5.316±0.027
GJ 1167 AB	13 09 34.95	28 59 06.6	M4.8	9.476±0.027	8.912±0.031	8.612±0.019	8.393±0.024	8.204±0.020
HIP 68994	14 07 29.29	-61 33 44.1	F4V	6.975±0.009	6.787±0.033	6.715±0.015	6.673±0.034	6.685±0.021
HIP 74405	15 12 23.43	-75 15 15.6	G9V	7.844±0.019	7.457±0.027	7.377±0.015	7.384±0.027	7.428±0.018
HIP 76629 A	15 38 57.55	-57 42 27.3	K0V	6.382±0.017	5.994±0.027	5.852±0.027	5.912±0.041	5.727±0.025
HD 139751 A	15 40 28.39	-18 41 46.2	K3V	7.729±0.027	7.135±0.021	6.948±0.015	6.934±0.036	6.889±0.021
HIP 79797	16 17 05.40	-67 56 28.5	A4V	5.768±0.029	5.684±0.043	5.657±0.013	5.619±0.058	5.483±0.022
HIP 79881	16 18 17.90	-28 36 50.5	A0V	4.855±0.033	4.939±0.075	4.739±0.011	4.765±0.069	4.502±0.038
HIP 81084	16 33 41.61	-09 33 11.9	M0.5V	8.377±0.013	7.779±0.049	7.547±0.021	7.449±0.024	7.443±0.021
HD 152555	16 54 08.14	-04 20 24.7	G0V	6.700±0.017	6.480±0.033	6.363±0.013	6.262±0.043	6.311±0.023
HIP 83494	17 03 53.58	34 47 24.8	A5V	5.654±0.013	5.675±0.035	5.601±0.009	5.633±5.459	5.607±0.057
HIP 84586	17 17 25.51	-66 57 03.7	G5IV	5.288±0.027	4.907±0.033	4.702±0.005	4.589±0.085	4.234±0.045
HIP 84642 A	17 18 14.65	-60 27 27.5	G8V	8.008±0.007	7.671±0.015	7.527±0.017	7.449±7.464	7.445±0.026
HD 160934 AB	17 38 39.63	61 14 16.0	M0V	7.618±0.017	6.998±0.007	6.812±0.013	6.727±0.038	6.700±0.020
HIP 88399 A	18 03 03.41	-51 38 56.4	F5V	6.159±0.009	6.022±0.027	5.913±0.013	5.882±0.057	5.841±0.021
HIP 88726 A	18 06 49.90	-43 25 30.8	A5V	4.680±0.246	4.488±0.041	4.386±0.009	4.410±0.081	3.828±0.049
HIP 92024 A	18 45 26.90	-64 52 16.5	A7V	4.382±0.260	4.251±0.212	4.298±0.027	4.269±0.094	3.775±0.059
HIP 92680	18 53 05.87	-50 10 49.9	G9IV	6.856±0.013	6.486±0.047	6.366±0.019	6.257±0.049	6.285±0.022
HIP 94235 AB	19 10 57.85	-60 16 19.9	G1V	7.201±0.015	6.966±0.017	6.881±0.023	6.822±0.035	6.835±0.021
HIP 95261	19 22 51.21	-54 25 26.2	A0V	5.096±0.033	5.148±0.081	5.008±0.029	4.969±0.069	4.651±0.035
HIP 95347	19 23 53.17	-40 36 57.4	B8V	4.173±0.248	4.195±0.208	4.195±0.033	4.223±0.094	3.850±0.051
HIP 98495	20 00 35.58	-72 54 38.0	A0V	3.798±0.248	3.762±0.234	3.800±0.258	4.011±0.118	3.443±0.071
HIP 99273	20 09 05.21	-26 13 26.5	F5V	6.321±0.009	6.091±0.023	6.076±0.021	6.044±0.051	5.992±0.025
2MASSJ20100002-2801410	20 10 00.03	-28 01 41.0	M3V	8.651±0.023	8.014±0.047	7.733±0.027	7.609±0.031	7.446±0.021
HIP 99770	20 14 32.03	36 48 22.5	A2V	4.886±0.306	4.688±0.242	4.422±0.009	4.484±0.092	3.957±0.047
HIP 100751	20 25 38.86	-56 44 06.3	B2IV	2.304±0.312	2.458±0.218	2.479±0.282	3.163±0.127	2.541±0.026
HIP 102141B	20 41 51.16	-32 26 06.8	M4V	5.807±0.019	5.201±0.043	4.944±0.039	4.680±0.089	4.067±0.043

Table 2 continued

Table 2 (continued)

Name	RA	DEC	SpT	J	H	K	W1	W2
	(J2000.0)	(J2000.0)						
2MASSJ20434114-2433534	20 43 41.14	-24 33 53.1	M4.1V+M3.7V	8.481±0.027	7.851±0.034	7.641±0.027	7.374±0.028	7.336±0.019
HIP 102409	20 45 09.53	-31 20 27.2	M1V	5.436±0.003	4.831±0.005	4.529±0.013	4.499±0.086	3.999±0.048
HIP 103311 AB	20 55 47.67	-17 06 51.0	F8V	6.207±0.009	5.945±0.035	5.811±0.013	5.718±0.056	5.663±0.024
HIP 105388	21 20 49.96	-53 02 03.1	G7V	7.386±0.013	7.026±0.035	6.908±0.017	6.815±0.035	6.872±0.020
HIP 105404 AB	21 20 59.80	-52 28 40.1	G9V	7.184±0.026	6.699±0.031	6.574±0.024	6.536±6.520	6.507±0.041
HIP 107345	21 44 30.12	-60 58 38.9	M1V	8.751±0.019	8.087±0.017	7.874±0.021	7.781±0.024	7.755±0.020
HIP 107947	21 52 09.72	-62 03 08.5	F6V	6.358±0.021	6.149±0.027	6.027±0.015	6.013±0.052	5.954±0.024
TYC 5899-0026-1	21 52 10.42	05 37 35.9	M3V	7.740±0.021	7.146±0.031	6.891±0.027	7.209±7.068	7.008±0.030
HIP 108195 A	21 55 11.39	-61 53 11.8	F3V	5.242±0.033	5.227±0.075	4.909±0.009	4.903±0.074	4.579±0.041
HIP 108422 AB	21 55 11.39	-61 53 11.8	F3V	5.242±0.033	5.227±0.075	4.909±0.009	4.903±0.074	4.579±0.041
HIP 109268	22 08 13.98	-46 57 39.5	B6V	2.021±0.350	2.027±0.228	2.016±0.244	3.659±-9.000	9.115±-9.000
1RXS J221419.3+253411 AB	22 14 17.66	25 34 06.6	M4.3V	10.177±0.016	9.624±0.018	9.339±0.016	9.197±9.007	8.893±0.024
HIP 110526 A	22 23 29.11	32 27 34.1	M3V	6.898±0.011	6.279±0.007	6.054±0.009	5.891±0.052	5.684±0.025
HIP 112312 A	22 44 57.97	-33 15 01.7	M4IV	7.786±0.009	7.154±0.027	6.932±0.025	6.789±0.037	6.595±0.020
HD 217343	23 00 19.82	-26 09 13.5	G5V	7.048±0.007	6.448±0.019	6.267±0.007	6.111±0.052	6.144±0.022
HIP 114066	23 06 04.84	63 55 34.4	M1V	7.815±0.015	7.167±0.037	6.977±0.017	6.926±0.033	6.908±0.020
HIP 114189	23 07 28.69	21 08 03.3	A5V	5.383±0.021	5.280±0.011	5.240±0.011	5.192±0.068	4.997±0.034
HD 218860 A	23 11 52.05	-45 08 10.6	G5V	7.467±0.019	7.109±0.023	7.032±0.017	6.968±0.031	7.022±0.020
HIP 115162	23 19 39.56	42 15 09.8	G4V	7.605±0.009	7.275±0.007	7.224±0.021	7.160±0.032	7.202±0.021
HIP 115738	23 26 55.96	01 15 20.2	A0V	5.317±0.270	4.984±0.005	4.902±0.011	4.949±0.079	4.670±0.038
G 190-27 A	23 29 22.58	41 27 52.2	M4.2V	8.017±0.021	7.406±0.025	7.166±0.015	6.976±6.806	6.715±0.031
HIP 116748 A	23 39 39.48	-69 11 44.7	G5V	7.122±0.017	6.759±0.017	6.676±0.031	6.844±0.066	6.748±0.030
κ And	23 40 24.49	44 20 02.1	B9V	4.624±0.264	4.595±0.218	4.571±0.354	4.462±3.885	4.410±0.080
HD 222575	23 41 54.29	-35 58 39.8	G8V	8.097±0.017	7.771±0.041	7.624±0.015	7.553±0.025	7.593±0.021
HIP 117452 AB	23 48 55.55	-28 07 49.0	A0V	4.801±0.262	4.643±0.075	4.532±0.015	4.530±0.078	4.003±0.053
HIP 118121	23 57 35.08	-64 17 53.6	A1V	4.910±0.033	4.949±0.027	4.824±0.015	4.804±0.080	4.517±0.042

Table 3. Properties of the sample of bona fide members

Name	$\mu_{\alpha} \cos \delta$	μ_{δ}	Radial Velocities	Distance	Association
	(mas/yr)	(mas/yr)	(km/s)	(pc)	
HIP 490	97.53±0.38	-76.27±0.44	1.5±1.2	39.38±0.91	Tucana-Horologium
HIP 560	97.81±0.42	-47.12±0.21	6.5±3.5	39.38±0.58	β -Pictoris
HIP 1113	83.53±0.78	-47.89±0.75	9.3±0.2	44.40±1.61	Tucana-Horologium
HIP 1134	102.79±0.78	-66.36±0.36	-2.2±1.2	47.14±1.42	Columba
HIP 1481	89.37±0.48	-59.46±0.50	6.4±0.4	41.54±0.89	Tucana-Horologium
HIP 1910 AB	90.91±2.37	-47.25±3.04	6.6±0.6	52.96±7.63	Tucana-Horologium
HIP 1993	87.76±2.14	-57.48±2.37	6.4±0.1	45.80±5.07	Tucana-Horologium
GJ 2006A	117.40±2.80	-29.30±8.10	8.7±0.2	32.20±1.05	β -Pictoris
HIP 2484 B	83.64±0.19	-54.82±0.18	14.0±5.0	41.40±0.34	Tucana-Horologium
HIP 2578	86.66±0.18	-50.33±0.17	7.7±0.8	45.55±0.39	Tucana-Horologium
HIP 2729	88.28±0.92	-53.16±0.91	-1.0±2.0	43.93±1.91	Tucana-Horologium
HIP 3556	95.74±1.92	-58.95±1.87	-1.6±10.0	40.35±4.31	Tucana-Horologium
HD 4277 A	96.81±0.65	-74.17±0.53	-14.8±1.7	52.52±2.45	AB-Doradus
HIP 4448 A	95.93±1.57	10.23±1.35	1.6±0.5	40.63±2.70	Argus
G 132-51 B	132.00±5.00	-164.00±5.00	-10.6±0.3	29.94±1.97	AB-Doradus
HD 6569 AB	99.29±1.23	-94.93±0.74	6.7±1.2	47.34±2.75	AB-Doradus
2MASS J01112542+1526214	180.00±2.00	-120.00±5.00	4.0±1.0	21.80±0.79	β -Pictoris
CD-12 243	110.59±0.92	-138.43±0.69	8.2±0.4	34.39±1.19	AB-Doradus
2MUCD 13056	77.40±2.40	-25.40±9.00	10.9±3.7	42.10±5.00	Tucana-Horologium
HIP 6485	92.45±0.92	-38.00±0.72	9.2±0.4	49.52±2.03	Tucana-Horologium
G 269-153 A	178.00±20.00	-110.00±20.00	19.4±2.7	25.12±1.01	AB-Doradus
HIP 6856	106.09±1.02	-42.81±1.24	8.0±0.2	36.02±1.29	Tucana-Horologium
2MASS J01351393-0712517	96.00±10.00	-50.00±10.00	11.7±5.3	37.87±2.29	β -Pictoris
G271-110	168.00±5.00	-105.00±5.00	12.2±0.4	41.66±0.69	β -Pictoris
HIP 9141 AB	105.08±0.72	-50.60±0.54	7.5±1.0	40.89±1.12	Tucana-Horologium
HIP 9685	75.74±0.45	-25.05±0.48	3.4±3.7	47.75±1.04	Tucana-Horologium
HIP 9892 AB	86.06±0.58	-22.60±0.65	10.0±0.5	50.94±1.66	Tucana-Horologium
HIP 9902	91.11±0.47	-18.29±0.47	11.1±0.7	44.16±0.87	Tucana-Horologium
HD 13482 A	125.44±1.45	-161.47±0.98	-0.3±0.2	36.63±1.59	AB-Doradus
HIP 10602 A	91.03±0.12	-22.23±0.12	10.2±2.0	47.12±0.26	Tucana-Horologium
HIP 10679	80.15±4.38	-78.40±4.91	6.5±0.7	27.33±4.35	β -Pictoris
HIP 11152	92.43±3.05	-113.69±2.36	10.4±2.0	28.68±2.33	β -Pictoris
HIP 11360	86.09±1.08	-50.13±0.72	8.8±3.0	44.78±2.10	β -Pictoris
HIP 11437 A	79.78±2.56	-70.02±1.73	7.0±1.1	39.95±3.59	β -Pictoris
IRXSJ022735.8+471021	119.00±5.00	-183.00±5.00	-6.0±0.7	36.50±3.07	AB-Doradus
HIP12394	87.30±0.09	0.09±0.10	13.6±0.9	46.55±0.19	Tucana-Horologium
HIP12413	88.20±2.02	-17.82±1.98	18.0±4.2	35.68±2.78	Columba
HIP 12545 AB	79.47±3.05	-53.89±1.74	10.0±1.0	42.03±2.65	β -Pictoris
AF Hor	92.20±1.10	-4.20±1.50	12.6±0.7	44.01±0.77	Tucana-Horologium
HIP 12635	75.73±2.49	-111.45±2.73	-4.1±0.3	50.42±6.66	AB-Doradus
HIP12925	75.27±1.45	-44.78±0.83	4.3±1.1	54.31±3.06	Tucana-Horologium
HD 17332 A	117.91±0.89	-161.81±0.71	3.7±0.3	33.55±0.92	AB-Doradus
HIP 13209	66.81±0.24	-116.52±0.15	4.0±4.1	50.78±0.49	AB-Doradus
HIP 14551	66.26±0.50	-19.09±0.49	13.8±0.8	54.64±1.49	Tucana-Horologium
IS Eri	91.01±1.30	-112.21±1.30	14.4±0.7	37.41±1.56	AB-Doradus
HIP 14807	54.86±3.99	-134.25±3.87	4.1±0.3	40.16±2.06	AB-Doradus
HIP 14913 A	81.63±0.55	-4.57±0.98	13.5±2.1	42.49±1.11	Tucana-Horologium
HIP 15247	78.63±0.67	-43.82±0.71	9.0±0.7	49.23±1.43	Tucana-Horologium

Table 3 continued

Table 3 (continued)

Name	$\mu_{\alpha} \cos \delta$	μ_{δ}	Radial Velocities	Distance	Association
	(mas/yr)	(mas/yr)	(km/s)	(pc)	
HIP 15353	56.94±0.30	12.68±0.40	26.0±0.5	54.94±0.90	AB-Doradus
CD-35 1167	89.20±2.80	-20.30±2.80	13.2±0.3	45.28±0.73	Tucana-Horologium
CD-44 1173	90.90±1.90	-5.00±1.90	15.1±0.5	45.24±0.61	Tucana-Horologium
V577 Per	68.46±0.96	-176.81±0.76	-6.0±0.3	34.38±1.20	AB-Doradus
2MASS J03350208+2342356	54.00±10.00	-56.00±10.00	15.5±1.7	42.37±2.33	β -Pictoris
HIP 16853 AB	89.74±0.75	0.29±0.84	14.4±0.9	43.34±1.37	Tucana-Horologium
HIP 17248	96.17±2.49	-117.69±2.26	-3.2±0.6	35.21±2.70	Columba
HIP 17695	185.53±3.77	-273.48±3.95	16.0±1.7	16.12±0.74	AB-Doradus
HIP 17764	63.46±0.39	24.86±0.49	15.5±1.3	54.05±1.16	Tucana-Horologium
HIP 17782 AB	61.87±1.98	-70.99±1.67	-2.2±0.6	51.67±4.32	Tucana-Horologium
HIP 17797	74.44±0.71	-9.09±0.87	15.6±0.4	50.73±2.21	Tucana-Horologium
HIP 18714 AB	69.46±0.81	-7.00±0.85	16.3±0.7	48.49±1.66	Tucana-Horologium
HD 25457	149.04±0.42	-253.03±0.43	17.6±0.2	18.83±0.11	AB-Doradus
HD 25953	37.08±1.43	-94.59±1.34	15.9±1.3	55.18±2.80	AB-Doradus
IRXS J041417.0-090650	96.00±10.00	-138.00±10.00	23.4±0.3	23.80±1.41	AB-Doradus
HIP 21547	44.22±0.34	-64.39±0.27	21.0±4.5	29.42±0.29	β -Pictoris
HIP 21632	56.03±0.51	-11.08±0.72	18.8±5.0	56.17±2.80	Tucana-Horologium
HIP 21965	50.25±0.69	-11.84±0.78	19.3±2.9	63.57±3.96	Tucana-Horologium
HIP 22295	46.66±0.49	41.30±0.56	11.5±2.0	61.01±1.89	Tucana-Horologium
BD+01 2447	118.90±4.50	-211.90±4.70	26.7±1.5	16.29±0.39	AB-Doradus
CD-56 1032 A	132.90±4.20	73.90±3.80	40.0±19.9	11.17±0.44	AB-Doradus
HIP 23179	46.35±0.63	-97.80±0.41	7.7±2.5	52.27±2.15	Columba
HIP 23362	46.35±0.63	-97.80±0.41	7.7±2.5	52.27±2.15	Columba
HIP 23200	34.60±2.34	-94.27±1.44	16.6±1.0	25.87±1.70	β -Pictoris
HIP 23309	36.34±1.42	70.22±1.27	19.4±0.3	26.78±0.81	β -Pictoris
HIP 23418 ABCD	12.09±9.92	-74.41±5.71	18.4±3.0	24.88±1.28	β -Pictoris
GJ 3331 A	34.20±1.20	-33.80±2.10	21.2±0.9	19.19±0.51	β -Pictoris
HIP 24947	38.36±0.29	13.06±0.50	23.9±2.2	48.30±0.95	Tucana-Horologium
HD 35650 AB	44.25±0.67	-59.51±1.13	31.9±0.3	18.00±0.29	AB-Doradus
HIP 25486	17.55±0.36	-50.23±0.36	21.1±1.6	27.04±0.35	β -Pictoris
V* AB Dor B	33.16±0.39	150.83±0.73	31.0±2.5	14.94±0.11	AB-Doradus
HIP 26309	25.80±0.31	-3.04±0.46	22.4±1.2	52.79±1.19	Columba
HIP 26369 A	24.05±2.62	13.08±1.82	32.2±0.2	25.63±4.82	AB-Doradus
HIP 26453	24.29±0.44	-4.06±0.74	23.5±0.4	56.78±1.99	Columba
HIP 26990	25.82±0.32	15.08±0.52	22.8±0.6	55.37±1.37	Columba
HIP 27321	4.65±0.11	83.10±0.15	20.0±0.7	19.44±0.04	β -Pictoris
HIP 28036	20.49±0.44	9.34±0.44	24.1±0.5	54.37±1.30	Columba
HIP28474	18.02±0.59	23.85±0.75	23.8±0.4	52.54±1.65	Columba
AP Col	27.33±0.35	340.92±0.35	22.4±0.3	8.38±0.06	Argus
2MASS J06085283-2753583	8.90±3.50	10.70±3.50	24.0±1.0	31.25±3.51	β -Pictoris
CD-35 2722	-6.30±2.80	-56.60±2.80	31.4±0.4	21.27±1.35	AB-Doradus
SCR 0613-2742AB 2MASS J06	-14.90±1.00	-2.10±1.00	22.5±0.2	29.40±0.90	β -Pictoris
HIP 29964	-8.32±0.86	72.02±1.06	16.2±1.0	38.55±1.33	β -Pictoris
HIP 30030	10.90±0.75	-42.62±0.61	19.1±2.4	49.23±1.96	Columba
HIP 30034 A	14.36±0.74	44.66±0.84	22.6±0.3	46.06±1.46	Carina
HD 45270 AB	-11.29±0.35	64.24±0.30	31.2±0.2	23.78±0.15	AB-Doradus
AK Pic AB	-47.84±1.04	72.73±0.87	32.3±1.0	21.29±0.36	AB-Doradus
CD-61 1439 A	-27.92±1.00	75.34±1.13	30.5±0.7	22.35±0.45	AB-Doradus
HIP 32104	7.87±0.66	-84.32±0.48	15.0±4.2	43.63±1.27	Columba
HIP 32235	6.17±0.80	61.15±0.87	20.7±0.1	58.24±2.44	Carina
HIP 32435	19.66±0.43	61.60±0.47	12.5±0.7	56.02±1.12	Tucana-Horologium

Table 3 continued

Table 3 (continued)

Name	$\mu_{\alpha} \cos \delta$	μ_{δ}	Radial Velocities	Distance	Association
	(mas/yr)	(mas/yr)	(km/s)	(pc)	
HIP 33737	1.56±0.94	59.94±1.00	17.6±0.1	58.82±3.07	Carina
V* V429 Gem	-65.80±1.60	-228.10±1.70	8.2±0.8	25.77±1.32	AB-Doradus
HIP 36349 C	-130.00±10.00	-180.00±10.00	28.1±1.0	14.90±0.71	AB-Doradus
HIP 36948	-55.71±0.59	74.58±0.62	22.5±0.1	35.34±1.06	Argus
HIP 47135	-74.85±0.59	50.62±0.59	5.2±0.1	67.98±2.77	Argus
TWA21	-60.70±2.50	12.80±1.60	17.5±0.8	54.79±1.47	TW Hydrae
HIP 50191	-150.09±0.10	49.44±0.11	7.4±2.7	31.07±0.14	Argus
TWA 22 B	-175.80±0.80	-21.30±0.80	14.8±2.1	17.54±0.21	β -Pictoris
TWA 1	-66.19±1.85	-13.90±1.47	13.4±0.8	53.70±6.17	TW Hydrae
TWA 2 A	-95.50±2.90	-23.50±2.80	10.5±0.5	46.55±2.81	TW Hydrae
TWA 12	-68.30±2.70	-12.10±1.50	10.9±1.0	64.14±2.88	TW Hydrae
TWA 13 A	-66.40±2.40	-12.50±1.80	11.6±0.6	55.61±2.22	TW Hydrae
TWA 4 AC	-85.40±1.73	-33.10±2.12	9.3±1.0	44.90±4.65	TW Hydrae
TWA 5 A	-81.60±2.50	-29.40±2.40	13.3±2.0	50.07±1.75	TW Hydrae
TWA30	-89.60±1.30	-25.80±1.30	12.3±1.5	23.80±1.13	TW Hydrae
TWA 8 B	-86.00±3.00	-22.00±38.00	8.9±0.2	46.99±2.20	TW Hydrae
TWA 26	-88.00±9.00	-34.00±10.00	11.6±2.0	41.98±4.54	TW Hydrae
TWA 9 A	-52.44±2.39	-22.93±1.66	9.5±0.4	46.77±5.42	TW Hydrae
HIP 57632	-497.68±0.87	-114.67±0.44	-0.2±0.5	10.99±0.06	Argus
TWA 23	-72.70±0.90	-29.30±0.90	8.5±1.2	53.90±1.39	TW Hydrae
TWA 27 AB	-71.60±6.70	-22.10±8.50	11.2±2.0	52.63±1.10	TW Hydrae
TWA 25	-74.00±0.80	-27.70±0.80	7.5±0.1	54.11±3.63	TW Hydrae
TWA 11 C	-45.10±2.40	-20.10±2.30	9.0±1.0	69.01±2.42	TW Hydrae
GJ 490 A	-269.00±5.00	-149.00±5.00	-2.9±0.6	18.11±1.01	Tucana-Horologium
PX Vir	-191.13±0.86	-218.73±0.68	0.0±0.5	21.69±0.38	AB-Doradus
GJ 1167 AB	-332.00±5.00	-210.00±5.00	-5.2±2.6	11.49±2.39	Carina
HIP 68994	-69.88±0.79	-29.87±0.60	-5.2±1.0	64.14±3.33	Argus
HIP 74405	-73.87±0.87	-73.08±0.92	-3.5±0.1	50.30±2.68	Argus
HIP 76629 A	-53.98±1.14	-106.00±1.27	3.6±0.9	38.53±1.69	β -Pictoris
HD 139751 A	-70.13±3.32	-159.81±2.39	-8.9±0.4	40.19±4.34	AB-Doradus
HIP 79797	-45.99±0.28	-84.00±0.35	-9.0±4.3	52.21±1.14	Argus
HIP 79881	-31.19±0.26	-100.92±0.18	-13.0±0.8	41.28±0.37	β -Pictoris
HIP 81084	-70.05±2.75	-177.52±2.29	-15.0±0.4	30.67±2.32	AB-Doradus
HD 152555	-37.25±1.01	-114.05±0.73	-16.5±0.4	46.72±2.00	AB-Doradus
HIP 83494	-60.92±0.26	-5.05±0.34	-21.5±1.4	54.97±0.93	Tucana-Horologium
HIP 84586 A	-21.83±0.39	-136.91±0.42	3.3±1.6	31.44±0.49	β -Pictoris
HIP 84642 A	-54.62±1.09	-91.04±0.84	1.3±0.7	58.92±4.65	Tucana-Horologium
HD 160934 AB	-23.30±2.03	47.71±2.20	-26.7±0.1	33.12±2.19	AB-Doradus
HIP 88399 A	4.02±0.60	-86.46±0.36	-0.2±0.5	48.14±1.29	β -Pictoris
HIP 88726 A	10.73±1.05	-106.59±0.51	-7.8±0.4	41.84±1.15	β -Pictoris
HIP 92024 A	32.40±0.17	-149.48±0.17	2.0±4.2	28.54±0.15	β -Pictoris
HIP 92680	17.64±1.13	-83.63±0.76	-4.2±0.2	51.49±2.59	β -Pictoris
HIP 94235 AB	12.51±0.79	-100.15±0.68	8.1±0.6	61.34±2.89	AB-Doradus
HIP 95261	25.57±0.21	-82.71±0.14	13.0±4.2	48.21±0.48	β -Pictoris
HIP 95347	30.49±0.35	-119.21±0.18	-0.7±2.5	55.74±0.68	AB-Doradus
HIP 98495	81.78±0.11	-132.16±0.14	-6.7±0.7	32.21±0.17	Argus
HIP 99273	39.17±0.50	-68.25±0.36	-5.8±2.0	52.21±1.22	β -Pictoris
2MASSJ20100002-2801410	40.70±3.00	-62.00±1.70	-5.8±0.6	47.96±3.05	β -Pictoris
HIP 99770	69.81±0.19	69.14±0.20	-17.3±2.8	42.69±0.40	Argus
HIP 100751	6.90±0.44	-86.02±0.32	2.0±0.9	54.82±1.56	Tucana-Horologium
HIP 102141B	270.45±4.63	-365.60±3.50	-4.0±3.7	10.69±0.41	β -Pictoris

Table 3 continued

Table 3 (continued)

Name	$\mu_{\alpha \cos \delta}$	μ_{δ}	Radial Velocities	Distance	Association
	(mas/yr)	(mas/yr)	(km/s)	(pc)	
2MASSJ20434114-2433534	62.00±10.00	-60.00±10.00	-6.1±0.3	35.58±4.93	β -Pictoris
HIP 102409	279.96±1.26	-360.61±0.73	-4.5±1.3	9.90±0.10	β -Pictoris
HIP 103311 AB	58.81±0.83	-62.83±0.73	-9.0±3.0	45.66±1.60	β -Pictoris
HIP 105388	28.77±1.01	-94.19±0.55	-0.9±0.7	42.97±1.80	Tucana-Horologium
HIP 105404 AB	25.45±1.69	-103.88±0.73	6.0±2.0	44.44±2.76	Tucana-Horologium
HIP 107345	39.98±2.35	-91.66±1.56	2.3±0.5	43.64±4.91	Tucana-Horologium
HIP 107947	44.05±0.41	-92.02±0.45	1.5±0.6	45.33±1.35	Tucana-Horologium
TYC 5899-0026-1	105.70±1.50	-147.40±1.40	-15.1±1.5	30.49±5.25	AB-Doradus
HIP 108195 A	44.50±0.23	-91.07±0.27	1.0±3.0	46.46±0.88	Tucana-Horologium
HIP 108422 AB	44.50±0.23	-91.07±0.27	1.0±3.0	46.46±0.88	Tucana-Horologium
HIP 109268	126.69±0.14	-147.47±0.14	10.9±1.7	30.96±0.20	AB-Doradus
IRXS J221419.3+253411 AB	164.00±5.00	-44.00±5.00	-19.9±0.3	28.73±2.06	Columba
HIP 110526 A	255.30±3.10	-207.80±2.90	-20.6±2.1	15.51±1.56	AB-Doradus
HIP 112312 A	184.76±2.64	-119.76±2.31	1.1±1.2	23.34±1.96	β -Pictoris
HD 217343	113.54±2.13	-162.04±1.52	6.3±1.5	30.54±1.89	AB-Doradus
HIP 114066	171.46±1.59	-58.55±1.57	-23.7±0.8	24.50±0.96	AB-Doradus
HIP 114189	107.93±0.60	-49.63±0.46	-12.6±1.4	39.40±1.08	Columba
HD 218860 A	87.53±1.39	-93.36±0.79	11.2±1.3	50.76±2.83	AB-Doradus
HIP 115162	77.52±0.73	-66.90±0.96	-19.7±0.2	50.15±2.86	AB-Doradus
HIP 115738	86.68±0.31	-94.29±0.22	-4.4±0.6	47.05±0.64	AB-Doradus
G 190-27 A	415.00±7.50	-41.00±6.70	-14.5±0.5	14.79±0.39	Columba
HIP 116748 A	79.00±1.10	-67.10±1.20	6.1±0.1	46.29±2.78	Tucana-Horologium
Kappa And	80.73±0.14	-18.70±0.15	-12.7±0.6	51.62±0.50	Columba
HD 222575	69.49±1.18	-67.53±0.95	11.1±1.7	63.69±4.58	AB-Doradus
HIP 117452 AB	100.80±0.25	-105.34±0.23	8.7±2.0	42.14±0.39	AB-Doradus
HIP 118121	79.12±0.47	-60.80±0.46	0.5±0.8	47.43±1.10	Tucana-Horologium

Table 4. *J*-band observations for all the target in the sample

Name	Filter	Instrument	Obs. Date	Nexp	Exposition Time	FWHM	Catalog	Conditions
					(s)	($''$)		
HIP490	J_G0802	F2	2014-07-25	9	612	0.72	median	photometric
HIP560	J_G0802	F2	2014-07-25	9	612	1.31	2MASS	photometric
HIP1113	J_G0802	F2	2016-10-10	14	630	0.67	2MASS	photometric
HIP1134	J	WIRCam	2016-08-18	16	960	0.70	2MASS	patchy clouds
HIP1481	J_G0802	F2	2014-07-25	9	612	1.01	VISTA	patchy clouds
HIP1910	J_G0802	F2	2016-09-16	14	630	0.77	2MASS	photometric
HIP1993	J_G0802	F2	2015-09-02	14	630	0.89	2MASS	patchy clouds
GJ2006A	J_G0802	F2	2014-07-25	9	612	0.69	2MASS	photometric
HIP2484	J_G0802	F2	2014-08-01	19	722	1.02	2MASS	patchy clouds
HIP2578	J_G0802	F2	2015-11-22	14	630	0.80	2MASS	patchy clouds
HIP2729	J_G0802	F2	2015-09-02	14	630	0.89	2MASS	photometric
HIP3556	J_G0802	F2	2014-07-25	9	612	0.78	2MASS	photometric
HIP3589	J	WIRCam	2015-11-17	16	960	0.21	2MASS	patchy clouds
HIP4448	J_G0802	F2	2014-07-26	10	680	0.95	2MASS	patchy clouds
G132-51B	J	WIRCam	2015-05-28	32	1885	0.70	2MASS	patchy clouds
HD6569	J_G0802	F2	2014-07-26	9	612	0.78	median	patchy clouds
2MASSJ0112542+1526214	J	WIRCam	2015-02-16	15	884	0.70	2MASS	photometric
HIP6276	J_G0802	F2	2014-07-26	9	612	0.93	median	patchy clouds
2MUCD13056	J_G0802	F2	2014-08-01	9	612	0.90	2MASS	photometric
HIP6485	J_G0802	F2	2015-11-27	5	225	1.36	2MASS	patchy clouds
G269-153	J	WIRCam	2015-02-12	16	942	0.70	2MASS	patchy clouds
HIP6856	J_G0802	F2	2014-08-01	9	612	1.06	VISTA	patchy clouds
2MASSJ01351393-0712517	J_G0802	F2	2014-07-25	9	612	1.04	SIMON	photometric
G271-110	J	WIRCam	2016-08-18	16	960	0.20	2MASS	photometric
HIP9141	J_G0802	F2	2014-07-26	9	612	0.73	median	patchy clouds
HIP9685	J_G0802	F2	2014-08-01	9	612	0.92	VISTA	photometric
HIP9892	J_G0802	F2	2016-01-02	14	630	0.84	VISTA	patchy clouds
HIP9902	J_G0802	F2	2016-09-17	14	630	0.83	median	photometric
HIP10272	J_G0802	F2	2014-08-03	9	612	0.97	median	patchy clouds
HIP10602	J_G0802	F2	2015-11-22	15	675	0.81	VISTA	patchy clouds
HIP10679	J_G0802	WIRCam	2015-11-22	15	45	0.24	VISTA	patchy clouds
HIP11152	J	WIRCam	2015-11-17	15	960	0.70	2MASS	patchy clouds
HIP11360	J_G0802	F2	2014-08-01	11	748	1.12	median	patchy clouds
HIP11437	J	WIRCam	2015-11-17	17	960	0.70	2MASS	patchy clouds
IRXSJ022735.8+471021	J	WIRCam	2016-08-18	19	1140	0.41	2MASS	patchy clouds
HIP12394	J_G0802	F2	2015-11-22	14	630	0.72	2MASS	patchy clouds
HIP12413	J_G0802	F2	2014-07-20	18	1224	0.69	SIMON	patchy clouds
HIP12545	J_G0802	F2	2014-09-22	11	748	0.29	median	patchy clouds
AFHor	J_G0802	F2	2016-08-16	14	630	0.84	VISTA	photometric
HIP12635	J	WIRCam	2015-11-17	16	960	0.70	2MASS	patchy clouds
HIP12925	J	WIRCam	2015-11-17	16	960	0.70	2MASS	patchy clouds
HIP13027	J_G0802	F2	2014-07-25	9	612	0.89	2MASS	photometric
HIP13209	J	WIRCam	2015-11-15	16	960	0.70	2MASS	patchy clouds
HIP14551	J	WIRCam	2016-08-18	15	900	0.33	2MASS	patchy clouds
IS-Eri	J_G0802	F2	2014-07-25	9	612	0.70	2MASS	photometric
HIP14807	J_G0802	F2	2014-08-03	9	612	0.99	median	photometric
HIP14913	J_G0802	F2	2016-11-05	14	630	0.56	median	photometric
HIP15247	J	WIRCam	2015-11-17	17	960	0.70	2MASS	patchy clouds

Table 4 continued

Table 4 (continued)

Name	Filter	Instrument	Obs. Date	Nexp	Exposition Time	FWHM	Catalog	Conditions
					(s)	(")		
HIP15353	J_G0802	F2	2015-09-02	14	630	0.96	2MASS	photometric
CD-351167	J_G0802	F2	2015-11-22	14	630	0.88	2MASS	patchy clouds
CD-441173	J_G0802	F2	2015-09-02	13	585	1.12	median	photometric
V577-Per	J	WIRCam	2015-11-17	16	960	0.70	2MASS	patchy clouds
2MASSJ03350208+2342356	J	WIRCam	2017-04-19	16	960	0.00	2MASS	patchy clouds
HIP16853	J_G0802	F2	2016-09-26	14	630	0.69	2MASS	patchy clouds
HIP17248	J	WIRCam	2015-11-17	16	960	0.70	2MASS	patchy clouds
HIP17695	J	WIRCam	2015-02-11	24	1355	0.70	2MASS	patchy clouds
HIP17764	J_G0802	F2	2015-09-02	14	630	0.87	2MASS	photometric
HIP17782	J	WIRCam	2015-11-17	16	900	0.70	2MASS	patchy clouds
HIP17797	J_G0802	F2	2015-09-02	14	630	0.87	median	photometric
HIP18714	J_G0802	F2	2016-02-11	14	630	0.87	2MASS	photometric
HIP18859	J	WIRCam	2015-02-11	16	942	0.70	2MASS	patchy clouds
HIP19183	J	WIRCam	2015-11-17	16	960	0.21	2MASS	patchy clouds
IRXSJ041417.0-090650	J	WIRCam	2015-02-11	16	942	0.70	VISTA	patchy clouds
HIP21547	J	WIRCam	2015-02-11	16	942	0.70	2MASS	patchy clouds
HIP21632	J	WIRCam	2016-01-18	17	963	0.70	2MASS	patchy clouds
HIP21965	J	WIRCam	2016-01-18	16	960	0.70	2MASS	patchy clouds
HIP22295	J_G0802	F2	2016-02-15	14	630	0.75	2MASS	photometric
TYC5899-0026-1	J_G0802	F2	2014-09-22	10	680	1.31	2MASS	patchy clouds
CD-561032	J_G0802	F2	2016-02-15	14	630	0.59	VISTA	photometric
HIP23179	J	WIRCam	2016-01-18	17	963	0.70	2MASS	patchy clouds
HIP23200	J	WIRCam	2015-02-11	21	1119	0.70	2MASS	patchy clouds
HIP23309	J_G0802	F2	2016-01-02	14	630	0.76	2MASS	patchy clouds
HIP23362	J	WIRCam	2016-01-18	16	960	0.70	2MASS	patchy clouds
HIP23418	J	WIRCam	2015-05-27	16	942	0.70	2MASS	patchy clouds
GJ3331	J	WIRCam	2015-05-27	16	942	0.70	2MASS	patchy clouds
HIP24947	J_G0802	F2	2016-02-16	1	45	0.65	2MASS	patchy clouds
HIP25283	J	WIRCam	2015-06-01	16	942	0.70	2MASS	patchy clouds
HIP25486	J	WIRCam	2015-05-28	16	942	0.70	2MASS	patchy clouds
HD36705B	J_G0802	F2	2015-09-13	14	630	0.84	2MASS	patchy clouds
HIP26309	J	WIRCam	2016-02-11	8	480	0.70	2MASS	patchy clouds
HIP26369	J_G0802	F2	2016-02-11	14	630	0.53	2MASS	photometric
HIP26453	J	WIRCam	2016-01-18	16	960	0.70	2MASS	patchy clouds
HIP26990	J_G0802	F2	2014-09-21	9	612	0.69	2MASS	photometric
HIP27321	J_G0802	F2	2015-09-02	13	585	0.87	SIMON	patchy clouds
HIP28036	J_G0802	F2	2015-09-02	14	630	1.00	2MASS	photometric
HIP28474	J_G0802	F2	2015-04-06	10	450	0.74	2MASS	patchy clouds
AP-Col	J	WIRCam	2015-06-01	54	2886	0.70	2MASS	patchy clouds
2MASSJ06085283-2753583	J_G0802	F2	2014-09-22	9	612	0.87	2MASS	photometric
Cd-352722	J	WIRCam	2016-02-11	13	766	0.70	2MASS	patchy clouds
2MASSJ06131330-2742054	J	WIRCam	2015-06-01	6	353	0.70	2MASS	patchy clouds
HIP29964	J_G0802	F2	2014-09-22	9	612	1.01	2MASS	photometric
HIP30030	J	WIRCam	2015-11-17	17	1020	0.70	2MASS	patchy clouds
HIP30034	J_G0802	F2	2015-03-22	14	630	0.61	2MASS	patchy clouds
HIP30314	J_G0802	F2	2016-02-14	14	630	0.57	2MASS	photometric
AK-Pic	J_G0802	F2	2016-02-15	14	630	0.64	2MASS	photometric
CD-611439	J_G0802	F2	2016-02-11	14	630	0.53	2MASS	photometric
HIP32104	J	WIRCam	2015-11-17	17	960	0.40	2MASS	patchy clouds
HIP32235	J_G0802	F2	2015-04-25	14	630	0.68	2MASS	photometric
HIP32435	J_G0802	F2	2015-04-25	14	630	0.76	2MASS	photometric

Table 4 continued

Table 4 (continued)

Name	Filter	Instrument	Obs. Date	Nexp	Exposition Time	FWHM	Catalog	Conditions
					(s)	($''$)		
HIP33737	J_G0802	F2	2015-04-25	14	630	0.73	2MASS	photometric
BD+201790	J	WIRCam	2015-06-01	36	2062	0.70	2MASS	patchy clouds
GJ2060C	J	WIRCam	2015-06-01	16	942	0.70	2MASS	patchy clouds
HIP36948	J_G0802	F2	2014-09-22	9	612	1.07	2MASS	patchy clouds
HIP47135	J_G0802	F2	2015-04-23	14	630	0.72	2MASS	photometric
TWA21	J_G0802	F2	2015-03-03	14	630	0.74	2MASS	photometric
HIP50191	J_G0802	F2	2016-01-03	16	720	0.77	VISTA	patchy clouds
TWA22	J_G0802	F2	2016-01-02	14	630	0.77	2MASS	photometric
HIP51317	J	WIRCam	2016-02-15	15	884	0.70	2MASS	photometric
TWA1	J	WIRCam	2015-06-11	19	1119	0.70	VISTA	patchy clouds
TWA2	J	WIRCam	2015-06-16	23	1355	0.70	2MASS	patchy clouds
TWA12	J_G0802	F2	2016-02-10	14	630	0.54	VISTA	photometric
TWA13	J_G0802	F2	2016-01-30	14	630	0.60	VISTA	photometric
TWA4	J	WIRCam	2016-01-18	16	960	0.70	2MASS	patchy clouds
TWA5	J_G0802	F2	2015-12-29	14	630	0.85	2MASS	photometric
TWA30A	J	WIRCam	2016-11-18	16	960	0.70	2MASS	patchy clouds
TWA8B	J	WIRCam	2016-01-18	23	1380	0.70	2MASS	patchy clouds
TWA26	J	WIRCam	2016-01-18	34	1980	0.70	2MASS	patchy clouds
TWA9	J_G0802	F2	2016-02-10	28	1260	0.62	2MASS	patchy clouds
HIP57632	J	WIRCam	2016-01-18	16	960	0.70	2MASS	patchy clouds
TWA23	J	WIRCam	2016-01-18	26	1500	0.70	2MASS	patchy clouds
TWA27	J_G0802	F2	2016-01-11	14	630	0.50	VISTA	photometric
TWA25	J_G0802	F2	2016-02-16	14	630	0.79	VISTA	photometric
TWA11C	J_G0802	F2	2016-02-15	14	630	0.79	VISTA	photometric
GJ490	J	WIRCam	2016-01-26	14	825	0.70	2MASS	patchy clouds
PX-Vir	J	WIRCam	2016-01-19	16	960	0.70	VISTA	patchy clouds
GJ1167	J	WIRCam	2015-06-01	16	942	0.70	2MASS	patchy clouds
HIP68994	J_G0802	F2	2015-04-10	14	630	0.63	2MASS	photometric
HIP74405	J_G0802	F2	2015-03-02	16	720	0.75	2MASS	photometric
HIP76629	J_G0802	F2	2015-03-03	14	630	0.67	2MASS	photometric
HIP76768	J	WIRCam	2015-06-15	16	1649	0.70	2MASS	patchy clouds
HIP79797	J_G0802	F2	2015-04-10	14	630	0.71	2MASS	photometric
HIP79881	J_G0802	F2	2014-07-25	19	646	0.55	2MASS	photometric
HIP81084	J_G0802	F2	2014-07-25	18	612	0.57	VISTA	photometric
HIP82688	J	WIRCam	2015-07-16	16	942	0.70	VISTA	patchy clouds
HIP83494	J	WIRCam	2015-07-16	16	1001	0.70	2MASS	patchy clouds
HIP84586	J_G0802	F2	2014-07-25	18	612	0.59	2MASS	photometric
HIP84642	J_G0802	F2	2015-04-10	14	630	0.63	2MASS	photometric
HIP86346	J	WIRCam	2015-07-16	16	942	0.70	2MASS	patchy clouds
HIP88399	J_G0802	F2	2014-08-02	37	1258	0.90	2MASS	patchy clouds
HR6750	J_G0802	F2	2014-07-25	18	612	0.60	VISTA	photometric
HIP92024	J_G0802	F2	2016-02-24	14	630	0.59	2MASS	photometric
HIP92680	J_G0802	F2	2014-07-25	18	612	0.57	2MASS	photometric
HIP94235	J_G0802	F2	2015-09-02	14	630	0.82	2MASS	photometric
Eta-TeLA	J_G0802	F2	2014-07-25	9	612	0.70	2MASS	patchy clouds
HIP95347	J_G0802	F2	2014-07-25	18	612	0.57	VISTA	photometric
HIP98495	J_G0802	F2	2014-08-03	26	884	0.98	2MASS	photometric
HIP99273	J_G0802	F2	2014-07-25	9	612	0.58	2MASS	photometric
2MASSJ20100002-2801410	J	WIRCam	2015-07-15	16	942	0.70	2MASS	patchy clouds
HIP99770	J	WIRCam	2015-07-16	16	942	0.70	2MASS	patchy clouds
HIP100751	J_G0802	F2	2016-08-15	14	630	0.79	VISTA	photometric

Table 4 continued

Table 4 (*continued*)

Name	Filter	Instrument	Obs. Date	Nexp	Exposition Time	FWHM	Catalog	Conditions
					(s)	(")		
HIP102141	J	WIRCam	2014-09-09	16	942	0.70	2MASS	patchy clouds
2MASSJ20434114-2433534	J	WIRCam	2015-07-17	15	884	0.20	2MASS	patchy clouds
HIP102409	J	WIRCam	2015-02-12	22	1296	0.70	2MASS	patchy clouds
HIP103311	J_G0802	F2	2014-08-01	9	612	0.70	2MASS	photometric
HIP105388	J_G0802	F2	2015-04-22	16	720	0.84	2MASS	photometric
HIP105404	J_G0802	F2	2015-04-23	14	630	0.80	VISTA	photometric
HIP107345	J_G0802	F2	2015-04-24	14	630	0.68	2MASS	photometric
HIP107947	J_G0802	F2	2015-04-23	14	630	0.85	2MASS	photometric
HIP108195	J_G0802	F2	2015-05-13	14	630	0.66	VISTA	patchy clouds
HIP108422	J_G0802	F2	2015-04-29	14	630	0.74	median	photometric
HIP109268	J_G0802	F2	2014-07-25	9	612	0.75	VISTA	patchy clouds
1RXSJ221419.3+253411	J	WIRCam	2014-09-12	21	1237	0.70	2MASS	patchy clouds
HIP110526	J	WIRCam	2014-09-09	20	1119	0.70	2MASS	patchy clouds
HIP112312	J	WIRCam	2014-09-09	20	1119	0.70	2MASS	patchy clouds
HIP113579	J_G0802	F2	2014-07-20	9	612	0.47	median	photometric
HIP114066	J	WIRCam	2016-01-19	18	1060	0.70	2MASS	patchy clouds
HR8799	J_G0802	F2	2014-07-25	9	612	0.92	median	photometric
HIP114530	J_G0802	F2	2015-04-29	14	630	0.60	median	patchy clouds
HIP115162	J	WIRCam	2015-07-16	15	942	0.70	2MASS	patchy clouds
HIP115738	J	WIRCam	2015-07-16	16	942	0.70	VISTA	patchy clouds
G190-27	J	WIRCam	2014-09-09	16	942	0.70	2MASS	patchy clouds
HIP116748	J_G0802	F2	2014-08-01	9	612	0.96	2MASS	patchy clouds
HIP116805	J	WIRCam	2015-07-15	19	1119	0.70	2MASS	patchy clouds
HD222575	J_G0802	F2	2015-09-02	14	630	0.76	2MASS	photometric
HIP117452	J_G0802	F2	2016-10-09	14	630	0.54	median	patchy clouds
HIP118121	J_G0802	F2	2016-06-10	14	630	0.99	2MASS	photometric

Table 5. z'_{ab} -band observation for all the target in the sample

Name	Filter	Instrument	Obs. Date	Nexp	Exposition Time	FWHM	Catalog	Conditions
					(s)	(")		
HIP490	z_G0328	GMOS-S	2014-09-09	8	1200	5.57	skymapper	patchy clouds
HIP560	z_G0328	GMOS-S	2014-10-10	8	1200	0.93	panstarrs	patchy clouds
HIP1113	z_G0328	GMOS-S	2015-09-02	8	520	0.76	skymapper	patchy clouds
HIP1134	z.MP9901	MegaCam	2016-09-07	4	1244	3.20	skymapper	photometric
HIP1481	z_G0328	GMOS-S	2014-07-20	9	1350	0.89	median	patchy clouds
HIP1910	z_G0328	GMOS-S	2015-08-03	9	585	0.98	skymapper	patchy clouds
HIP1993	z_G0328	GMOS-S	2015-08-24	11	715	0.88	skymapper	photometric
GJ2006A	z_G0328	GMOS-S	2016-06-10	8	520	0.99	skymapper	patchy clouds
HIP2484	z_G0328	GMOS-S	2014-09-09	8	1200	1.04	median	patchy clouds
HIP2578	z_G0328	GMOS-S	2015-08-03	8	520	1.00	median	patchy clouds
HIP2729	z_G0328	GMOS-S	2015-09-02	8	520	0.85	skymapper	patchy clouds
HIP3556	z_G0328	GMOS-S	2014-10-10	10	1500	0.90	skymapper	photometric
HIP3589	z.MP9901	MegaCam	2015-09-10	4	1245	0.56	panstarrs	photometric
HIP4448	z_G0328	GMOS-S	2014-08-26	8	1200	0.79	median	patchy clouds
G132-51B	z.MP9801	MegaCam	2014-07-18	4	1245	3.30	SDSS	photometric
HD6569	z_G0328	GMOS-S	2016-06-08	7	455	0.91	skymapper	patchy clouds
2MASSJ0112542+1526214	z.MP9801	MegaCam	2014-06-29	4	1245	3.78	SDSS	photometric
HIP6276	z_G0328	GMOS-S	2014-09-08	11	1650	0.65	panstarrs	patchy clouds
2MUCD13056	z_G0328	GMOS-S	2013-12-25	3	602	0.76	skymapper	photometric
HIP6485	z_G0328	GMOS-S	2015-09-02	8	520	0.65	skymapper	patchy clouds
G269-153	z.MP9801	MegaCam	2014-08-24	8	3809	0.59	skymapper	patchy clouds
HIP6856	z_G0328	GMOS-S	2014-10-10	10	1500	0.95	skymapper	patchy clouds
2MASSJ01351393-0712517	z_G0328	GMOS-S	2011-09-22	3	602	0.91	SDSS	photometric
G271-110	z.MP9901	MegaCam	2016-09-08	4	1244	0.67	skymapper	patchy clouds
HIP9141	z_G0328	GMOS-S	2014-10-10	12	1800	0.91	skymapper	patchy clouds
HIP9685	z_G0328	GMOS-S	2016-08-04	8	520	0.39	median	patchy clouds
HIP9892	z_G0328	GMOS-S	2015-09-03	6	390	0.75	skymapper	photometric
HIP9902	z_G0328	GMOS-S	2016-08-04	8	520	0.95	median	patchy clouds
HIP10272	z_G0328	GMOS-S	2014-10-07	8	1200	0.68	SDSS	patchy clouds
HIP10602	z_G0328	GMOS-S	2016-08-01	8	520	0.84	median	patchy clouds
HIP10679	z.MP9801	MegaCam	2014-08-24	4	1244	0.49	SDSS	photometric
HIP11152	z.MP9801	MegaCam	2014-08-24	6	1867	3.48	SDSS	photometric
HIP11360	z_G0328	GMOS-S	2015-09-28	8	520	0.86	median	patchy clouds
HIP11437	z.MP9901	MegaCam	2015-09-08	4	1244	2.84	SDSS	photometric
IRXSJ022735.8+471021	z.MP9901	MegaCam	2016-10-22	7	2178	0.76	median	patchy clouds
HIP12394	z_G0328	GMOS-S	2015-08-24	8	520	0.91	median	patchy clouds
HIP12413	z_G0328	GMOS-S	2014-07-20	8	1200	0.72	median	patchy clouds
HIP12545	z_G0328	GMOS-S	2015-09-28	7	455	0.86	SDSS	patchy clouds
AFHor	z_G0328	GMOS-S	2015-09-03	8	520	0.77	skymapper	patchy clouds
HIP12635	z.MP9901	MegaCam	2015-09-08	6	1867	0.51	panstarrs	photometric
HIP12925	z.MP9901	MegaCam	2015-09-09	4	1244	3.29	SDSS	photometric
HIP13027	z_G0328	GMOS-S	2014-09-24	8	1200	0.79	median	patchy clouds
HIP13209	z.MP9901	MegaCam	2015-09-09	4	1245	0.47	panstarrs	photometric
HIP14551	z.MP9901	MegaCam	2016-11-04	10	3111	0.77	skymapper	photometric
IS-Eri	z_G0328	GMOS-S	2014-09-08	6	900	1.08	skymapper	0
HIP14807	z_G0328	GMOS-S	2014-10-18	8	1200	0.90	median	patchy clouds
HIP14913	z_G0328	GMOS-S	2016-08-04	8	520	0.88	median	patchy clouds
HIP15247	z.MP9901	MegaCam	2015-09-08	4	1245	3.53	panstarrs	photometric

Table 5 continued

Table 5 (continued)

Name	Filter	Instrument	Obs. Date	Nexp	Exposition Time	FWHM	Catalog	Conditions
					(s)	(")		
HIP15353	z_G0328	GMOS-S	2015-09-28	8	520	0.72	median	patchy clouds
CD-351167	z_G0328	GMOS-S	2015-09-08	9	585	0.89	median	patchy clouds
CD-441173	z_G0328	GMOS-S	2015-09-28	8	520	0.94	skymapper	patchy clouds
V577-Per	z.MP9901	MegaCam	2015-09-10	4	1245	0.46	median	patchy clouds
2MASSJ03350208+2342356	z_G0328	GMOS-S	2013-01-03	3	602	1.00	panstarrs	photometric
HIP16853	z_G0328	GMOS-S	2016-08-03	8	520	1.06	median	patchy clouds
HIP17248	z.MP9901	MegaCam	2015-09-08	4	1245	0.48	panstarrs	photometric
HIP17695	z.MP9801	MegaCam	2014-10-22	4	1244	3.42	skymapper	photometric
HIP17764	z_G0328	GMOS-S	2015-09-29	8	520	0.95	skymapper	patchy clouds
HIP17782	z.MP9901	MegaCam	2015-09-09	4	1245	0.49	panstarrs	photometric
HIP17797	z_G0328	GMOS-S	2015-09-03	8	520	0.82	median	patchy clouds
HIP18714	z_G0328	GMOS-S	2016-02-11	8	520	0.61	median	photometric
HIP18859	z.MP9801	MegaCam	2014-08-26	4	1244	0.53	SDSS	photometric
HIP19183	z.MP9901	MegaCam	2015-09-09	4	1244	0.50	panstarrs	photometric
1RXSJ041417.0-090650	z.MP9901	MegaCam	2016-09-08	4	1244	0.63	skymapper	photometric
HIP21547	z.MP9801	MegaCam	2014-08-29	8	2489	3.59	skymapper	photometric
HIP21632	z.MP9901	MegaCam	2016-09-08	4	1244	0.69	skymapper	photometric
HIP21965	z.MP9901	MegaCam	2016-09-08	4	1244	0.70	skymapper	photometric
HIP22295	z_G0328	GMOS-S	2016-02-15	8	520	0.79	skymapper	patchy clouds
TYC5899-0026-1	z_G0328	GMOS-S	2016-02-17	8	520	0.76	panstarrs	patchy clouds
CD-561032	z_G0328	GMOS-S	2012-09-20	3	602	1.43	skymapper	photometric
HIP23179	z.MP9901	MegaCam	2015-09-15	4	1245	0.72	panstarrs	photometric
HIP23200	z.MP9801	MegaCam	2014-10-22	4	1244	3.16	panstarrs	photometric
HIP23309	z_G0328	GMOS-S	2015-09-28	8	520	0.98	median	patchy clouds
HIP23362	z.MP9901	MegaCam	2017-01-28	10	4761	0.84	panstarrs	photometric
HIP23418	z.MP9801	MegaCam	2014-10-26	9	2800	0.89	panstarrs	photometric
GJ3331	z.MP9801	MegaCam	2014-10-23	10	3111	3.38	skymapper	photometric
HIP24947	z_G0328	GMOS-S	2013-10-10	3	602	0.56	median	photometric
HIP25283	z.MP9801	MegaCam	2014-10-30	5	2380	5.06	skymapper	photometric
HIP25486	z.MP9801	MegaCam	2014-10-27	4	1244	0.55	skymapper	photometric
HD36705B	z_G0328	GMOS-S	2015-08-23	8	520	0.73	skymapper	patchy clouds
HIP26309	z.MP9901	MegaCam	2016-01-01	8	2489	4.11	skymapper	photometric
HIP26369	z_G0328	GMOS-S	2016-02-11	9	585	0.56	skymapper	photometric
HIP26453	z.MP9901	MegaCam	2016-01-01	8	2489	0.73	skymapper	photometric
HIP26990	z_G0328	GMOS-S	2015-09-08	12	780	0.95	skymapper	patchy clouds
HIP27321	z_G0328	GMOS-S	2015-09-28	8	520	0.82	median	patchy clouds
HIP28036	z_G0328	GMOS-S	2015-09-28	8	520	0.85	skymapper	patchy clouds
HIP28474	z_G0328	GMOS-S	2015-03-14	9	1350	0.47	skymapper	patchy clouds
AP-Col	z.MP9801	MegaCam	2014-10-28	5	2380	3.62	skymapper	photometric
2MASSJ06085283-2753583	z_G0328	GMOS-S	2012-10-12	3	602	0.91	skymapper	photometric
Cd-352722	z.MP9801	MegaCam	2014-10-27	6	1867	0.76	skymapper	photometric
2MASSJ06131330-2742054	z.MP9801	MegaCam	2014-11-17	4	1244	0.75	skymapper	photometric
HIP29964	z_G0328	GMOS-S	2014-09-09	8	1200	1.34	skymapper	patchy clouds
HIP30030	z.MP9901	MegaCam	2015-09-17	5	1555	0.80	skymapper	photometric
HIP30034	z_G0328	GMOS-S	2015-03-14	9	1350	0.55	median	patchy clouds
HIP30314	z_G0328	GMOS-S	2016-02-14	8	520	0.62	median	photometric
AK-Pic	z_G0328	GMOS-S	2016-02-14	9	585	0.70	skymapper	photometric
CD-611439	z_G0328	GMOS-S	2016-02-11	8	520	0.59	skymapper	photometric
HIP32104	z.MP9901	MegaCam	2015-09-15	4	1245	0.79	median	patchy clouds
HIP32235	z_G0328	GMOS-S	2015-03-14	9	1350	0.80	skymapper	patchy clouds
HIP32435	z_G0328	GMOS-S	2015-03-16	9	1350	0.59	skymapper	patchy clouds

Table 5 continued

Table 5 (continued)

Name	Filter	Instrument	Obs. Date	Nexp	Exposition Time	FWHM	Catalog	Conditions
					(s)	(")		
HIP33737	z_G0328	GMOS-S	2015-03-15	9	1350	0.64	median	patchy clouds
BD+201790	z.MP9801	MegaCam	2014-10-30	5	1555	3.61	panstarrs	photometric
GJ2060C	z.MP9801	MegaCam	2014-11-18	4	1904	4.07	skymapper	photometric
HIP36948	z_G0328	GMOS-S	2016-08-31	8	520	0.62	skymapper	photometric
HIP47135	z_G0328	GMOS-S	2015-03-14	9	1350	0.69	skymapper	patchy clouds
TWA21	z_G0328	GMOS-S	2015-03-03	9	1350	0.86	skymapper	patchy clouds
HIP50191	z_G0328	GMOS-S	2016-01-02	8	520	0.83	median	patchy clouds
TWA22	z_G0328	GMOS-S	2015-11-16	8	520	0.80	skymapper	patchy clouds
HIP51317	z.MP9901	MegaCam	2016-01-02	4	1244	3.30	SDSS	photometric
TWA1	z.MP9901	MegaCam	2016-04-12	6	2856	0.93	skymapper	patchy clouds
TWA2	z.MP9901	MegaCam	2016-01-01	5	2381	0.83	skymapper	photometric
TWA12	z_G0328	GMOS-S	2016-02-10	8	520	0.66	skymapper	patchy clouds
TWA13	z_G0328	GMOS-S	2016-01-31	12	780	0.73	median	patchy clouds
TWA4	z.MP9901	MegaCam	2016-01-01	4	1244	0.70	skymapper	photometric
TWA5	z_G0328	GMOS-S	2015-11-22	10	650	0.69	skymapper	patchy clouds
TWA30A	z.MP9901	MegaCam	2016-12-24	6	2857	0.69	skymapper	photometric
TWA8B	z.MP9901	MegaCam	2016-01-02	4	1244	0.66	skymapper	photometric
TWA26	z.MP9901	GMOS-S	2016-01-02	4	1904	3.71	skymapper	photometric
TWA9	z_G0328	GMOS-S	2016-02-10	8	520	0.71	skymapper	0
HIP57632	z.MP9801	MegaCam	2015-01-16	8	2489	4.00	panstarrs	photometric
TWA23	z.MP9901	MegaCam	2016-01-03	6	2856	0.83	skymapper	patchy clouds
TWA27	z_G0328	GMOS-S	2015-12-17	8	520	0.84	skymapper	patchy clouds
TWA25	z_G0328	GMOS-S	2016-02-23	9	585	0.89	skymapper	patchy clouds
TWA11C	z_G0328	GMOS-S	2016-02-15	8	520	0.76	median	patchy clouds
GJ490	z.MP9801	MegaCam	2014-07-03	8	2489	4.40	SDSS	patchy clouds
PX-Vir	z.MP9801	MegaCam	2014-07-03	4	1244	0.47	skymapper	photometric
GJ1167	z.MP9801	MegaCam	2014-07-03	4	1244	3.49	SDSS	photometric
HIP68994	z_G0328	GMOS-S	2015-03-09	9	1350	0.46	median	photometric
HIP74405	z_G0328	GMOS-S	2015-03-02	7	1050	0.80	skymapper	patchy clouds
HIP76629	z_G0328	GMOS-S	2015-03-04	8	1200	0.60	median	patchy clouds
HIP76768	z.MP9901	MegaCam	2016-05-30	4	1244	0.55	skymapper	photometric
HIP79797	z_G0328	GMOS-S	2015-03-14	9	1350	0.64	median	patchy clouds
HIP79881	z_G0328	GMOS-S	2014-08-26	8	1200	0.53	panstarrs	photometric
HIP81084	z_G0328	GMOS-S	2014-09-08	9	1350	0.76	skymapper	patchy clouds
HIP82688	z.MP9901	MegaCam	2016-09-06	4	1244	3.01	skymapper	patchy clouds
HIP83494	z.MP9901	MegaCam	2015-08-20	5	1556	0.71	median	patchy clouds
HIP84586	z_G0328	GMOS-S	2014-08-26	8	1200	0.83	skymapper	patchy clouds
HIP84642	z_G0328	GMOS-S	2015-03-22	9	1350	0.70	skymapper	patchy clouds
HIP86346	z.MP9901	MegaCam	2016-09-06	4	1245	0.50	median	patchy clouds
HIP88399	z_G0328	GMOS-S	2016-02-17	10	650	1.09	skymapper	patchy clouds
HR6750	z_G0328	GMOS-S	2014-09-02	15	2250	1.24	median	patchy clouds
HIP92024	z_G0328	GMOS-S	2016-02-24	8	520	0.79	median	patchy clouds
HIP92680	z_G0328	GMOS-S	2016-03-06	8	520	0.72	skymapper	patchy clouds
HIP94235	z_G0328	GMOS-S	2015-08-24	8	520	0.81	skymapper	patchy clouds
Eta-TeLA	z_G0328	GMOS-S	2014-09-03	11	1650	1.06	median	patchy clouds
HIP95347	z_G0328	GMOS-S	2016-03-14	8	520	0.72	median	patchy clouds
HIP98495	z_G0328	GMOS-S	2014-10-09	8	1200	0.68	median	patchy clouds
HIP99273	z_G0328	GMOS-S	2016-03-10	9	585	0.75	skymapper	patchy clouds
2MASSJ20100002-2801410	z.MP9901	MegaCam	2015-07-10	6	1867	0.79	skymapper	patchy clouds
HIP99770	z.MP9901	MegaCam	2015-06-10	4	1245	0.59	panstarrs	patchy clouds
HIP100751	z_G0328	GMOS-S	2016-08-05	6	390	0.97	median	patchy clouds

Table 5 continued

Table 5 (continued)

Name	Filter	Instrument	Obs. Date	Nexp	Exposition Time	FWHM	Catalog	Conditions
					(s)	(")		
HIP102141	z.MP9801	MegaCam	2014-06-28	3	1428	3.63	skymapper	patchy clouds
2MASSJ20434114-2433534	z.MP9901	MegaCam	2016-09-06	4	1244	0.63	skymapper	photometric
HIP102409	z.MP9801	MegaCam	2014-09-18	5	2380	4.11	skymapper	patchy clouds
HIP103311	z_G0328	GMOS-S	2016-03-25	8	520	0.84	median	patchy clouds
HIP105388	z_G0328	GMOS-S	2015-03-31	9	1350	0.85	skymapper	patchy clouds
HIP105404	z_G0328	GMOS-S	2015-04-18	13	1950	0.80	skymapper	patchy clouds
HIP107345	z_G0328	GMOS-S	2015-04-19	12	1800	0.94	skymapper	photometric
HIP107947	z_G0328	GMOS-S	2015-04-01	9	1350	0.67	skymapper	patchy clouds
HIP108195	z_G0328	GMOS-S	2015-04-23	12	1800	0.74	median	patchy clouds
HIP108422	z_G0328	GMOS-S	2015-06-04	13	1950	0.74	skymapper	patchy clouds
HIP109268	z_G0328	GMOS-S	2014-09-07	8	1200	0.86	median	patchy clouds
IRXSJ221419.3+253411	z.MP9801	MegaCam	2014-06-22	4	1245	2.96	median	photometric
HIP110526	z.MP9801	MegaCam	2014-06-22	4	1245	3.05	median	patchy clouds
HIP112312	z.MP9801	MegaCam	2014-07-01	8	3809	0.65	skymapper	photometric
HIP113579	z_G0328	GMOS-S	2014-07-20	8	1200	0.65	panstarrs	patchy clouds
HIP114066	z.MP9801	MegaCam	2014-07-01	4	1245	0.71	panstarrs	patchy clouds
HR8799	z_G0328	GMOS-S	2015-08-24	8	520	0.84	SDSS	patchy clouds
HIP114530	z_G0328	GMOS-S	2015-05-13	9	1350	0.67	median	patchy clouds
HIP115162	z.MP9901	MegaCam	2016-09-07	4	1244	0.53	panstarrs	patchy clouds
HIP115738	z.MP9901	MegaCam	2016-09-07	4	1244	0.47	median	photometric
G190-27	z.MP9801	MegaCam	2014-06-23	4	1245	2.73	panstarrs	photometric
HIP116748	z_G0328	GMOS-S	2016-05-22	8	520	1.10	skymapper	patchy clouds
HIP116805	z.MP9901	MegaCam	2016-09-07	4	1245	0.62	SDSS	patchy clouds
HD222575	z_G0328	GMOS-S	2016-06-22	8	520	0.80	skymapper	patchy clouds
HIP117452	z_G0328	GMOS-S	2015-08-03	9	585	0.89	panstarrs	patchy clouds
HIP118121	z_G0328	GMOS-S	2015-05-13	9	1350	0.75	median	patchy clouds

Table 6. 7σ detection limits in the J band

Name	a_{min}	a_{max}	a_{min}	a_{min}	J	M_J	Mass Limit
	'	'	AU	AU		'	M_{Jup}
HIP490	32	180	1241	7096	22.1	19.1	1.0
HIP560	46	180	1808	7096	20.7	17.7	1.7
HIP1113	5	180	232	8001	21.0	17.7	1.7
HIP1134	19	630	877	29717	21.8	18.5	1.3
HIP1481	27	180	1137	7486	20.6	17.5	1.8
HIP1910	22	180	1163	9543	21.5	17.9	1.6
HIP1993	23	180	1055	8254	21.4	18.1	1.5
GJ2006A	26	180	823	5802	21.3	18.8	1.2
HIP2484	72	180	2996	7461	20.0	16.9	2.2
HIP2578	52	180	2378	8209	21.0	17.7	1.7
HIP2729	28	180	1242	7917	21.6	18.4	1.4
HIP3556	15	180	596	7271	21.3	18.2	1.4
HIP3589	2	630	126	33104	21.2	17.6	1.8
HIP4448	22	180	907	7321	20.9	17.8	1.7
G132-51B	17	630	512	18871	22.6	20.2	0.7
HD6569	3	180	153	8531	22.2	18.8	1.1
2MASSJ01112542+1526214	8	630	183	13741	22.3	20.6	0.6
HIP6276	27	180	935	6198	20.8	18.1	1.5
2MUCD13056	5	180	220	7586	20.7	17.6	1.8
HIP6485	19	180	945	8924	21.6	18.1	1.5
G269-153	15	630	377	15837	21.7	19.7	0.9
HIP6856	26	180	953	6491	20.6	17.8	1.7
2MASSJ01351393-0712517	13	180	505	6825	20.9	18.0	1.6
G271-110	11	630	259	15127	21.0	19.1	1.0
HIP9141	21	180	861	7369	22.0	19.0	1.1
HIP9685	30	180	1410	8605	20.5	17.2	2.0
HIP9892	22	180	1137	9179	20.4	16.9	2.2
HIP9902	36	180	1574	7958	21.1	17.9	1.6
HIP10272	33	180	1193	6600	20.6	17.8	1.7
HIP10602	53	180	2519	8491	21.7	18.4	1.4
HIP10679	33	630	894	17231	21.1	18.9	1.1
HIP11152	2	630	60	18081	21.3	19.0	1.0
HIP11360	15	180	685	8069	23.2	20.0	0.8
HIP11437	2	630	96	25182	22.3	19.3	0.9
IRXSJ022735.8+471021	11	630	304	17270	20.3	18.1	4.0
HIP12394	53	180	2480	8388	21.0	17.7	4.7
HIP12413	26	180	919	6430	22.1	19.3	2.7
HIP12545	19	180	779	7574	21.6	18.4	3.7
AFHor	30	180	806	4775	21.0	18.9	3.1
HIP12635	17	630	847	31785	22.0	18.5	3.6
HIP12925	15	630	815	34237	21.7	18.0	4.2
HIP13027	34	180	1142	6046	20.7	18.1	4.1
HIP13209	41	630	2087	32011	22.4	18.8	3.2
HIP14551	25	630	1377	34443	20.6	17.0	5.9
IS-Eri	27	180	997	6741	21.2	18.3	3.9
HIP14807	34	180	1373	7236	21.5	18.5	3.6
HIP14913	52	180	2218	7657	21.1	18.0	4.3
HIP15247	31	180	1524	8871	23.1	19.6	2.4
HIP15353	42	180	2295	9900	21.3	17.6	4.8

Table 6 continued

Table 6 (continued)

Name	a_{min}	a_{max}	a_{min}	a_{min}	J	M_J	Mass Limit
	'	'	AU	AU		'	M_{Jup}
CD-351167	15	180	714	8829	22.2	18.7	3.3
CD-441173	30	180	1240	7568	20.6	17.5	5.0
V577-Per	6	630	206	21675	20.8	18.1	4.1
2MASSJ03350208+2342356	2	630	76	26708	20.8	17.6	4.8
HIP16853	34	180	1467	7810	21.7	18.5	3.5
HIP17248	8	630	264	22194	20.8	18.1	4.2
HIP17695	13	630	208	10166	22.2	21.2	1.5
HIP17764	33	180	1761	9739	21.3	17.6	4.8
HIP17782	7	630	341	32574	20.5	16.9	6.0
HIP17797	60	180	3068	9142	20.0	16.5	6.9
HIP18714	17	180	829	8738	21.4	18.0	4.2
HIP18859	34	630	633	11870	22.0	20.6	1.8
HIP19183	17	630	911	34785	20.7	17.0	5.9
IRXSJ041417.0-090650	2	630	43	15007	22.3	20.4	1.9
HIP21547	24	630	697	18549	22.1	19.8	2.3
HIP21632	17	630	927	35410	21.6	17.9	4.4
HIP21965	23	630	1449	40070	20.6	16.6	6.6
HIP22295	30	180	1812	10993	21.2	17.3	5.2
TYC5899-0026-1	26	180	790	5495	20.8	18.4	3.8
CD-561032	29	180	328	2014	20.7	20.5	1.8
HIP23179	37	630	1913	32948	21.0	17.4	5.1
HIP23200	4	630	93	16312	20.7	18.7	3.4
HIP23309	28	180	757	4825	21.3	19.2	2.8
HIP23362	36	630	2166	38246	21.2	17.3	5.3
HIP23418	24	630	605	15687	20.9	18.9	3.1
GJ3331	38	630	731	12098	21.0	19.6	2.4
HIP24947	25	180	1217	8704	21.0	17.6	4.8
HIP25283	41	630	734	11347	21.4	20.1	2.0
HIP25486	31	630	836	17044	21.8	19.7	2.4
HD36705B	41	180	616	2693	20.3	19.4	2.6
HIP26309	34	630	1774	33279	20.9	17.3	1.3
HIP26369	33	180	840	4619	22.0	20.0	0.6
HIP26453	20	630	1141	35792	20.9	17.1	1.4
HIP26990	21	180	1146	9977	21.3	17.6	1.2
HIP27321	60	180	1169	3503	20.7	19.3	0.7
HIP28036	37	180	1997	9798	20.9	17.2	1.4
HIP28474	15	180	785	9468	20.6	17.0	1.5
AP-Col	4	630	30	5287	22.3	22.7	0.0
2MASSJ06085283-2753583	3	180	101	5631	20.5	18.1	1.0
Cd-352722	3	630	57	13411	20.9	19.3	0.7
2MASSJ06131330-2742054	6	630	185	18531	20.5	18.1	1.0
HIP29964	15	180	583	6946	19.7	16.8	1.6
HIP30030	3	630	162	31034	20.2	16.8	1.6
HIP30034	17	180	771	8299	21.6	18.3	0.9
HIP30314	44	180	1057	4285	23.5	21.6	0.8
AK-Pic	44	180	939	3837	22.6	20.9	0.9
CD-611439	25	180	551	4027	21.7	19.9	1.4
HIP32104	33	630	1453	27500	21.4	18.2	2.4
HIP32235	2	180	105	10494	21.0	17.2	3.4
HIP32435	22	180	1230	10094	20.7	17.0	3.7
HIP33737	24	180	1429	10599	21.2	17.3	3.2

Table 6 continued

Table 6 (continued)

Name	a_{min}	a_{max}	a_{min}	a_{min}	J	M_J	Mass Limit
	'	'	AU	AU		'	M_{Jup}
BD+201790	21	630	534	16245	23.1	21.0	0.9
GJ2060C	3	630	40	9393	20.6	19.8	1.5
HIP36948	16	180	554	6369	19.3	16.6	4.2
HIP47135	24	180	1603	12249	20.7	16.5	4.2
TWA21	172	180	9399	9873	20.1	16.4	4.5
HIP50191	54	180	1672	5599	20.3	17.8	2.8
TWA22	20	180	347	3161	19.8	18.5	2.2
HIP51317	33	630	543	10274	20.6	19.5	1.6
TWA1	2	630	129	33851	20.9	17.2	3.4
TWA2	32	630	1466	29344	20.5	17.2	3.4
TWA12	24	180	1547	11557	22.1	18.1	2.5
TWA13	29	180	1622	10021	21.0	17.3	3.3
TWA4	4	630	162	28303	21.6	18.4	2.3
TWA5	30	180	1487	9023	21.3	17.8	2.8
TWA30A	2	630	101	26473	20.9	17.8	2.8
TWA8B	2	630	113	29619	21.6	18.3	2.4
TWA26	6	630	264	26461	20.8	17.7	2.9
TWA9	20	180	918	8428	22.3	18.9	1.9
HIP57632	102	630	1125	6933	21.9	21.7	0.7
TWA23	17	630	922	33978	20.2	16.5	4.3
TWA27	3	180	133	9483	22.3	18.7	2.0
TWA25	26	180	1403	9750	21.4	17.8	2.8
TWA11C	25	180	1727	12435	21.6	17.4	3.1
GJ490	5	630	82	11418	21.3	20.1	1.3
PX-Vir	22	630	475	13672	22.0	20.3	1.2
GJ1167	8	630	97	7245	21.0	20.7	1.0
HIP68994	13	180	820	11557	19.0	15.0	7.2
HIP74405	19	180	960	9063	21.1	17.6	3.0
HIP76629	4	180	160	6943	18.4	15.5	6.1
HIP76768	4	630	145	25334	20.2	17.2	3.4
HIP79797	4	180	216	9409	21.5	17.9	2.7
HIP79881	20	180	832	7439	20.9	17.8	2.8
HIP81084	13	180	403	5527	21.4	19.0	1.9
HIP82688	3	630	140	29453	20.7	17.3	3.3
HIP83494	3	630	165	34651	21.1	17.4	3.1
HIP84586	44	180	1398	5666	20.8	18.3	2.4
HIP84642	24	180	1400	10618	20.9	17.0	3.6
HIP86346	16	630	527	20878	22.0	19.4	1.7
HIP88399	21	180	1023	8675	19.9	16.5	4.2
HR6750	42	180	1777	7539	20.3	17.2	3.4
HIP92024	65	180	1860	5144	21.0	18.7	2.0
HIP92680	24	180	1261	9278	21.3	17.8	2.8
HIP94235	30	180	1811	11054	21.0	17.1	3.6
Eta-TeLA	48	180	2317	8688	21.5	18.0	2.6
HIP95347	49	180	2729	10043	21.3	17.6	3.0
HIP98495	64	180	2070	5805	21.7	19.1	1.8
HIP99273	29	180	1532	9409	21.5	17.9	2.7
2MASSJ20100002-2801410	10	630	460	28427	23.0	19.7	1.5
HIP99770	2	630	102	26913	19.3	16.2	4.9
HIP100751	82	180	4500	9878	19.3	15.6	5.9
HIP102141	56	630	603	6741	21.1	20.9	0.9

Table 6 continued

Table 6 (continued)

Name	a_{min}	a_{max}	a_{min}	a_{min}	J	M_J	Mass Limit
	'	'	AU	AU		'	M_{Jup}
2MASSJ20434114-2433534	2	630	59	17711	20.9	18.7	2.0
HIP102409	37	630	363	6246	21.2	21.3	0.9
HIP103311	30	180	1381	8227	21.5	18.2	2.4
HIP105388	30	180	1292	7743	21.2	18.0	2.6
HIP105404	31	180	1384	8008	22.3	19.0	1.9
HIP107345	17	180	723	7865	21.6	18.4	2.3
HIP107947	36	180	1640	8168	21.0	17.7	2.9
HIP108195	30	180	1414	8373	20.0	16.7	4.0
HIP108422	23	180	1337	10457	21.7	17.9	2.7
HIP109268	67	180	2063	5580	18.8	16.3	4.6
1RXSJ221419.3+253411	3	630	86	18112	21.9	19.6	1.6
HIP110526	32	630	493	9777	22.1	21.1	0.9
HIP112312	3	630	77	14713	20.9	19.1	1.8
HIP113579	22	180	664	5542	22.9	20.4	1.1
HIP114066	2	630	51	15445	20.7	18.8	2.0
HR8799	46	180	1830	7099	21.6	18.7	2.1
HIP114530	24	180	1243	9146	22.0	18.4	2.2
HIP115162	2	630	120	31610	20.4	16.9	2.2
HIP115738	32	630	1482	29661	20.7	17.3	1.9
G190-27	3	630	49	9324	22.3	21.5	0.4
HIP116748	27	180	1242	8342	20.4	17.1	5.7
HIP116805	46	630	2354	32540	21.9	18.3	0.9
HD222575	26	180	1685	11476	21.5	17.5	3.0
HIP117452	53	180	2245	7593	21.4	18.3	2.4
HIP118121	54	180	2562	8547	20.8	17.5	3.1

Table 7. 7σ detection limits in the [4.5] band

Name	a_{min}	a_{max}	a_{min}	a_{min}	[4.5]	$M_{[4.5]}$	Mass Limit
	'	'	AU	AU		'	M_{Jup}
HIP490	28	479	1087	18858	18.7	15.7	0.3
HIP560	25	479	993	18858	18.4	15.4	0.4
HIP1113	28	479	1226	21261	18.8	15.6	0.3
HIP1134	24	479	1132	22574	18.2	14.8	0.7
HIP1481	25	479	1047	19892	18.5	15.4	0.4
HIP1910	26	479	1398	25360	18.7	15.0	0.6
HIP1993	22	479	989	21933	18.8	15.5	0.4
GJ2006A	20	479	657	15417	18.8	16.2	< 0.5
HIP2484	66	479	2733	19826	17.4	14.3	0.9
HIP2578	28	479	1257	21813	18.4	15.1	0.5
HIP2729	30	479	1318	21037	18.8	15.6	0.3
HIP3556	25	479	1017	19322	18.8	15.7	0.3
HIP3589	29	479	1513	25147	18.0	14.4	0.9
HIP4448	25	479	1024	19456	18.7	15.7	0.3
G132-51B	25	479	754	14335	18.5	16.1	0.1
HD6569	29	479	1364	22670	18.7	15.3	0.5
2MASSJ01112542+1526214	19	479	419	10438	18.6	17.0	< 0.5
HIP6276	35	479	1197	16471	18.4	15.7	0.3
2MUCD13056	11	479	455	20157	18.8	15.7	0.3
HIP6485	30	479	1486	23715	18.8	15.3	0.5
G269-153	26	479	663	12030	18.5	16.5	< 0.5
HIP6856	28	479	994	17248	18.6	15.9	0.2
2MASSJ01351393-0712517	14	479	545	18136	18.5	15.6	0.3
G271-110	16	479	374	11491	18.6	16.7	< 0.5
HIP9141	29	479	1178	19583	18.7	15.7	0.3
HIP9685	24	479	1146	22865	18.6	15.2	0.5
HIP9892	29	479	1467	24391	18.8	15.2	0.5
HIP9902	31	479	1378	21148	18.6	15.3	0.4
HIP10272	36	479	1319	17538	18.5	15.7	0.3
HIP10602	17	479	792	22564	17.3	13.9	1.2
HIP10679	36	479	984	13089	18.3	16.1	0.1
HIP11152	17	479	482	13735	18.5	16.2	< 0.5
HIP11360	28	479	1236	21442	16.7	13.5	1.7
HIP11437	29	479	1151	19129	18.6	15.5	0.4
1RXSJ022735.8+471021	14	479	395	13119	18.2	16.1	1.1
HIP12394	31	479	1453	22291	18.0	14.7	2.3
HIP12413	42	479	1499	17088	18.0	15.2	1.7
HIP12545	22	479	908	20126	18.6	15.5	1.5
AFHor	31	479	827	12688	18.6	16.5	0.9
HIP12635	36	479	1815	24145	18.5	15.0	1.9
HIP12925	28	479	1499	26008	18.5	14.8	2.1
HIP13027	37	479	1248	16067	18.3	15.7	1.3
HIP13209	52	479	2621	24317	17.5	14.0	3.5
HIP14551	24	479	1311	26164	18.3	14.6	2.4
IS-Eri	23	479	853	17912	18.5	15.7	1.4
HIP14807	22	479	867	19229	18.4	15.4	1.6
HIP14913	64	479	2703	20348	18.0	14.9	2.0
HIP15247	28	479	1359	23575	18.6	15.1	1.8

Table 7 continued

Table 7 (continued)

Name	a_{min}	a_{max}	a_{min}	a_{min}	[4.5]	$M_{[4.5]}$	Mass Limit
	'	'	AU	AU		'	M_{Jup}
HIP15353	35	479	1912	26308	18.9	15.2	1.8
CD-351167	23	479	1117	23461	18.8	15.4	1.6
CD-441173	24	479	1008	20110	18.8	15.7	1.4
V577-Per	42	479	1444	16465	18.1	15.4	1.6
2MASSJ03350208+2342356	10	479	407	20288	18.5	15.3	1.6
HIP16853	32	479	1404	20754	18.6	15.4	1.6
HIP17248	18	479	634	16859	17.6	14.8	2.1
HIP17695	29	479	465	7723	18.6	17.5	0.5
HIP17764	31	479	1686	25881	18.7	15.0	1.9
HIP17782	22	479	1116	24744	17.6	14.1	3.3
HIP17797	44	479	2253	24292	18.0	14.5	2.6
HIP18714	36	479	1746	23220	18.7	15.3	1.7
HIP18859	49	479	927	9017	17.8	16.4	0.9
HIP19183	23	479	1258	26424	18.4	14.7	2.3
1RXSJ041417.0-090650	14	479	343	11400	18.7	16.8	0.8
HIP21547	32	479	954	14091	17.7	15.4	1.6
HIP21632	28	479	1551	26899	18.7	15.0	1.9
HIP21965	29	479	1831	30439	18.6	14.6	2.4
HIP22295	25	479	1538	29213	18.7	14.8	2.1
TYC5899-0026-1	19	479	586	14602	17.5	15.1	1.9
CD-561032	47	479	523	5352	18.3	18.1	0.3
HIP23179	41	479	2133	25029	17.5	13.9	3.6
HIP23200	25	479	652	12391	18.6	16.5	0.9
HIP23309	29	479	771	12823	18.8	16.6	0.8
HIP23362	32	479	1966	29053	18.3	14.4	2.8
HIP23418	31	479	777	11916	18.5	16.5	0.9
GJ3331	50	479	967	9190	18.4	16.9	0.7
HIP24947	28	479	1333	23130	18.5	15.1	1.9
HIP25283	23	479	410	8619	18.6	17.3	0.6
HIP25486	26	479	714	12948	18.2	16.1	1.1
HD36705B	38	479	574	7157	17.4	16.6	0.8
HIP26309	28	479	1457	25280	18.5	14.9	0.4
HIP26369	34	479	861	12274	18.5	16.5	< 0.5
HIP26453	23	479	1295	27189	18.6	14.8	0.4
HIP26990	22	479	1196	26512	18.5	14.8	0.4
HIP27321	60	479	1166	9308	17.0	15.5	0.1
HIP28036	29	479	1566	26036	18.7	15.0	0.3
HIP28474	22	479	1135	25160	18.7	15.1	0.3
AP-Col	32	479	272	4016	18.6	18.9	< 0.5
2MASSJ06085283-2753583	8	479	263	14963	18.9	16.4	< 0.5
Cd-352722	28	479	587	10187	18.6	16.9	< 0.5
2MASSJ06131330-2742054	29	479	847	14077	18.5	16.2	< 0.5
HIP29964	26	479	1018	18458	18.4	15.5	0.1
HIP30030	26	479	1300	23575	18.1	14.6	0.5
HIP30034	18	479	829	22054	17.5	14.2	0.7
HIP30314	30	479	713	11386	18.5	16.6	0.3
AK-Pic	35	479	741	10196	18.0	16.4	0.5
CD-611439	23	479	510	10702	18.6	16.9	0.2
HIP32104	31	479	1361	20890	17.9	14.7	1.4
HIP32235	22	479	1258	27886	18.5	14.6	1.5
HIP32435	30	479	1681	26824	18.4	14.6	1.5

Table 7 continued

Table 7 (continued)

Name	a_{min}	a_{max}	a_{min}	a_{min}	[4.5]	$M_{[4.5]}$	Mass Limit
	'	'	AU	AU		'	M_{Jup}
HIP33737	19	479	1129	28165	18.5	14.7	1.4
BD+201790	25	479	649	12340	18.3	16.2	0.5
GJ2060C	16	479	232	7136	17.3	16.5	0.4
HIP36948	22	479	764	16925	17.3	14.6	1.5
HIP47135	23	479	1550	32549	18.2	14.0	2.0
TWA21	12	479	658	26236	16.4	12.8	4.2
HIP50191	37	479	1156	14879	17.3	14.9	1.2
TWA22	12	479	211	8400	16.0	14.8	1.3
HIP51317	35	479	567	7804	18.2	17.2	0.1
TWA1	19	479	1031	25714	18.8	15.1	1.0
TWA2	30	479	1397	22291	18.6	15.3	0.9
TWA12	19	479	1232	30712	18.5	14.5	1.6
TWA13	30	479	1669	26630	18.6	14.8	1.3
TWA4	23	479	1024	21500	18.6	15.4	0.9
TWA5	23	479	1142	23976	18.6	15.1	1.0
TWA30A	0	0	0	0	0.00	-3.1	319
TWA8B	26	479	1241	22500	18.5	15.2	1.0
TWA26	10	479	403	20101	18.9	15.8	0.7
TWA9	34	479	1572	22395	18.5	15.2	1.0
HIP57632	62	479	686	5267	15.4	15.2	1.0
TWA23	20	479	1100	25811	18.7	15.0	1.1
TWA27	10	479	505	25200	18.4	14.8	1.3
TWA25	25	479	1364	25909	18.7	15.1	1.0
TWA11C	14	479	994	33043	18.5	14.3	1.8
GJ490	34	479	609	8674	18.7	17.4	< 0.5
PX-Vir	37	479	807	10386	18.5	16.8	0.3
GJ1167	7	479	83	5503	18.8	18.5	< 0.5
HIP68994	7	479	462	30712	13.0	8.97	41.
HIP74405	18	479	905	24085	17.8	14.3	1.7
HIP76629	12	479	462	18451	13.8	10.8	11.
HIP76768	28	479	1109	19244	18.4	15.4	0.9
HIP79797	23	479	1191	25003	17.1	13.5	2.7
HIP79881	26	479	1090	19769	17.3	14.2	1.8
HIP81084	28	479	847	14687	18.4	16.0	0.6
HIP82688	23	479	1065	22374	18.2	14.9	1.2
HIP83494	29	479	1583	26322	18.7	15.0	1.1
HIP84586	35	479	1094	15057	17.5	15.0	1.1
HIP84642	14	479	849	28214	17.3	13.5	2.9
HIP86346	37	479	1232	15860	18.7	16.1	0.6
HIP88399	29	479	1387	23052	17.2	13.8	2.4
HR6750	30	479	1255	20033	16.2	13.1	3.5
HIP92024	38	479	1096	13668	17.4	15.2	1.0
HIP92680	24	479	1236	24655	17.9	14.4	1.7
HIP94235	19	479	1178	29374	18.3	14.3	1.7
Eta-TeLA	30	479	1446	23086	18.2	14.7	1.4
HIP95347	36	479	2007	26689	17.6	13.9	2.2
HIP98495	37	479	1198	15425	17.8	15.3	0.9
HIP99273	25	479	1316	25003	18.4	14.8	1.3
2MASSJ20100002-2801410	14	479	649	21594	18.4	15.2	1.0
HIP99770	22	479	922	20444	14.9	11.8	7.4
HIP100751	36	479	1974	26250	16.5	12.8	4.2

Table 7 continued

Table 7 (continued)

Name	a_{min}	a_{max}	a_{min}	a_{min}	[4.5]	$M_{[4.5]}$	Mass Limit
	'	'	AU	AU		'	M_{Jup}
HIP102141	38	479	411	5121	17.3	17.2	0.1
2MASSJ20434114-2433534	19	479	540	13454	18.3	16.1	0.6
HIP102409	38	479	381	4745	17.4	17.4	< 0.5
HIP103311	25	479	1151	21863	18.4	15.1	1.1
HIP105388	25	479	1083	20576	18.6	15.5	0.9
HIP105404	24	479	1067	21280	18.7	15.5	0.8
HIP107345	20	479	890	20899	18.6	15.4	0.9
HIP107947	25	479	1142	21704	18.6	15.4	0.9
HIP108195	31	479	1450	22249	18.4	15.1	1.1
HIP108422	25	479	1463	27789	18.5	14.7	1.4
HIP109268	60	479	1858	14828	15.7	13.2	3.2
1RXSJ221419.3+253411	18	479	517	13759	18.7	16.5	0.4
HIP110526	34	479	521	7427	18.4	17.5	< 0.5
HIP112312	31	479	728	11176	18.3	16.5	0.4
HIP113579	30	479	923	14728	18.0	15.6	0.8
HIP114066	14	479	353	11732	16.9	14.9	1.2
HR8799	38	479	1513	18865	18.1	15.1	1.0
HIP114530	25	479	1279	24305	18.7	15.2	1.0
HIP115162	20	479	1023	24012	18.4	14.9	0.7
HIP115738	29	479	1355	22532	18.4	15.1	0.6
G190-27	32	479	479	7083	18.5	17.6	< 0.5
HIP116748	46	479	2111	22167	18.6	15.3	1.7
HIP116805	30	479	1549	24719	17.9	14.3	0.6
HD222575	20	479	1299	30497	18.8	14.7	1.4
HIP117452	34	479	1416	20177	17.9	14.7	1.4
HIP118121	30	479	1423	22713	18.3	14.9	1.2

Table 8. Properties of the candidates without MIPS data or detection

RA	DEC	Host Star	z'_{ab}	J'	[3.6]	[4.5]	Separation	Distance
(J2000.0)	(J2000.0)	(mag)	(mag)	(mag)	(mag)	'	pc	
02:46:00.708	05:35:00.82	HIP12925	>23.83	>21.48	16.68±0.08	16.76±0.08	67.5130±0.019	54.3±3.0
02:50:00.567	27:16:00.52	HIP13209	>22.73	>20.93	15.59±0.07	15.62±0.07	69.7032±0.021	50.7±0.4
04:48:00.751	-80:46:00.34	HIP22295	>24.75	>21.71	18.42±0.08	18.11±0.08	107.158±0.188	61.0±1.8
05:01:00.177	-20:03:00.08	HIP23362	>24.04	>20.94	18.62±0.08	17.83±0.08	57.8078±0.017	60.6±2.1
05:01:00.270	-20:01:00.43	HIP23362	>24.04	>20.94	17.77±0.08	17.32±0.08	80.2475±0.022	60.6±2.1
05:20:00.536	-39:45:00.03	HIP24947	>22.15	>20.00	18.02±0.08	17.71±0.08	97.8883±0.035	48.3±0.9
06:00:00.277	-44:53:00.56	HIP28474	>24.82	>20.92	18.36±0.05	18.07±0.05	75.5571±0.029	52.5±1.6
06:00:00.613	-44:52:00.49	HIP28474	>24.82	>20.92	17.78±0.05	17.83±0.05	80.8067±0.024	52.5±1.6
06:00:00.859	-44:53:00.07	HIP28474	>24.82	>20.92	17.80±0.25	17.50±0.25	83.5713±0.032	52.5±1.6
06:46:00.315	-83:59:00.83	HIP32435	>25.06	>20.50	19.38±0.08	18.65±0.08	65.1345±0.164	56.0±1.1
07:00:00.902	-79:40:00.69	HIP33737	>24.87	>20.67	18.00±0.08	18.04±0.08	70.2442±0.063	58.8±3.0
09:36:00.173	-78:19:00.80	HIP47135	>24.45	>20.51	17.61±0.25	17.54±0.25	63.8135±0.035	67.9±2.7
09:36:00.649	-78:19:00.76	HIP47135	>24.45	>20.51	19.02±0.25	18.64±0.25	73.1604±0.039	67.9±2.7
11:39:00.275	-32:00:00.12	TWA26	>24.43	>20.93	17.50±0.08	17.38±0.08	78.5368±0.024	41.9±4.5
23:05:00.214	63:58:00.78	HIP114066	>22.46	>20.94	18.58±0.07	17.62±0.07	192.299±0.072	24.5±0.9
23:11:00.882	-45:08:00.82	HIP114530	>23.99	>21.29	16.33±0.05	16.29±0.05	78.7520±0.030	50.7±2.8
23:40:00.795	44:18:00.89	HIP116805	>24.28	>20.89	17.06±0.25	16.96±0.25	87.3615±0.024	51.6±0.5

Table 9. Properties of the candidates identified through color cuts

Host star	RA	DEC	$M_{z'_{ab}}$	M_J	$M_{[3.6]}$	$M_{[4.5]}$	Separation	$\mu_{\alpha} \cos \delta$	μ_{δ}	Rejected at
(J2000.0)	(J2000.0)		(mag)	(mag)	(mag)	(mag)	(AU)	(mas/yr)	(mas/yr)	(sigma)
HIP 14913 A	48.085635	-44.426938	18.26±0.13	15.98±0.06	13.82±0.10	13.31±0.09	5559±101	-46.71±26.00	16.75±30.2700	3
HIP 29964	94.595099	-72.054682	18.35±1.70	16.88±0.02	14.46±0.07	13.46±0.05	1670±116	27.52±17.48	12.81±22.5900	3
HIP 79881	244.61165	-28.608996	18.35±1.60	16.36±0.09	14.05±0.06	13.31±0.05	6365±442	3.73±9.76	-6.13±9.53000	8
HD 152555	253.51768	-4.3371192	18.83±0.07	16.46±0.12	14.08±0.12	13.65±0.11	4895±89	-10.10±13.25	-12.86±17.6900	5

Table 10. Parametrization of the J -band images fraction of pixel as a logistic function

Name	a_0	a_1	a_2
HIP490	8.56	0.83	0.0331
HIP560	13.15	1.09	0.0777
HIP1113	25.65	5.59	0.0308
HIP1134	-0.03	0.16	0.0131
HIP1481	9.54	0.86	0.0308
HIP1910	27.53	3.61	0.0190
HIP1993	16.40	2.14	0.0159
GJ2006A	15.08	2.11	0.0723
HIP2484	23.01	1.86	0.1607
HIP2578	11.85	0.94	0.0705
HIP2729	20.45	2.48	0.0422
HIP3556	14.25	1.83	0.0220
HIP3589	12.73	5.60	0.0085
HIP4448	14.46	1.52	0.0380
G132-51B	15.34	7.27	0.0293
HD6569	25.93	7.47	0.0006
2MASSJ01112542+1526214	1.58	0.41	-0.0013
HIP6276	9.43	1.01	0.0352
2MUCD13056	24.26	5.56	0.0069
HIP6485	17.04	1.65	0.0153
G269-153	1.57	0.36	0.0016
HIP6856	10.55	1.08	0.0148
2MASSJ01351393-0712517	15.31	2.05	0.0097
G271-110	1.03	0.40	0.0069
HIP9141	11.55	1.21	0.0233
HIP9685	11.99	0.99	0.0556
HIP9892	20.89	2.58	0.0311
HIP9902	20.12	2.25	0.0444
HIP10272	-7.50	0.12	0.0014
HIP10602	-7.50	0.12	0.0014
HIP10679	0.20	0.11	-0.0124
HIP11152	16.98	7.29	0.0091
HIP11360	11.00	0.97	0.0427
HIP11437	14.92	6.69	0.0055
1RXSJ022735.8+471021	1.54	0.48	0.0028
HIP12394	13.79	1.05	0.1264
HIP12413	7.66	0.72	0.0215
HIP12545	28.66	3.92	0.0079
AFHor	33.15	4.56	0.0716
HIP12635	14.59	6.49	0.0189
HIP12925	0.06	0.22	0.0131
HIP13027	12.36	1.04	0.0392
HIP13209	-0.39	0.06	-0.0202
HIP14551	6.97	2.76	0.0645
IS-Eri	8.47	0.89	0.0246
HIP14807	27.60	7.14	0.1400
HIP14913	6.98	0.61	0.0980

Table 10 continued

Table 10 (*continued*)

Name	a_0	a_1	a_2
HIP15247	14.17	1.65	0.0688
HIP15353	10.55	0.98	0.0476
CD-351167	16.33	2.15	0.0170
CD-441173	22.96	3.20	0.0031
V577-Per	11.54	5.82	0.0171
2MASSJ03350208+2342356	14.97	6.73	0.0031
HIP16853	33.27	7.23	0.1034
HIP17248	15.42	6.96	0.0172
HIP17695	0.81	0.25	0.0006
HIP17764	13.24	1.34	0.0156
HIP17782	13.72	4.14	0.0124
HIP17797	10.60	0.75	0.1383
HIP18714	0.24	0.01	-1.7864
HIP18859	0.53	0.18	0.0426
HIP19183	0.11	0.16	-0.0017
1RXSJ041417.0-090650	11.22	4.99	0.0019
HIP21547	13.27	5.31	0.0318
HIP21632	16.60	4.36	0.0107
HIP21965	2.09	0.72	0.0418
HIP22295	10.35	1.24	0.0383
TYC5899-0026-1	-2.14	0.01	0.1188
CD-561032	2.10	0.29	0.0559
HIP23179	-7.50	0.12	0.0014
HIP23200	-7.50	0.12	0.0014
HIP23309	20.14	2.41	0.0403
HIP23362	5.12	1.73	0.0720
HIP23418	19.32	7.49	0.0358
GJ3331	-0.36	0.11	-0.0089
HIP24947	21.43	3.15	0.0365
HIP25283	19.84	6.68	0.0210
HIP25486	5.58	1.97	0.0576
HD36705B	5.12	0.43	0.0418
HIP26309	5.14	1.89	0.0568
HIP26369	15.41	2.26	0.1350
HIP26453	-1.29	0.06	-0.0164
HIP26990	8.56	0.88	0.0219
HIP27321	8.61	0.61	0.1049
HIP28036	10.41	1.05	0.0289
HIP28474	16.54	2.13	0.0264
AP-Col	15.45	5.37	0.0041
2MASSJ06085283-2753583	21.45	5.92	0.0084
Cd-352722	19.88	7.25	0.0028
2MASSJ06131330-2742054	18.96	8.37	0.0169
HIP29964	15.90	1.68	0.0304
HIP30030	13.02	4.82	0.0052
HIP30034	12.87	1.63	0.0255
HIP30314	9.40	2.74	0.1025
AK-Pic	10.71	0.89	0.1051
CD-611439	9.11	1.14	0.0365
HIP32104	-0.59	0.10	0.0042
HIP32235	31.16	12.96	0.0080

Table 10 continued

Table 10 (continued)

Name	a_0	a_1	a_2
HIP32435	16.84	2.00	0.0758
HIP33737	15.96	2.26	0.0229
BD+201790	11.76	5.77	0.0355
GJ2060C	14.93	6.76	0.0199
HIP36948	21.77	2.48	0.0199
HIP47135	0.98	0.20	-0.0111
TWA21	29.96	8.66	0.0521
HIP50191	16.72	1.21	0.0821
TWA22	20.99	3.56	0.0257
HIP51317	0.37	0.18	0.0158
TWA1	12.85	5.43	0.0120
TWA2	0.73	0.29	0.0035
TWA12	22.69	3.60	0.0143
TWA13	9.03	1.11	0.0076
TWA4	21.23	7.43	0.0105
TWA5	18.50	2.22	0.0133
TWA30A	19.91	7.73	0.0034
TWA8B	16.13	7.30	0.0047
TWA26	11.52	3.07	0.0018
TWA9	4.98	0.78	0.0195
HIP57632	-2.14	0.01	0.0034
TWA23	0.99	0.35	-0.0049
TWA27	34.27	10.88	0.0066
TWA25	38.04	13.60	0.0373
TWA11C	11.94	0.66	0.4632
GJ490	14.66	4.69	0.0089
PX-Vir	1.18	0.22	0.0118
GJ1167	4.43	1.07	0.0193
HIP68994	19.10	9.87	0.1318
HIP74405	17.95	2.73	0.0097
HIP76629	21.62	11.09	0.0776
HIP76768	18.39	6.07	0.0090
HIP79797	9.18	0.94	0.0414
HIP79881	18.20	7.20	0.0672
HIP81084	24.60	5.29	0.0026
HIP82688	13.27	4.93	0.0157
HIP83494	18.18	5.94	0.0091
HIP84586	9.89	0.97	0.0484
HIP84642	30.29	4.59	0.0371
HIP86346	4.39	1.59	0.0410
HIP88399	15.56	1.75	0.0290
HR6750	27.01	12.57	0.0306
HIP92024	14.68	1.22	0.1004
HIP92680	14.96	1.90	0.0229
HIP94235	15.54	1.97	0.0372
Eta-TeLA	-0.47	0.11	-0.0471
HIP95347	13.18	1.13	0.1059
HIP98495	11.52	0.85	0.0821
HIP99273	8.02	0.83	0.0442
2MASSJ20100002-2801410	12.99	3.07	0.0051
HIP99770	12.90	5.41	0.0476

Table 10 continued

Table 10 (*continued*)

Name	a_0	a_1	a_2
HIP100751	9.37	4.43	0.1676
HIP102141	-2.14	0.01	0.0085
2MASSJ20434114-2433534	16.28	6.92	0.0096
HIP102409	-2.14	0.15	0.0031
HIP103311	8.16	0.79	0.0429
HIP105388	13.80	1.65	0.0211
HIP105404	16.31	1.96	0.0240
HIP107345	23.04	3.32	0.0179
HIP107947	9.72	0.98	0.0259
HIP108195	8.81	0.76	0.0592
HIP108422	27.56	3.51	0.0335
HIP109268	18.00	0.90	0.3030
1RXSJ221419.3+253411	26.00	8.60	0.0146
HIP110526	-7.50	0.12	0.0014
HIP112312	-7.50	0.12	0.0014
HIP113579	0.72	0.31	-0.0191
HIP114066	15.78	7.65	0.0101
HR8799	5.75	0.49	0.0423
HIP114530	11.54	1.37	0.0553
HIP115162	28.82	10.39	0.0034
HIP115738	4.28	1.53	0.0745
G190-27	15.71	6.28	0.0027
HIP116748	8.53	0.77	0.0177
HIP116805	0.63	0.33	0.0582
HD222575	14.18	1.81	0.0231
HIP117452	8.29	0.71	0.0953
HIP118121	12.73	1.05	0.0941

Table 11. Parametrization of *SPITZER*'s fraction of pixel as a logistic function

Name	a_0	a_1	a_2
HIP490	1.91	0.45	0.0003
HIP560	-0.88	0.14	-0.0013
HIP1113	5.30	0.98	0.0030
HIP1134	0.25	0.30	-0.0014
HIP1481	1.36	0.34	-0.0005
HIP1910	5.74	1.00	0.0034
HIP1993	3.00	0.56	0.0040
GJ2006A	6.53	1.46	0.0006
HIP2484	-5.58	0.01	-0.0007
HIP2578	1.34	0.31	-0.0007
HIP2729	8.04	1.43	0.0015
HIP3556	2.13	0.42	0.0031
HIP3589	8.53	1.68	0.0047
HIP4448	4.30	0.79	0.0003
G132-51B	-1.26	0.11	-0.0003
HD6569	-2.87	0.08	0.0001
2MASSJ01112542+1526214	3.17	0.68	0.0019
HIP6276	-0.24	0.10	-0.0018
2MUCD13056	-7.50	0.12	0.0014
HIP6485	6.61	1.24	0.0016
G269-153	-1.17	0.12	-0.0016
HIP6856	4.19	0.76	0.0019
2MASSJ01351393-0712517	2.78	0.61	0.0033
G271-110	-0.60	0.18	-0.0014
HIP9141	7.90	1.46	0.0034
HIP9685	1.04	0.33	0.0007
HIP9892	4.00	0.81	0.0028
HIP9902	6.45	1.34	0.0001
HIP10272	1.22	0.22	7.1525
HIP10602	2.64	0.57	0.0009
HIP10679	4.56	0.94	0.0002
HIP11152	-3.43	0.11	0.0012
HIP11360	-1.32	0.16	-0.0008
HIP11437	-3.68	0.04	1.1444
1RXSJ022735.8+471021	17.71	5.62	0.0011
HIP12394	-0.51	0.13	-0.0027
HIP12413	1.37	0.28	0.0017
HIP12545	2.43	0.57	0.0021
AFHor	-3.26	0.06	4.1483
HIP12635	-3.68	0.04	4.0411
HIP12925	2.81	0.55	0.0021
HIP13027	2.64	0.57	0.0009
HIP13209	0.77	0.26	0.0009
HIP14551	2.27	0.40	0.0004
IS-Eri	3.77	0.77	0.0019
HIP14807	-2.81	0.08	0.0003
HIP14913	2.04	0.35	-0.0003

Table 11 continued

Table 11 (*continued*)

Name	a_0	a_1	a_2
HIP15247	2.25	0.53	0.0021
HIP15353	-0.19	0.18	-0.0010
CD-351167	5.27	0.91	0.0027
CD-441173	2.64	0.57	0.0009
V577-Per	-3.00	0.05	-0.0007
2MASSJ03350208+2342356	-1.31	0.27	0.0001
HIP16853	2.92	0.57	0.0030
HIP17248	3.00	0.95	0.0007
HIP17695	-3.20	0.09	-0.0004
HIP17764	3.28	0.79	0.0023
HIP17782	3.99	0.79	0.0046
HIP17797	5.37	1.03	-2.4497
HIP18714	-1.68	0.06	-0.0019
HIP18859	-1.42	0.12	-0.0015
HIP19183	5.55	1.15	7.8436
1RXSJ041417.0-090650	1.85	0.43	0.0057
HIP21547	2.70	0.93	0.0001
HIP21632	3.46	0.67	0.0006
HIP21965	2.10	0.56	0.0015
HIP22295	4.21	0.74	0.0040
TYC5899-0026-1	1.83	0.36	0.0020
CD-561032	6.79	1.30	0.0049
HIP23179	0.35	0.14	-0.0007
HIP23200	0.65	0.27	-0.0013
HIP23309	3.26	0.58	0.0008
HIP23362	-0.57	0.12	-0.0023
HIP23418	2.33	0.43	0.0041
GJ3331	5.33	1.20	0.0007
HIP24947	3.95	0.74	0.0008
HIP25283	2.41	0.55	0.0007
HIP25486	2.26	0.64	0.0010
HD36705B	-1.65	0.07	-0.0015
HIP26309	2.17	0.40	-0.0001
HIP26369	4.46	0.99	0.0004
HIP26453	2.23	0.45	0.0011
HIP26990	2.56	0.54	0.0018
HIP27321	0.42	0.18	-0.0002
HIP28036	0.53	0.18	-0.0003
HIP28474	3.24	0.87	-4.1604
AP-Col	-3.39	0.10	-0.0001
2MASSJ06085283-2753583	5.37	2.41	0.0034
Cd-352722	3.37	0.59	0.0053
2MASSJ06131330-2742054	4.07	0.81	0.0034
HIP29964	3.33	0.68	0.0048
HIP30030	-7.50	0.12	0.0014
HIP30034	1.80	0.41	0.0019
HIP30314	-0.52	0.11	-0.0015
AK-Pic	-0.25	0.13	-0.0015
CD-611439	2.93	0.61	0.0026
HIP32104	1.64	0.43	0.0022
HIP32235	4.99	0.88	0.0049

Table 11 continued

Table 11 (continued)

Name	a_0	a_1	a_2
HIP32435	3.89	0.76	0.0029
HIP33737	4.50	1.45	0.0026
BD+201790	-2.35	0.13	-0.0003
GJ2060C	-3.05	0.09	0.0020
HIP36948	4.53	0.89	0.0047
HIP47135	4.87	1.19	0.0007
TWA21	3.01	0.75	0.0109
HIP50191	-0.48	0.17	-0.0014
TWA22	-2.14	0.00	0.0035
HIP51317	-4.14	0.08	-0.0002
TWA1	5.41	0.92	0.0041
TWA2	3.31	0.56	0.0035
TWA12	5.48	0.99	0.0057
TWA13	6.36	1.32	0.0003
TWA4	2.28	0.44	0.0003
TWA5	5.40	0.93	0.0024
TWA30A	6.54	3.19	0.0040
TWA8B	4.63	0.99	0.0011
TWA26	8.07	3.90	0.0029
TWA9	-1.42	0.08	-0.0015
HIP57632	0.72	0.24	0.0532
TWA23	4.58	1.00	0.0002
TWA27	-2.14	0.41	0.0027
TWA25	8.21	1.49	0.0016
TWA11C	10.54	5.29	0.0008
GJ490	2.64	0.57	0.0009
PX-Vir	-4.00	0.10	-0.0001
GJ1167	3.50	1.26	0.0046
HIP68994	-1.87	0.30	0.0075
HIP74405	7.52	1.55	0.0027
HIP76629	2.64	0.57	0.0009
HIP76768	4.16	0.85	0.0083
HIP79797	3.80	0.98	0.0030
HIP79881	-1.12	0.16	-0.0010
HIP81084	-2.00	0.11	-0.0006
HIP82688	2.49	0.52	0.0028
HIP83494	3.17	0.64	0.0020
HIP84586	-1.56	0.11	-0.0003
HIP84642	2.82	0.76	0.0032
HIP86346	6.27	1.35	0.0022
HIP88399	-3.41	0.07	0.0013
HR6750	2.90	0.53	0.0039
HIP92024	2.11	0.49	0.0023
HIP92680	3.86	1.10	0.0019
HIP94235	3.63	0.73	0.0024
Eta-TeLA	1.02	0.31	0.0004
HIP95347	-3.26	0.09	3.1232
HIP98495	-0.22	0.13	-0.0025
HIP99273	2.34	0.53	0.0028
2MASSJ20100002-2801410	3.39	0.83	0.0010
HIP99770	2.97	1.00	0.0064

Table 11 continued

Table 11 (*continued*)

Name	a_0	a_1	a_2
HIP100751	2.51	0.45	0.0028
HIP102141	-2.08	0.10	-0.0009
2MASSJ20434114-2433534	12.05	6.37	0.0032
HIP102409	-2.93	0.12	-0.0004
HIP103311	0.33	0.19	-0.0015
HIP105388	4.74	0.92	0.0041
HIP105404	4.20	0.73	0.0017
HIP107345	2.65	0.59	0.0023
HIP107947	2.35	0.44	0.0013
HIP108195	1.91	0.36	0.0003
HIP108422	4.43	0.94	0.0035
HIP109268	-0.61	0.15	-0.0021
1RXSJ221419.3+253411	-3.08	0.10	0.0018
HIP110526	-3.02	0.09	-0.0004
HIP112312	-0.62	0.17	-0.0013
HIP113579	-0.20	0.21	-0.0013
HIP114066	3.89	0.90	0.0043
HR8799	4.45	0.94	0.0001
HIP114530	7.00	1.48	0.0005
HIP115162	3.09	0.96	0.0004
HIP115738	-0.51	0.13	-0.0023
G190-27	-2.66	0.11	-0.0001
HIP116748	-1.80	0.11	-0.0008
HIP116805	-0.01	0.14	-0.0019
HD222575	5.47	1.09	-0.0002
HIP117452	-0.48	0.19	-0.0010
HIP118121	-0.29	0.15	-0.0024

REFERENCES

- Ahn, C. P., Alexandroff, R., Allende Prieto, C., et al. 2012, *The Astrophysical Journal Supplement Series*, 203, 21
- Albert, L. 2006, Ph.D. Thesis, 13
- Albert, L., Artigau, É., Delorme, P., et al. 2011, *The Astronomical Journal*, 141, 203
- Alibert, Y., Pont, F., Baraffe, I., et al. 2009, *Astronomy and Astrophysics*, 506, 391
- Baraffe, I., Chabrier, G., Barman, T. S., Allard, F., & Hauschildt, P. H. 2003, *Astronomy & Astrophysics*, 402, 701
- Baruteau, C., & Masset, F. 2013, *Lecture Notes in Physics*, Berlin Springer Verlag, 861, 201
- Bate, M. R. 2012, *Monthly Notices of the Royal Astronomical Society*, 419, 3115
- Bate, M. R., Bonnell, I. A., & Bromm, V. 2002, *Monthly Notices of the Royal Astronomical Society*, 332, L65
- Beichman, C., Gelino, C. R., Kirkpatrick, J. D., et al. 2014, *The Astrophysical Journal*, 783, 68
- Bell, C. P. M., Mamajek, E. E., & Naylor, T. 2016, *Young Stars & Planets Near the Sun*, 314, 41
- Berger, J. O., Bernardo, J. M., & Sun, D. 2009, *The Annals of Statistics*, 37, 905
- Bertin, E. 2010a, *Astrophysics Source Code Library*, ascl:1010.063
- 2010b, *Astrophysics Source Code Library*, ascl:1010.068
- Bertin, E., & Arnouts, S. 1996, *Astronomy and Astrophysics Supplement Series*, 117, 393
- Biller, B. A., Liu, M. C., Wahhaj, Z., et al. 2010, *The Astrophysical Journal Letters*, 720, L82
- 2013, *The Astrophysical Journal*, 777, 160
- Binks, A. S., Jeffries, R. D., & Maxted, P. F. L. 2015, *Monthly Notices of the Royal Astronomical Society*, 452, 173
- Blunt, S., Nielsen, E. L., Rosa, D., et al. 2017, *The Astronomical Journal*, 153, 229
- Boss, A. P. 2011, *The Astrophysical Journal*, 731, 74
- Boulade, O., Vigroux, L. G., Charlot, X., et al. 1998, in , 614
- Bowler, B. P. 2016, *Publications of the Astronomical Society of the Pacific*, 128, 102001
- Bowler, B. P., Liu, M. C., Shkolnik, E. L., & Tamura, M. 2015, *The Astrophysical Journal Supplement Series*, 216, 7
- Brandeker, A., Jayawardhana, R., Khavari, P., Haisch, Jr., K. E., & Mardones, D. 2006, *The Astrophysical Journal*, 652, 1572
- Brandt, T. D., McElwain, M. W., Turner, E. L., et al. 2014, *The Astrophysical Journal*, 794, 159
- Bryan, M. L., Bowler, B. P., Knutson, H. A., et al. 2016, *The Astrophysical Journal*, 827, 100
- Chambers, K., & Team, P.-S. 2018, *American Astronomical Society Meeting Abstracts*
- Chatterjee, S., Ford, E. B., Matsumura, S., & Rasio, F. A. 2008, *The Astrophysical Journal*, 686, 580
- Chauvin, G., Lagrange, A.-M., Dumas, C., et al. 2004, *Astronomy and Astrophysics*, 425, L29
- Chauvin, G., Lagrange, A.-M., Zuckerman, B., et al. 2005, *Astronomy and Astrophysics*, 438, L29
- Chauvin, G., Vigan, A., Bonnefoy, M., et al. 2015, *Astronomy and Astrophysics*, 573, A127
- Choquet, É., Pueyo, L., Soummer, R., et al. 2015, *Techniques and Instrumentation for Detection of Exoplanets VII*, 9605, 96051P
- Cutri, R. M., Skrutskie, M. F., van Dyk, S., et al. 2003, *VizieR Online Data Catalog*, 2246, 0
- Daddi, E., Dickinson, M., Morrison, G., et al. 2007, *The Astrophysical Journal*, 670, 156
- de la Reza, R., Torres, C. A. O., Quast, G., Castilho, B. V., & Vieira, G. L. 1989, *The Astrophysical Journal Letters*, 343, L61
- Delorme, P., Delfosse, X., Albert, L., et al. 2008, *Astronomy and Astrophysics*, 482, 961, 00101
- Delorme, P., Albert, L., Forveille, T., et al. 2010, *Astronomy and Astrophysics*, 518, A39
- Delorme, P., Gagné, J., Girard, J. H., et al. 2013, *Astronomy and Astrophysics*, 553, L5
- Dupuy, T. J., & Liu, M. C. 2012, *The Astrophysical Journal Supplement Series*, 201, 19
- Durkan, S., Janson, M., & Carson, J. C. 2016, *The Astrophysical Journal*, 824, 58
- Eikenberry, S., Bandyopadhyay, R., Bennett, J. G., et al. 2012, *Ground-based and Airborne Instrumentation for Astronomy IV*, 8446, 84460I
- Faherty, J. K., Riedel, A. R., Cruz, K. L., et al. 2016, *The Astrophysical Journal Supplement Series*, 225, 10
- Fazio, G. G., Hora, J. L., Allen, L. E., et al. 2004, *The Astrophysical Journal Supplement Series*, 154, 10
- Fortney, J. J., Marley, M. S., Saumon, D., & Lodders, K. 2008, *The Astrophysical Journal*, 683, 1104
- Gagné, J., Allers, K. N., Theissen, C. A., et al. 2018a, *The Astrophysical Journal Letters*, 854, L27
- Gagné, J., Burgasser, A. J., Faherty, J. K., et al. 2015a, *The Astrophysical Journal Letters*, 808, L20
- Gagné, J., Lafrenière, D., Doyon, R., Malo, L., & Artigau, É. 2014, *The Astrophysical Journal*, 783, 121
- Gagné, J., Faherty, J. K., Cruz, K. L., et al. 2015b, *The Astrophysical Journal Supplement Series*, 219, 33
- Gagné, J., Mamajek, E. E., Malo, L., et al. 2018b, *The Astrophysical Journal*, 856, 23
- Gaia Collaboration, Brown, A. G. A., Vallenari, A., et al. 2018, *ArXiv e-prints*, 1804, arXiv:1804.09365
- Gaia Collaboration, Prusti, T., de Bruijne, J. H. J., et al. 2016, *Astronomy and Astrophysics*, 595, A1
- Galicher, R., Marois, C., Macintosh, B., et al. 2016, *Astronomy and Astrophysics*, 594, A63

- Gauza, B., Béjar, V. J. S., Pérez-Garrido, A., et al. 2015, *The Astrophysical Journal*, 804, 96
- Jimeno, G., Roth, K., Chiboucas, K., et al. 2016, in *Ground-based and Airborne Instrumentation for Astronomy VI*, Vol. 9908 (International Society for Optics and Photonics), 99082S
- Goldman, B., Marsat, S., Henning, T., Clemens, C., & Greiner, J. 2010, *Monthly Notices of the Royal Astronomical Society*, 405, 1140
- Hawley, S. L., Covey, K. R., Knapp, G. R., et al. 2002, *The Astronomical Journal*, 123, 3409
- Heinze, A. N., Hinz, P. M., Kenworthy, M., et al. 2010, *The Astrophysical Journal*, 714, 1570
- Hook, I. M., Jørgensen, I., Allington-Smith, J. R., et al. 2004, *Publications of the Astronomical Society of the Pacific*, 116, 425, 00290
- Inaba, S., Wetherill, G. W., & Ikoma, M. 2003, *Icarus*, 166, 46
- Janson, M., Bonavita, M., Klahr, H., et al. 2011, *The Astrophysical Journal*, 736, 89
- Janson, M., Quanz, S. P., Carson, J. C., et al. 2015, *Astronomy and Astrophysics*, 574, A120
- Janson, M., Brandt, T. D., Moro-Martín, A., et al. 2013, *The Astrophysical Journal*, 773, 73
- Kastner, J. H., Zuckerman, B., Weintraub, D. A., & Forveille, T. 1997, *Science*, 277, 67
- Kipping, D. M. 2013, *Monthly Notices of the Royal Astronomical Society*, 434, L51
- Kirkpatrick, A., Pope, A., Alexander, D. M., et al. 2012a, *The Astrophysical Journal*, 759, 139
- Kirkpatrick, J. D., Gelino, C. R., Cushing, M. C., et al. 2012b, *The Astrophysical Journal*, 753, 156
- Kiss, L. L., Moór, A., Szalai, T., et al. 2011, *Monthly Notices of the Royal Astronomical Society*, 411, 117
- Kraus, A. L., Shkolnik, E. L., Allers, K. N., & Liu, M. C. 2014, *The Astronomical Journal*, 147, 146, 00000
- Lafrenière, D., Marois, C., Doyon, R., Nadeau, D., & Artigau, É. 2007a, *The Astrophysical Journal*, 660, 770
- Lafrenière, D., Doyon, R., Marois, C., et al. 2007b, *The Astrophysical Journal*, 670, 1367
- Lagrange, A.-M., Gratadour, D., Chauvin, G., et al. 2009, *Astronomy and Astrophysics*, 493, L21
- Lannier, J., Delorme, P., Lagrange, A. M., et al. 2016, *Astronomy and Astrophysics*, 596, A83
- Lépine, S., & Simon, M. 2009, *The Astronomical Journal*, 137, 3632
- Lindgren, L., Hernandez, J., Bombrun, A., et al. 2018, [arXiv:1804.09366 \[astro-ph\]](https://arxiv.org/abs/1804.09366), [arXiv: 1804.09366](https://arxiv.org/abs/1804.09366)
- Liu, M. C., Magnier, E. A., Deacon, N. R., et al. 2013, *The Astrophysical Journal Letters*, 777, L20
- Lodieu, N., Béjar, V. J. S., & Rebolo, R. 2013, *Astronomy and Astrophysics*, 550, L2
- Looper, D. L., Bochanski, J. J., Burgasser, A. J., et al. 2010, *The Astronomical Journal*, 140, 1486
- Macintosh, B., Graham, J. R., Barman, T., et al. 2015, *Science*, 350, 64
- Makarov, V. V., & Urban, S. 2000, *Monthly Notices of the Royal Astronomical Society*, 317, 289
- Malo, L., Doyon, R., Feiden, G. A., et al. 2014, *The Astrophysical Journal*, 792, 37
- Malo, L., Doyon, R., Lafrenière, D., et al. 2013, *The Astrophysical Journal*, 762, 88
- Marley, M. S., Fortney, J. J., Hubickyj, O., Bodenheimer, P., & Lissauer, J. J. 2007, *The Astrophysical Journal*, 655, 541
- Marois, C., Macintosh, B., Barman, T., et al. 2008, *Science*, 322, 1348
- Marois, C., Zuckerman, B., Konopacky, Q. M., Macintosh, B., & Barman, T. 2010, *Nature*, 468, 1080
- Mayor, M., & Queloz, D. 1995, *Nature*, 378, 355
- McMahon, R. G., Banerji, M., Gonzalez, E., et al. 2013, *The Messenger*, 154, 35
- Millar-Blanchaer, M. A., Graham, J. R., Pueyo, L., et al. 2015, *The Astrophysical Journal*, 811, 18
- Montet, B. T., Bowler, B. P., Shkolnik, E. L., et al. 2015, *The Astrophysical Journal Letters*, 813, L11
- Moór, A., Szabó, G. M., Kiss, L. L., et al. 2013, *Monthly Notices of the Royal Astronomical Society*, 435, 1376
- Mordasini, C., Alibert, Y., Klahr, H., & Henning, T. 2012, *Astronomy and Astrophysics*, 547, A111
- Morzinski, K. M., Males, J. R., Skemer, A. J., et al. 2015, *The Astrophysical Journal*, 815, 108
- Naud, M.-E., Artigau, É., Doyon, R., et al. 2017, *The Astronomical Journal*, 154, 129
- Naud, M.-E., Artigau, É., Malo, L., et al. 2014, *The Astrophysical Journal*, 787, 5, 00000
- Nayakshin, S. 2017, *Monthly Notices of the Royal Astronomical Society*, 470, 2387
- Nielsen, E. L., Close, L. M., Biller, B. A., Masciadri, E., & Lenzen, R. 2008, *The Astrophysical Journal*, 674, 466
- Nielsen, E. L., Liu, M. C., Wahhaj, Z., et al. 2013, *The Astrophysical Journal*, 776, 4
- Padoan, P., & Nordlund, A. 2004, *The Astrophysical Journal*, 617, 559
- Pollack, J. B., Hubickyj, O., Bodenheimer, P., et al. 1996, *Icarus*, 124, 62
- Puget, P., Stadler, E., Doyon, R., et al. 2004, *Ground-based Instrumentation for Astronomy*, 5492, 978
- Rajan, A., Rameau, J., De Rosa, R. J., et al. 2017, *The Astronomical Journal*, 154, 10, [arXiv: 1705.03887](https://arxiv.org/abs/1705.03887)
- Rameau, J., Chauvin, G., Lagrange, A.-M., et al. 2013, *Astronomy and Astrophysics*, 553, A60

- Riedel, A. R., Finch, C. T., Henry, T. J., et al. 2014, *The Astronomical Journal*, 147, 85
- Rodriguez, D. R., Bessell, M. S., Zuckerman, B., & Kastner, J. H. 2011, *The Astrophysical Journal*, 727, 62
- Rodriguez, D. R., Zuckerman, B., Kastner, J. H., et al. 2013, *The Astrophysical Journal*, 774, 101
- Schlieder, J. E., Lépine, S., & Simon, M. 2010, *The Astronomical Journal*, 140, 119
- . 2012a, *The Astronomical Journal*, 143, 80
- . 2012b, *The Astronomical Journal*, 144, 109
- Schneider, G., Song, I., Zuckerman, B., et al. 2004, *American Astronomical Society Meeting Abstracts*, 11.14
- Shkolnik, E., Liu, M. C., & Reid, I. N. 2009, *The Astrophysical Journal*, 699, 649
- Shkolnik, E. L., Allers, K. N., Kraus, A. L., Liu, M. C., & Flagg, L. 2017, *The Astronomical Journal*, 154, 69
- Shkolnik, E. L., Anglada-Escudé, G., Liu, M. C., et al. 2012, *The Astrophysical Journal*, 758, 56
- Shkolnik, E. L., Liu, M. C., Reid, I. N., Dupuy, T., & Weinberger, A. J. 2011, *The Astrophysical Journal*, 727, 6
- Smart, R. L., Marocco, F., Caballero, J. A., et al. 2017, *Monthly Notices of the Royal Astronomical Society*, 469, 401
- Soderblom, D. R. 2010, *Annual Review of Astronomy and Astrophysics*, 48, 581
- Song, I., Zuckerman, B., & Bessell, M. S. 2003, *The Astrophysical Journal*, 599, 342
- Soumer, R., Pueyo, L., & Larkin, J. 2012, *The Astrophysical Journal Letters*, 755, L28
- Soumer, R., Choquet, E., Pueyo, L., et al. 2016, *American Astronomical Society Meeting Abstracts #227*, 227, 137.03
- Stamatellos, D., Hubber, D. A., & Whitworth, A. P. 2007, *Monthly Notices of the Royal Astronomical Society*, 382, L30
- Tonry, J. L., Stubbs, C. W., Lykke, K. R., et al. 2012, *The Astrophysical Journal*, 750, 99
- Torres, C. A. O., da Silva, L., Quast, G. R., de la Reza, R., & Jilinski, E. 2000, *The Astronomical Journal*, 120, 1410
- Torres, C. A. O., Quast, G. R., Melo, C. H. F., & Sterzik, M. F. 2008, in *Handbook of Star Forming Regions, Volume II*, 757
- Veras, D., Crepp, J. R., & Ford, E. B. 2009, *The Astrophysical Journal*, 696, 1600
- Vigan, A., Patience, J., Marois, C., et al. 2012, *Astronomy and Astrophysics*, 544, A9
- Vigan, A., Bonavita, M., Biller, B., et al. 2017, *Astronomy and Astrophysics*, 603, A3
- Wahhaj, Z., Liu, M. C., Nielsen, E. L., et al. 2013, *The Astrophysical Journal*, 773, 179
- Wang, J., Fischer, D. A., Xie, J.-W., & Ciardi, D. R. 2015, *The Astrophysical Journal*, 813, 130
- Wertz, O., Absil, O., González, G., et al. 2017, *Astronomy and Astrophysics*, 598, A83
- Wolf, C., Onken, C. A., Luvaul, L. C., et al. 2018, *Publications of the Astronomical Society of Australia*, 35, e010
- Zuckerman, B. 2001, *Young Stars Near Earth: Progress and Prospects*, 244, 122
- Zuckerman, B., Rhee, J. H., Song, I., & Bessell, M. S. 2011, *The Astrophysical Journal*, 732, 61
- Zuckerman, B., & Song, I. 2004, *Annual Review of Astronomy and Astrophysics*, 42, 685
- Zuckerman, B., Song, I., & Bessell, M. S. 2004, *The Astrophysical Journal Letters*, 613, L65
- Zuckerman, B., Song, I., Bessell, M. S., & Webb, R. A. 2001a, *The Astrophysical Journal Letters*, 562, L87
- Zuckerman, B., Song, I., & Webb, R. A. 2001b, *The Astrophysical Journal*, 559, 388
- Zuckerman, B., & Webb, R. A. 2000, *The Astrophysical Journal*, 535, 959